Generation and Active Absorption of 2- and 3-Dimensional Linear Water Waves in Physical Models

Christensen, Morten

Publication date:
1995

Document Version
Publisher's PDF, also known as Version of record

Link to publication from Aalborg University

Citation for published version (APA):
Christensen, M. (1995). *Generation and Active Absorption of 2- and 3-Dimensional Linear Water Waves in Physical Models*. Hydraulics & Coastal Engineering Laboratory, Department of Civil Engineering, Aalborg University.

Hydraulics & Coastal Engineering Laboratory
Department of Civil Engineering
Aalborg University
SERIES PAPER No. 11

ISSN 0909 - 4296

Generation and Active Absorption of 2- and 3-Dimensional Linear Water Waves in Physical Models

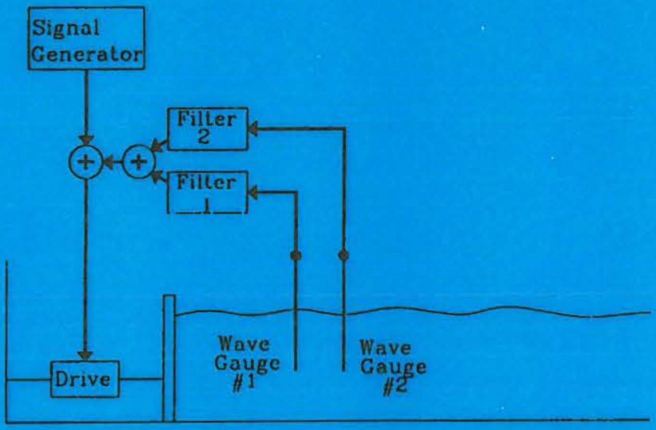

Morten Christensen

August 1995

Hydraulics & Coastal Engineering Laboratory
Aalborg University
Sohngaardsholmsvej 57, DK-9000 Aalborg, Denmark

Hydraulics & Coastal Engineering Laboratory
Department of Civil Engineering
Aalborg University
Sohngaardsholmsvej 57
DK-9000 Aalborg, Denmark

ISSN 0909-4296
SERIES PAPER No. 11

GENERATION AND ACTIVE ABSORPTION OF 2- AND 3-DIMENSIONAL LINEAR WATER WAVES IN PHYSICAL MODELS

by

Morten Christensen

August 1995

Preface

The present thesis *Generation and Active Absorption of 2- and 3-Dimensional Linear Water Waves in Physical Models* is submitted as one of the requirements for obtaining the Ph.D. degree according to notice no. 627 of 17 October 1988 from the Danish Ministry of Education.

The study was carried out at the Department of Civil Engineering, Aalborg University, from August 1992 to July 1995 under the supervision of Associate Professor M. Brorsen.

The author wishes to thank Associate Professor M. Brorsen and Associate Professor P. Frigaard for scientific supervision and the staff at the Hydraulics and Coastal Engineering Laboratory for their assistance in carrying out the experimental work. Furthermore, thanks are due to Ph.D.-student J. Helm-Petersen who read and commented the manuscript and to secretary Birte Torstveit who proofread the manuscript.

Aalborg, 01.08.95

Morten Christensen

Contents

Symbols

a : Fourier coefficient

A : wave amplitude

b : Fourier coefficient

c : phase velocity

c_g : group velocity

d : water depth

$D(\omega, \theta)$: directional spreading function

$\mathcal{D}$: desired complex frequency response

e : wave paddle displacement amplitude (in App. A: $e^z = \exp(z)$)

E_f : energy flux

f : frequency

f_p : peak frequency

f_s : sampling frequency

g : acceleration of gravity

H_{m_0} : Estimate of H_s based on 0'th moment of freq. spectrum ($H_{m_0} = 4.004\sqrt{m_0}$)

H_s : significant wave height

$\mathcal{H}$: complex filter frequency response

i : imaginary unit, $i = \sqrt{-1}$ (in App. A)

k : wave number $k = 2\pi/L$

k_n : wave number corresponding to near-field solution

K_n : near-field Biésel coefficient

K_f : far-field Biésel coefficient

L : wave length

m_n : n'th moment of frequency spectrum

MWL : mean water level

$\mathcal{N}(\mu, \sigma^2)$: Normal distribution with mean μ and variance σ^2.

N_l : number of dir. wave gen. paddles pr. period in y-direction

s : spreading parameter

$S_\eta(\omega)$: frequency spectrum

$S_\eta(\omega,\theta)$: directional spectrum

$S_{XY}(\omega)$: Cross spectral density between processes X and Y

t : time

T : period

$\mathcal{U}[0..1]$: uniform distribution in the interval from 0 to 1.

$\mathcal{W}$: servocontrol system complex frequency response

x, y : rectangular coordinates

X : wave generator displacement

α : random number ($\alpha : \mathcal{N}(0,1)$)

β : random number ($\beta : \mathcal{N}(0,1)$)

Γ : the Gamma function

ϕ : phase

ω : cyclic frequency, $\omega = 2\pi f$

η : surface elevation

θ : wave direction

θ_0 : mean wave direction

θ_{min} : min. direction of propagation in decomposed dir. spectrum

θ_{max} : max. direction of propagation in decomposed dir. spectrum

σ_θ : spreading width of directional spreading function

δ : delay

$x.re$: real part of complex number x

$x.im$: imaginary part of complex number x

$amp(x(t))$: amplitude of harmonic function $x(t)$

Abstract

Methods for mechanical generation of 2-dimensional (2-D) and 3-dimensional (3-D) linear water waves in physical models are presented.
The results of a series of laboratory 3-D wave generation tests are presented and discussed. The tests performed involve reproduction of wave fields characterised by different directional wave spectra. The wave generator displacement signals applied in the tests are generated by means of linear digital filtering of Gaussian white noise in the time domain.

An absorbing wave generator for 2-D wave facilities (wave channels) is developed. The absorbing wave generator is based on a new principle for active absorption of reflected waves: the wave generator displacement correction signal corresponding to absorption of the reflected wave train is determined by means of linear filtering and subsequent superposition of surface elevation signals measured in two positions in the wave channel in front of the wave generator. The results of physical model tests performed with an absorbing wave maker based on this principle show that the problem of rereflection is reduced significantly when active absorption is performed.
Finally, an absorbing directional wave generator for 3-D wave facilities (wave basins) based on a similar principle is developed. A conventional directional wave generator is converted into an absorbing directional wave generator based on this principle and applied to a series of physical model tests. The test results show that the absorbing directional wave generator is capable of reducing the problem of rereflection in multi-directional, irregular wave fields significantly.

Dansk resumé

Metoder til mekanisk generering af 2-dimensionale (2-D) og 3-dimensionale (3-D) lineære bølger i fysiske modeller præsenteres.
Resultaterne af en række laboratorie 3-D bølgegenereringsforsøg præsenteres og diskuteres. Forsøgene omfatter reproduktion af bølgefelter karakteriseret ved forskellige retningsspektre. De anvendte bølgegeneratorflytningssignaler genereres vha. lineær digital filtrering af Gaussisk hvid støj i tidsdomænet.

En absorberende bølgegenerator til 2-D laboratoriefaciliteter (bølgekanaler) udvikles. Den absorberende bølgegenerator er baseret på et nyt princip for aktiv absorption af reflekterede bølger: Bølgegeneratorflytningskorrektionssignalet svarende til absorption af det reflekterede bølgetog fastlægges vha. lineær filtrering og efterfølgende superposition af overfladeelevationssignaler målt i to positioner i bølgekanalen foran bølgegeneratoren. Resultaterne af laboratorieforsøg udført med en absorberende bølgegenerator baseret på dette princip viser at problemer med rerefleksion reduceres væsentligt når aktiv absorption foretages.
Endvidere udvikles en absorberende 3-D bølgegenerator baseret på et lignende princip. En konventionel 3-D bølgegenerator laves om til en absorberende bølgegenerator baseret på dette princip, og en række laboratorieforsøg udføres med denne bølgegenerator. Forsøgsresultaterne viser, at den absorberende 3-D bølgegenerator er i stand til at reducere problemerne med rerefleksion i retningsspredte, uregelmæssige bølgefelter væsentligt.

1 Introduction

The purpose of the present article is to present the maximum likelihood method for estimating directional spectra. In short, a directional spectrum expresses how the wave energy is distributed on both frequencies and directions. The presentation is based on the references [Isobe, M. and K. Kondo; 1984], [Isobe, M.; 1990] and [Yokoki, H., M. Isobe and A. Watanabe; 1992]. The directional spectrum is given in a standard form in terms of some unknown parameters to be estimated from measured data. In the present article only surface elevation measurements are treated.

The directional spectrum estimation is based on surface elevations measured in a two-dimensional wave gauge array consisting of M gauges. From these measurements it is possible to identify both directions and frequencies of the wave pattern. In order to perform the identification, a relation between the cross correlation matrix of the M elevation processes and the directional spectrum is established (see section 2). The underlying assumption is that the elevation processes at one point can be considered as a sum of harmonic components having Rayleigh distributed amplitudes and uniformly distributed phases. Assuming all phases and amplitudes to be independent, the elevation processes become normally distributed. Furthermore, the theory described in section 2 offers the possibility of introducing reflected waves.

In section 3 the likelihood function is introduced. Again, the starting point is the M elevation processes. Based on an assumption of stationary processes, the M time series are expressed as Fourier sums. It is emphasised, that the Fourier coefficients at a given frequency are jointly Gaussian variables. Furthermore, the mean value vector and the cross correlation matrix of the Fourier coefficients are determined, and it is shown that the elements in the cross correlation matrix are given in terms of the cross spectral density matrix of the M elevation processes. The results show that the cross spectral density matrix is a function of the directional spectrum and therefore the distribution of the Fourier coefficients becomes a function of the unknown directional spectrum. A likelihood function is formulated in terms of the probability density function of the Fourier coefficients and the the maximum likelihood estimates of the unknown parameters in the directional spectrum are found by maximising the likelihood function, i.e. by maximising the probability of observing the Fourier coefficients obtained.

In order to determine the performance of the maximum likelihood method, the method has been implemented and applied to numerically simulated surface elevation time series (see section 4). The implementation estimates the parameters in the Mitsuyasu directional spectrum based on surface elevation time series measured simultaneously in an arbitrary number of wave gauges. The likelihood function is maximised using the method described by [Nelder, J. A. and R. Mead; 1965]. Numerical tests both with and without reflected waves are presented.

2 Relation between Cross-Spectral Density and Directional Spectrum

In the following section a relation between the one-sided cross-spectral density matrix $G_{\eta_m\eta_n}\left(\underline{x}_m, \underline{x}_n, \omega\right), \omega \geq 0$, and the one-sided directional spectrum $S_\eta(\omega, \theta)$ will be established. The cross spectral density matrix refers to the elevation processes η_m and η_n at the locations $\underline{x}_m$ and $\underline{x}_n$ characterized by a constant depth d. The relation will be established assuming the presence of reflected waves. The starting point is the following wave model (no reflection)

$$\eta\left(\underline{x}, t\right) = \sum_{j=1}^{J}\sum_{i=1}^{I} A_{ji} cos\left(k_j x \, cos\theta_i + k_j \, y \, sin\theta_i - \omega_j t + \Psi_{ji}\right) \tag{1}$$

where A_{ji} : wave amplitude
ω_j : circular wave frequency
θ_i : wave direction
Ψ_{ji} : phase
k_j : wave number

Based on this model the total elevation is obtained as the sum of waves having different frequencies (indices j) and directions (indices i). The frequencies are in the range $[-\infty, \infty]$ and the directions are in the range $[0, 2\pi]$.
The wave number, k_j, is determined from the linear dispersion relation

$$\frac{\omega_j}{k_j} = \frac{g}{\omega_j} tanh\left(k_j \cdot d\right) \tag{2}$$

The amplitudes are assumed to be Rayleigh distributed, i.e. the density function of the amplitudes is given by

$$f_{A_{ji}}(a_{ji}) = \frac{a_{ji}}{\sigma_{ji}^2} exp\left(\frac{-a_{ji}}{2\sigma_{ji}}\right) \tag{3}$$

The phases are assumed to be uniformly distributed, i.e. $\Psi_{ji} \in U[0, 2\pi]$.
All Ψ_{ji} are assumed to be independent, all A_{ji} are assumed to be independent and A_{ji} and Ψ_{ji} are mutually independent too.
As a consequence of these assumptions it can be proved that $\eta\left(\underline{x}, t\right)$ becomes normally distributed with mean value function equal to 0 and variance equal

to $\sum_{j=1}^{J}\sum_{i=1}^{I}\sigma_{ji}^2$ (see e.g. [Nielsen, S. R. K.; 1993]).

Introducing the directional spectrum $S_\eta(\omega,\theta)$, which describes how the energy is distributed on frequencies and directions, the following relation exists between the one-sided autospectral density $G_\eta(\omega)$ and $S_\eta(\omega,\theta)$

$$G_\eta(\omega) = \int_0^{2\pi} S_\eta(\omega,\theta)\,d\theta \tag{4}$$

If the energy is concentrated at discrete frequencies ω_j and directions θ_i as shown in (1) the following relation may be established between σ_{ji} and $S_\eta(\omega,\theta)$

$$\sigma_{ji}^2 = S_\eta\left(\omega_j,\theta_i\right)\Delta\omega_j\cdot\Delta\theta_i \tag{5}$$

where $\Delta\omega_j$ and $\Delta\theta_i$ represent frequency- and direction-intervals around ω_j and θ_i.

In the following a relation between the one-sided cross-spectral density function $G_{\eta_m\eta_n}\left(\underline{x}_m,\underline{x}_n,\omega\right)$ and $S_\eta(\omega,\theta)$ will be established, but first the possibility of introducing reflected waves will be discussed. It is assumed that the incident wave pattern given by (1) is reflected at the y-axis as shown in figure 1.

Obviously the reflected waves $\eta_r\left(\underline{x},t\right)$ are connected to the "initial" wave pattern given by (1) and characterized by $S_\eta(\omega,\theta)$. As shown in figure 1 the angle of incidence is assumed to be equal to the angle of reflection. If the incident wave number vector $\underline{k}$ is given as $\underline{k}^T = k(\omega)[cos\theta, sin\theta]$ the reflected wave number vector $\underline{k}_r$ is given as $\underline{k}_r^T = k\underline{T}[cos\theta, sin\theta] = k[-cos\theta, sin\theta]$ where $\underline{T}$ is a transformation matrix equal to

$$\underline{T} = \begin{bmatrix} -1 & 0 \\ 0 & 1 \end{bmatrix} \tag{6}$$

The amplitude of the reflected wave is assumed to be reduced to $r(\omega_j,\theta_i)\cdot A_{ji}$ where r is the reflection coefficient at the frequency ω_j in the direction θ_i. In the following, the reflection coefficient is assumed to be independent of the wave direction θ_i. This assumption is generally valid for a plane reflective wall and wave directions of $\theta_i \in [\frac{3\pi}{4}..\frac{5\pi}{4}]$, i.e. directions for which no Mach

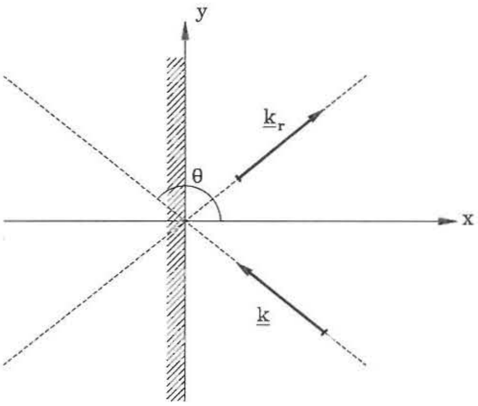

Figure 1: Incident and reflected waves.

reflection occurs, see [Svendsen, I. A. and Jonsson, I. G.; 1980]. Introducing the notation $r_j = r(\omega_j)$ the surface elevation in the combined wave field is given by

$$\begin{aligned}\eta\left(\underline{x}, t\right) &= \sum_{j=1}^{J}\sum_{i=1}^{I} A_{ji} cos\left(k_j x \, cos\theta_i + k_j \, y \, sin\theta_i - \omega_j t + \Psi_{ji}\right) \\ &+ \sum_{j=1}^{J}\sum_{i=1}^{I} r_j A_{ji} cos\left(k_j x\left(-cos\theta_i\right) + k_j y \, sin\theta_i - \omega_j t + \Psi_{ji}\right) \qquad (7)\end{aligned}$$

r_j is assumed to be deterministic. With $\eta(\underline{x}, t)$ given by (7) the cross correlation function of η can be calculated as $\kappa_{\eta_m\eta_n}\left(t_n - t_m\right) = E\left[\eta_m(\underline{x}_m, t_m)\eta_n(\underline{x}_n t_n)\right]$ where η_m and η_n represent the total elevation processes. Introducing $\tau = t_n - t_m$ the one-sided cross spectral density function $G_{\eta_m\eta_n}\left(\underline{x}_m, \underline{x}_n, \omega\right)$ is determined as

$$G_{\eta_m\eta_n}\left(\underline{x}_m, \underline{x}_n, \omega\right) = 2\int_{-\infty}^{\infty} e^{-i\omega\tau} E\left[\eta_m\left(\underline{x}_m, t_m\right)\eta_n\left(\underline{x}_n, t_m + \tau\right)\right] d\tau \qquad (8)$$

After some calculations the following result is obtained

$$\begin{aligned} G_{\eta_m \eta_n}(\omega) &= \int_0^{2\pi} S_\eta(\omega,\theta) \left\{ e^{ik(\omega)\left(\underline{x}_m^T - \underline{x}_n^T\right)\underline{\theta}} + r(\omega)\, e^{ik(\omega)\left(\underline{x}_m^T - \underline{x}_n^T \underline{T}\right)\underline{\theta}} \right. \\ & \left. + r(\omega) e^{ik(\omega)\left(\underline{x}_m^T \underline{T} - \underline{x}_n^T\right)\underline{\theta}} + r^2(\omega) e^{ik(\omega)\left(\underline{x}_m^T - \underline{x}_n^T\right)\underline{T}\,\underline{\theta}} \right\} d\theta \qquad (9) \end{aligned}$$

where $\underline{\theta}^T = [cos\theta, sin\theta]$.
If no reflection is present, i.e. $r = 0$, this relation is reduced to

$$G_{\eta_m \eta_n}(\omega) = \int_0^{2\pi} S_\eta(\omega,\theta)\, e^{ik(\omega)\left(\underline{x}_m^T - \underline{x}_n^T\right)\underline{\theta}}\, d\theta \qquad (10)$$

3 The Maximum Likelihood Method Theory

The starting point is M surface elevation time series, $\eta(\underline{x}, t)$, measured at M different locations $\underline{x}$. The total elevation processes $\eta_i\left(\underline{x}_i, t\right),\ i = 1, \ldots, M$, are modelled as stochastic processes. The processes are assumed to be joint stationary, ergodic normally distributed. The mean value functions $\mu_{\eta_i}(t),\ i = 1, \ldots, M$, are assumed to be equal to 0. The M time series can be written as a Fourier-sum as

$$\eta_i\left(\underline{x}, t\right) = \sum_{j=1}^{\infty} \left(A_{cj}^i cos\omega_j t + A_{sj}^i sin\omega_j t \right),\ i = 1, .., M \qquad (11)$$

where

$$\begin{aligned} \omega_j &= 2\pi\, f_j \\ f_j &= j \cdot f_1 \\ f_1 &= 1/T \end{aligned}$$

and T is the length of the time series. The coefficients A_{cj}^i and A_{sj}^i are given as the stochastic integrals

$$A^i_{cj} = \frac{2}{T}\int_{-\frac{T}{2}}^{\frac{T}{2}} \eta_i\left(\underline{x}_i, t\right) cos\omega_j t\, dt \quad , \quad j = 1, 2, \ldots, i = 1, \ldots, M \tag{12}$$

$$A^i_{sj} = \frac{2}{T}\int_{-\frac{T}{2}}^{\frac{T}{2}} \eta_i\left(\underline{x}_i, t\right) sin\omega_j t\, dt \quad , \quad j = 1, 2, \ldots, i = 1, \ldots, M \tag{13}$$

In (11) the term corresponding to $j = 0$ has been omitted as it equals 0. From (12) and (13) it is seen that all the coefficients A^i_{cj} and A^i_{sj} are joint normally distributed stochastic variables.
In the following only the j'th components are considered. The primary goal is to determine the joint distribution of the coefficients A^i_{cj} and A^i_{sj}, $i = 1, \ldots, M$, at the frequency ω_j (or f_j).
The reason for limiting the analysis to a single frequency at a time is that the unknown parameters in $S_\eta(\omega, \theta)$ to be estimated may be frequency dependent.
The coefficients A^i_{cj} and A^i_{sj}, $i = 1, \ldots, M$ are expressed in vector form

$$\begin{aligned} \underline{A}^T &= \left[A^1_c\, A^2_c \ldots A^M_c\, A^1_s\, A^2_s \ldots A^M_s\right] \\ &= \left[A^1 \ldots A^M\, A^{M+1} \ldots A^{2M}\right] \end{aligned} \tag{14}$$

As the coefficients are joint normally distributed the density function is given in terms of the mean value function vector, $E\left[\underline{A}\right]$, and the cross covariance function matrix $\underline{\kappa}_{\underline{A}\,\underline{A}^T} = E\left[\underline{A}\,\underline{A}^T\right]$. The cross covariance function matrix of size $2M \times 2M$ is symmetric and of the form

$$\underline{\kappa}_{\underline{A}\,\underline{A}^T} = \begin{bmatrix} \underline{B} & \underline{F} \\ \underline{F}^T & \underline{D} \end{bmatrix} \tag{15}$$

where the submatrices $\underline{B}$, $\underline{F}$ and $\underline{D}$ are $M \times M$ matrices.
From (12) and (13) the following results are found

$$E\left[A^i_{cj}\right] = \frac{2}{T}\int_{-\frac{T}{2}}^{\frac{T}{2}} E\left[\eta_i\left(\underline{x}_i, t\right)\right] cos\omega_j t\, dt = 0 \quad , \quad i = 1, \ldots, M \tag{16}$$

and

$$E\left[A^i_{sj}\right] = \frac{2}{T}\int_{-\frac{T}{2}}^{\frac{T}{2}} E\left[\eta_i\left(\underline{x}_i, t\right)\right]\, sin\omega_j t\, dt = 0 \quad , \quad i = 1, \dots , M \qquad (17)$$

i.e. $E\left[\underline{A}\right] = \underline{0}$.
In the following the cross covariance function matrix $\underline{\kappa}_{\underline{A}\,\underline{A}^T} = E\left[\underline{A}\,\underline{A}^T\right]$ will be determined. As an example the submatrix $\underline{B}$ in (15) is considered.

$$\begin{aligned} B_{mn} &= \kappa_{A^m_{cj}A^n_{cj}}\left(t_1, t_2\right) \\ &= E\left[\frac{2}{T}\int_{-\frac{T}{2}}^{\frac{T}{2}} \eta_m\left(t_1\right)\, cos\left(\omega_j t_1\right) dt_1 \cdot \frac{2}{T}\int_{-\frac{T}{2}}^{\frac{T}{2}} \eta_n\left(t_2\right)\, cos\left(\omega_j t_2\right) dt_2\right] \\ &= \frac{4}{T^2}\int_{-\frac{T}{2}}^{\frac{T}{2}}\int_{-\frac{T}{2}}^{\frac{T}{2}} E\left[\eta_m\left(t_1\right)\eta_n\left(t_2\right)\right]\, cos\left(\omega_j t_1\right) cos\left(\omega_j t_2\right)\, dt_1 dt_2 \\ &= \frac{4}{T^2}\int_{-\frac{T}{2}}^{\frac{T}{2}}\int_{-\frac{T}{2}}^{\frac{T}{2}} \kappa_{\eta_m\eta_n}\left(t_2 - t_1\right) cos\left(\omega_j t_1\right) cos\left(\omega_j t_2\right)\, dt_1 dt_2 \qquad (18) \end{aligned}$$

Introducing the variables $t = t_1$ and $\tau = t_2 - t_1$, (18) is rewritten as

$$\begin{aligned} B_{mn} &= \kappa_{A^m_{cj}A^n_{cj}}\left(t, \tau\right) \\ &= \frac{4}{T^2}\int_{-\frac{T}{2}}^{\frac{T}{2}} cos\left(\omega_j t\right)\int_{-\frac{T}{2}-t}^{\frac{T}{2}-t} \kappa_{\eta_m\eta_n}\left(\tau\right) cos\left(\omega_j(t+\tau)\right)\, d\tau dt \\ &= \frac{4}{T^2}\int_{-\frac{T}{2}}^{\frac{T}{2}}\left[cos^2\left(\omega_j t\right)\int_{-\frac{T}{2}-t}^{\frac{T}{2}-t} \kappa_{\eta_m\eta_n}\left(\tau\right) cos\left(\omega_j \tau\right)\, d\tau\right. \\ &\qquad \left. - cos\left(\omega_j t\right) sin\left(\omega_j t\right)\int_{-\frac{T}{2}-t}^{\frac{T}{2}-t} \kappa_{\eta_m\eta_n}\left(\tau\right) sin\left(\omega_j \tau\right)\, d\tau\right] dt \qquad (19) \end{aligned}$$

It is seen, that B_{mn} depends on the cross covariance between the elevation processes $\eta_m\left(t\right)$ and $\eta_n\left(t\right)$. The cross covariance matrix $\underline{\kappa}_{\eta_m\eta_n}(\tau)$ is related to the one-sided cross spectral density matrix $G_{\eta_m\eta_n}(\omega)$ in terms of the Wiener-Khintchine relation

$$\begin{aligned} G_{\eta_m\eta_n}(\omega) &= 2S_{\eta_m\eta_n}(\omega) = 2\int_{-\infty}^{\infty} \kappa_{\eta_m\eta_n}(\tau)\, e^{-i\omega\tau}\, d\tau \\ &= 2\int_{-\infty}^{\infty} \kappa_{\eta_m\eta_n}(\tau)\, cos\omega\tau\, d\tau - i\cdot 2\int_{-\infty}^{\infty} \kappa_{\eta_m\eta_n}(\tau)\, sin\omega\tau\, d\tau \\ &= C_{\eta_m\eta_n}(\omega) - i\, Q_{\eta_m\eta_n}(\omega) \qquad (20) \end{aligned}$$

where

$$C_{\eta_m\eta_n}(\omega) = 2\int_{-\infty}^{\infty} \kappa_{\eta_m\eta_n}(\tau)\, cos\omega\tau\, d\tau$$

and

$$Q_{\eta_m\eta_n}(\omega) = 2\int_{-\infty}^{\infty} \kappa_{\eta_m\eta_n}(\tau)\, sin\omega\tau\, d\tau$$

are the co-spectrum and the quad-spectrum, respectively.

Assuming the period T to be "very long", (19) can be rewritten

$$\begin{aligned} B_{mn} &= \frac{2}{T^2}\int_{-\frac{T}{2}}^{\frac{T}{2}} \left[cos^2(\omega_j t)\, C_{\eta_m\eta_n}(\omega_j) - cos(\omega_j t)\, sin(\omega_j t)\, Q_{\eta_m\eta_n}(\omega_j)\right] dt \\ &= \frac{1}{T} C_{\eta_m\eta_n}(\omega_j) \\ &= \Delta f\, C_{\eta_m\eta_n}(\omega_j) \qquad (21) \end{aligned}$$

It is concluded that B_{mn} in (15) equals Δf multiplied by the co-spectrum of the elevation processes $\eta_m(t)$ and $\eta_n(t)$. Furthermore, B_{mn} is time independent.

Using the same procedure the elements $\underline{F}$ and $\underline{D}$ of (15) can be found and after some calculation the following result is obtained

$$\underline{\kappa}_{\underline{A}\,\underline{A}^T}(\omega_j) = \Delta f \begin{bmatrix} \underline{C} & \underline{Q} \\ -\underline{Q} & \underline{C} \end{bmatrix} = \Delta f \cdot \underline{\Omega}(\omega_j) \tag{22}$$

where $\underline{C}$ and $\underline{Q}$ are $M \times M$ matrices defined by

$$C_{mn} = C_{\eta_m \eta_n}(\omega_j)$$

$$Q_{mn} = Q_{\eta_m \eta_n}(\omega_j)$$

Thus, the cross-covariance between the coefficients in (11) at a given frequency ω_j is given in terms of the co- and quad-spectra of the elevation processes.

So far expressions have been established for the mean value vector ((16) and (17)) and the cross covariance matrix (22) of the vector $\underline{A}$. These relations were established at a given frequency ω_j. As discussed in section 2 the waves are characterized by both a frequency and a direction of travel (ω and θ) in terms of the directional spectrum $S_\eta(\omega, \theta)$.

In section 2 a relation (9) was established between $S_\eta(\omega, \theta)$ and the cross spectral density matrix, $G_{\eta_m \eta_n}(\omega)$, of the elevation processes $\eta_m(\underline{x}_m, t)$ and $\eta_n(\underline{x}_n, t)$.

If the directional spectrum $S_\eta(\omega, \theta)$ is known, (9) may be used to calculate $G_{\eta_m \eta_n}(\omega)$, e.g. by numerical integration. Based on (20) $\underline{C}$ and $\underline{Q}$ are identified as the real- and the imaginary parts of $\underline{G}$. Finally $\underline{\kappa}_{\underline{A}\,\underline{A}^T}(\omega_j)$ can be determined from (22).

However, $S_\eta(\omega, \theta)$ is generally unknown. In the following, a method will be presented which can be used to estimate a directional spectrum expressed in standard form in terms of some unknown parameters. The method is known as the maximum likelihood method.

As expressed earlier, the elements in $\underline{A}$ have a joint normal distribution. The general expression for a density function of a vector $\underline{A}$ with $2M$ joint normal elements having a mean value vector $\underline{E}(\underline{A}) = \underline{0}$ is

$$f_{\underline{A}}(\underline{a}) = \frac{1}{\left(\sqrt{2\pi}\right)^{2M} |\underline{\kappa}_{\underline{A}\,\underline{A}^T}(\omega_j)|^{\frac{1}{2}}} exp\left(-\frac{1}{2}\underline{a}^T \underline{\kappa}^{-1}_{\underline{A}\,\underline{A}^T}(\omega_j)\underline{a}\right) \tag{23}$$

where $|\underline{\kappa}_{\underline{A}\,\underline{A}^T}(\omega_j)|$ and $\underline{\kappa}^{-1}_{\underline{A}\,\underline{A}^T}(\omega_j)$ are the determinant and inverse matrix of $\underline{\kappa}_{\underline{A}\,\underline{A}^T}(\omega_j)$, respectively.
If $S_\eta(\omega,\theta)$ was given (23) could be used to calculate the probability of the observed realisation $\underline{a}$ of $\underline{A}$, where $\underline{a}$ represents the actual Fourier coefficients obtained from a given time-series. Since $S_\eta(\omega,\theta)$, or some parameters in $S_\eta(\omega,\theta)$, are unknown, a Likelihood function, L, will be formulated. Expressed in terms of the Likelihood function, L, the unknown parameters in $S_\eta(\omega,\theta)$ are determined as the values corresponding to the maximum value of L.
In his article [Isobe, M.; 1990] uses J time-series measured at each of the M locations $\underline{x}_i$, $i = 1, \dots , M$. Based on each of the J time-series an estimate $\underline{a}^{(j)}$, $j = 1, \dots , J$, of $\underline{A}^{(j)}$ is obtained. The probability of obtaining the estimate $\underline{a}^{(j)}$ is given by (23). Assuming the J observations to be independent the joint probability for obtaining exactly the J observed estimates $\underline{a}^{(j)}$ is given as $f_{\underline{A}}\left(\underline{a}^{(1)}\right) \cdot f_{\underline{A}}\left(\underline{a}^{(2)}\right) \cdot \ldots \cdot f_{\underline{A}}\left(\underline{a}^{(J)}\right)$. Therefore [Isobe, M.; 1990] suggested a Likelihood function, L, as the J'th root of this product, i.e.

$$L\left(\underline{a}^{(1)}, \dots, \underline{a}^{(J)}, \underline{G}\right) = \left\{f_{\underline{A}}\left(\underline{a}^{(1)}\right) \cdot \ldots \cdot f_{\underline{A}}\left(\underline{a}^{(J)}\right)\right\}^{1/J}$$

$$= \frac{1}{(2\pi\Delta f)^M \sqrt{det\,(\underline{\Omega})}} exp\left(-\frac{1}{2}\sum_{k=1}^{2M}\sum_{l=1}^{2M}\Omega^{-1}_{kl}\hat{\Omega}_{lk}\right) \tag{24}$$

where

$$\hat{\Omega}_{lk} = \frac{1}{\Delta f \cdot J}\sum_{j=1}^{J} a_{jl}a_{jk} \tag{25}$$

$\hat{\underline{\Omega}}$ denotes the measured cross spectral density matrix.
(24) represents the probability of obtaining exactly the estimates $\underline{a}^{(j)}$, $j = 1, \dots , J$. The unknown quantity in (24) is $\underline{\Omega}$ (or $S_\eta(\omega,\theta)$).
The "optimal" choice of $S_\eta(\omega,\theta)$ or (in practice) the unknown parameters in $S_\eta(\omega,\theta)$ are determined in order to maximize L, i.e. the optimal parameters maximize the probability of obtaining exactly the observed Fourier-coefficients.

4 Implementation and Application

In order to determine the performance of the maximum likelihood method, the method was implemented and applied to numerically generated data.
The basic relation in the implementation is eq. (24) which determines the likelihood of observing a given data set. The measured cross covariance matrix $\underline{\hat{\Omega}}$ is determined by means of Fourier analysis of the data set and subsequent use of eq. (25). The estimated cross covariance matrix $\underline{\Omega}$ is established from eq. (22) in terms of $\underline{C}$ and $\underline{Q}$. Co- and quad-spectra are determined by means of numerical integration of (9) or (10). This integration requires a choice of model directional spectrum. Often a standard directional spectrum determined by a finite number of parameters λ_i in its mathematical expression is chosen. In the implementation presented here, it was chosen to apply the Mitsuyasu directional spectrum [Isobe, M.; 1990] and [Yokoki et al.; 1992]

$$S_\eta(\omega,\theta) = S_\eta(\omega)\frac{2^{2S-1}\Gamma^2(s+1)}{\pi\,\Gamma(2s+1)}\left[cos\frac{\theta-\theta_o}{2}\right]^{2s} = S_\eta(\omega)H(\omega,\theta) \qquad (26)$$

where $S_\eta(\omega)$ is the auto-spectral density function (the frequency spectrum), Γ is the Gamma-function, s is the degree of directional concentration (see figure (2)), θ_o is the peak wave direction and H denotes the directional spreading function.
In the implementation of the maximum likelihood method described by [Isobe, M.; 1990] and [Yokoki et al.; 1992] the maximum likelihood estimate of the parameters λ_i in the Mitsuyasu directional spectrum were determined by solving the equations

$$\frac{\partial L}{\partial \lambda_i} = 0 \qquad (27)$$

by means of the Newton-Raphson method. The implementation was applied succesfully to both numerical data and field data. However, numerical instabilities sometimes occured in the algorithm of the Newton-Raphson method, and various modifications had to be made in order to achieve convergence.
In the implementation presented here, the maximum likelihood estimate of

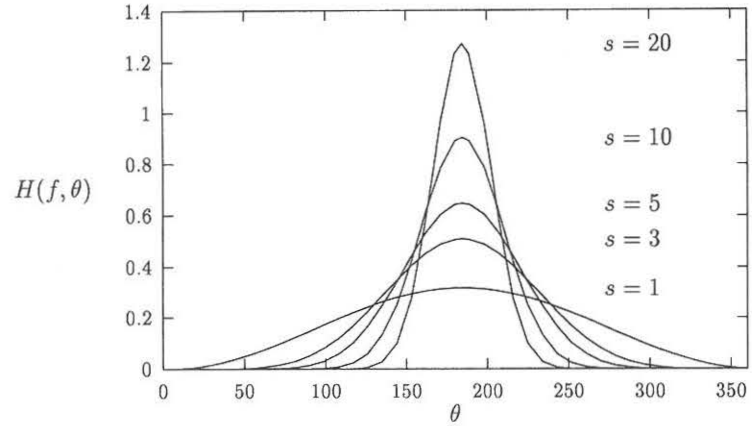

Figure 2: Mitsuyasu's spreading function.

the parameters λ_i were obtained through optimization of the likelihood function. The 0'th order method due to [Nelder and Mead; 1965] was applied. This method can be extremely slow, but it can also, in some cases, be extremely robust [Press, W. H. et al.; 1989]. Thus, robustness is favored at the expense of computational speed in order to avoid numerical instabilities.

In the numerical tests performed, the unknown parameters in the directional spectrum were determined from numerically generated surface elevation time series.

The purpose of the numerical tests was to predict the performance of the implementation when applied to data obtained from a specific series of laboratory wave generation tests. In all tests, a water depth of $d = 0.35m$ was chosen. The target incident directional wave spectra were Pierson-Moskowitz type frequency spectra combined with different Mitsuyasu spreading functions. Surface elevation time series of length $T = 2048s$ (sample frequency $f_s = 6Hz$) were generated by means of white noise filtering in the time domain [Borgman, L. E.; 1969]. Gaussian white noise was added to the generated surface elevation time series in order to simulate laboratory noise. The

RMS (Root Mean Square) of the added Gaussian white noise corresponded to 5% of the RMS of the generated time series.
When determining the measured cross spectral density matrix (eq. (25)), each surface elevation time series was divided into $J = 24$ subseries of length $T_{sub} = \frac{512}{f_s} \approx 85.3s$. This yields a frequency domain resolution of $\Delta f = \frac{1}{T_{sub}} \approx 0.0117Hz$.

Two test series were performed: one in which no reflected wave field was present (eqs. (1) and (10)), and one in which the numerically generated wave field was a combined wave field comprised by the incident wave field and a reflected wave field (eqs. (7) and (9)).

4.1 Numerical tests, test series 1 (no reflection).

Two wave gauge arrays were applied:

1. a CERC5 type array with a radius of $R = 0.50m$, see fig. 4.
2. a modified CERC5 type array ($R = 0.50m$), see fig. 5.

The test program is shown in fig. 3

Test no.	f_p	H_s	θ_0	s	Array
	Hz	m	deg		
1.1	0.8	0.05	0	12	1
2.1	0.8	0.05	0	6	2
2.2	0.8	0.05	0	12	2
2.3	0.8	0.05	0	25	2
2.4	0.8	0.05	15	12	2
2.5	0.8	0.05	15	25	2

Figure 3: Test program, test series 1.

The results of tests 1.1-2.5 are shown in figs. 6-11. Instead of the estimated spreading parameter s, the corresponding spreading width σ_θ (defined as the standard deviation of the spreading function $H(\omega, \theta)$) is plotted.

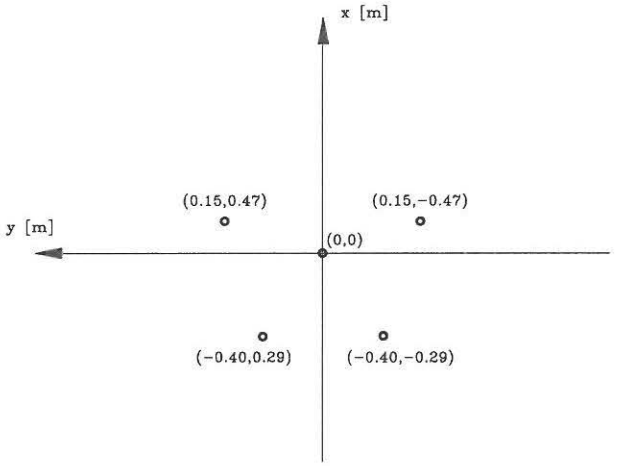

Figure 4: Wave gauge array 1 (CERC5 array).

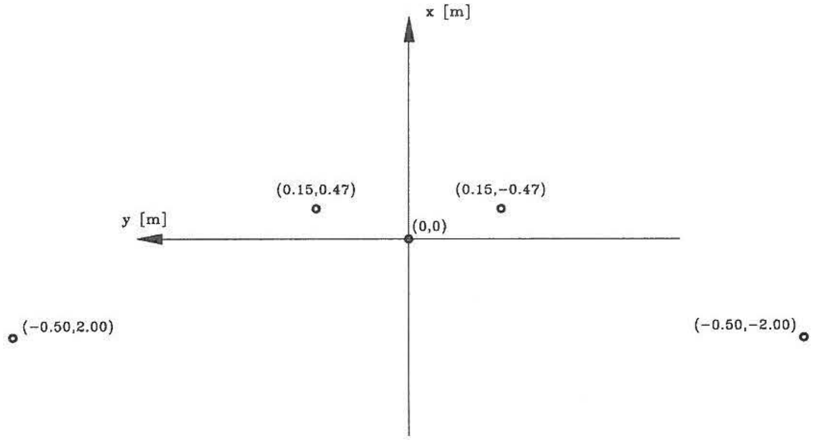

Figure 5: Wave gauge array 2 (modified CERC5 array).

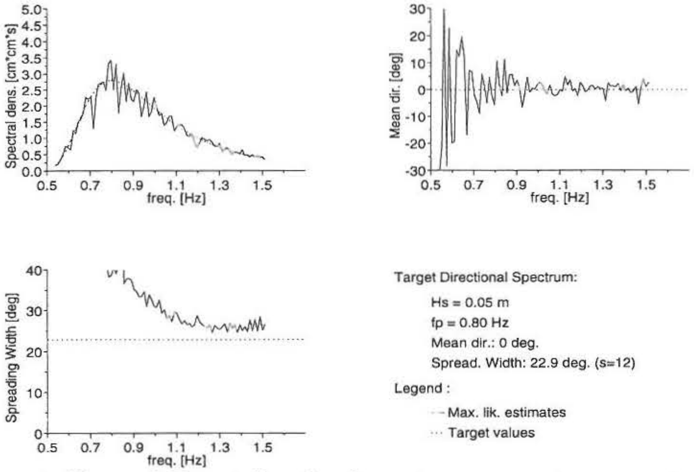

Figure 6: Est. and Target directional spectrum parameters, num. test 1.1.

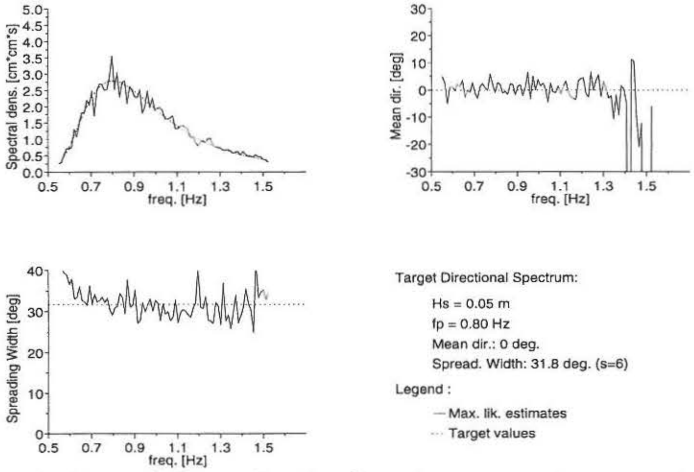

Figure 7: Est. and Target directional spectrum parameters, num. test 2.1.

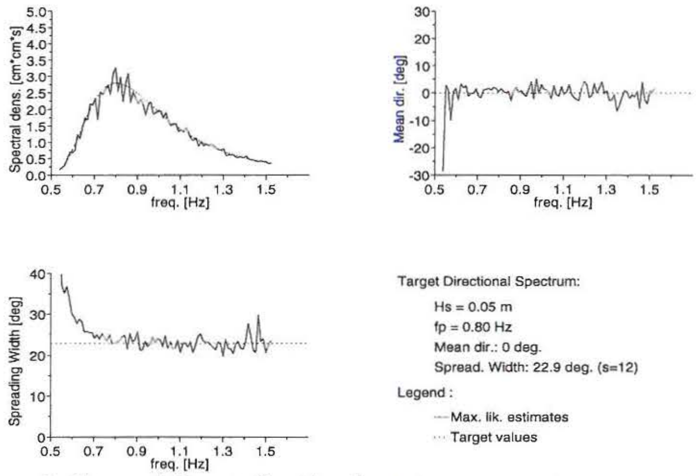

Target Directional Spectrum:

Hs = 0.05 m
fp = 0.80 Hz
Mean dir.: 0 deg.
Spread. Width: 22.9 deg. (s=12)

Legend :

— Max. lik. estimates
··· Target values

Figure 8: Est. and Target directional spectrum parameters, num. test 2.2.

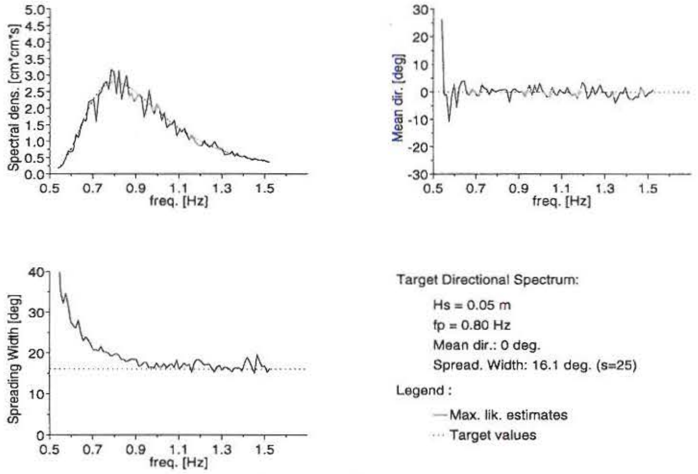

Target Directional Spectrum:

Hs = 0.05 m
fp = 0.80 Hz
Mean dir.: 0 deg.
Spread. Width: 16.1 deg. (s=25)

Legend :

— Max. lik. estimates
··· Target values

Figure 9: Est. and Target directional spectrum parameters, num. test 2.3.

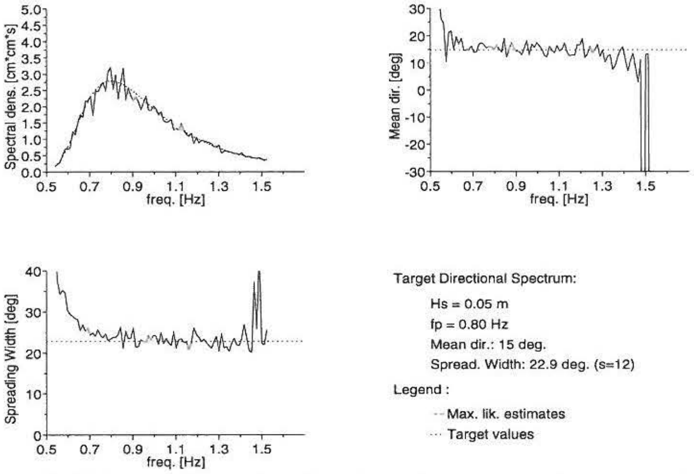

Figure 10: Est. and Target directional spectrum parameters, num. test 2.4.

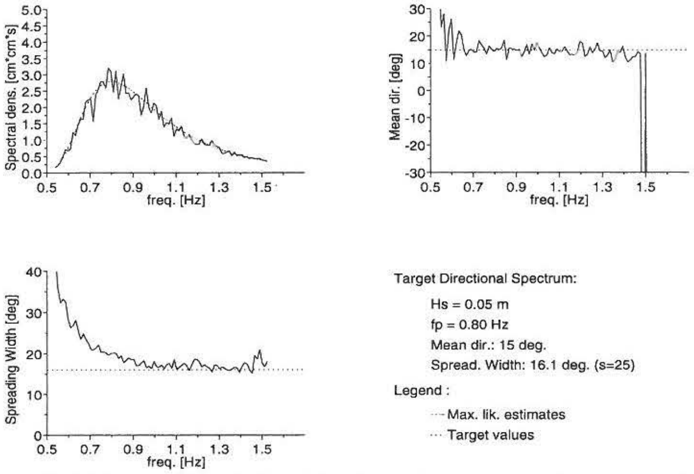

Figure 11: Est. and Target directional spectrum parameters, num. test 2.5.

Comparison of figs. 6 and 8 shows that with the parameters $s = 12$ and $\theta_0 = 0deg$, better estimates of the directional spreading function parameters are obtained when wave gauge array 2 is applied than when wave gauge array 1 is applied. When wave gauge array 1 is applied, the estimated directional spectrum parameters differ significantly from the target values, particularly at low frequencies. When array 2 is applied, excellent agreement is achieved. The discrepancies observed when applying array 1 are believed to be caused by the geometry of the array. It is obvious that in order to determine the directional spectrum of a given wave field, the distances between the individual wave gauges in the wave gauge array applied must not be too small compared to the wave lengths. Otherwise the differences in phase between the surface elevation signals at different gauges will be indistinguishable from the phase differences caused by noise, and directional spectrum estimation will be impossible.

Based on these observations, it is concluded that array 2 (the modified CERC5 array) is preferable under conditions similar to those given in num. tests 1.1 and 2.2.

As mentioned above, inspection of figs. 7-11 shows that the estimated parameters are generally in excellent agreement with the target values when wave gauge array 2 is applied. However, at low frequencies ($f < 0.7Hz$), the estimated spreading width is generally higher than the target value. Again, the reason for these discrepancies is believed to be that the distance between the individual wave gauges is too small compared to the wave length. If this is the case, the discrepancies observed would increase with decreasing frequency (increasing wave length). Figs. 7-11 show that the difference between target and estimated spreading function parameters does indeed increase with decreasing frequency (particularly the differences in spreading width).

4.2 Numerical tests, test series 2 (reflection).

The examples considered involve a reflecting wall installed at $x = 0.0$ characterised by a reflection coefficient of $r(\omega) = 0.95$.
The wave gauge array applied is shown in fig. 12.

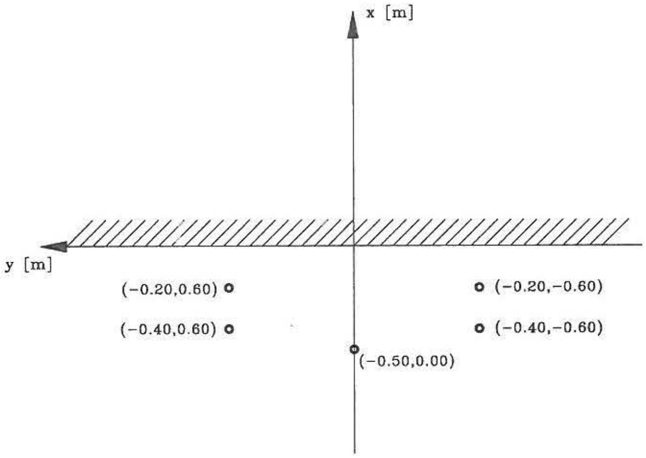

Figure 12: Wave gauge array 3.

The test program is shown in fig. 13.
The results of tests 3.1-3.3 are given in figs. 14-16.

	Incident dir. spec.					
Test no.	f_p	H_s	θ_0	s	r	Array
	Hz	m	deg			
3.1	0.8	0.04	0	6	0.95	3
3.2	0.8	0.04	0	12	0.95	3
3.3	0.8	0.04	0	25	0.95	3

Figure 13: Test program, test series 2.

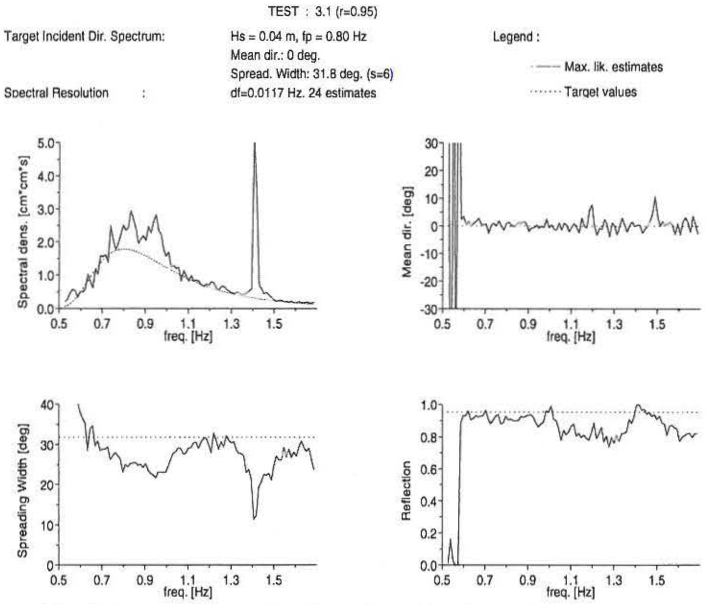

Figure 14: Est. and Target Incident directional spectrum parameters, num. test 3.1.

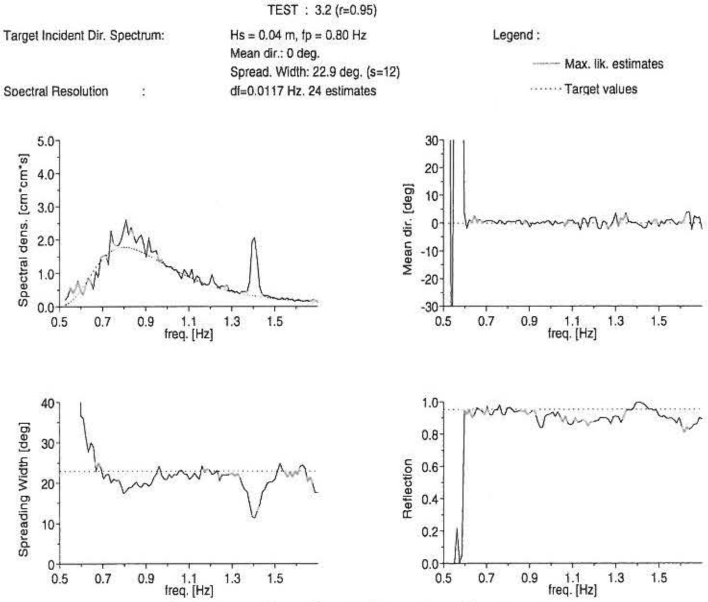

Figure 15: Est. and Target Incident directional spectrum parameters, num. test 3.2.

In general, the estimated parameters are in good agreement with the target parameters. However, discrepancies do occur.

In all tests the estimated parameters corresponding to frequencies of approximately $1.4Hz$ differ significantly from the target parameters. This may be due to the fact that for $f = 1.4Hz$ ($L = 0.8m$) and a direction of $\theta = 0deg$, a node in the standing wave pattern appears at $x = -0.20m$ and an antinode appears at $x = -0.40m$. Thus, the positions of 4 of the 5 wave gauges in the wave gauge array (see fig. 12) coincide with nodal points in the standing wave pattern.

For a frequency of $f = 0.93Hz$ ($L = 1.6m$), and a direction of $\theta = 0deg$, a node in the standing wave pattern appears at $x = -0.40m$. Thus, the position of 2 of the 5 wave gauges will coincide with nodal points in the standing wave pattern. Inspection of figs. 14-16 shows that for $f = 0.93Hz$, discrepancies occur (particularly in test 3.3).

Furthermore, for frequencies of $f = 0.75Hz$ to $f = 1.0Hz$ the spreading width is generally underestimated whereas the spectral density is overestimated. This is particularly pronounced in test 3.1 (see fig. 14).

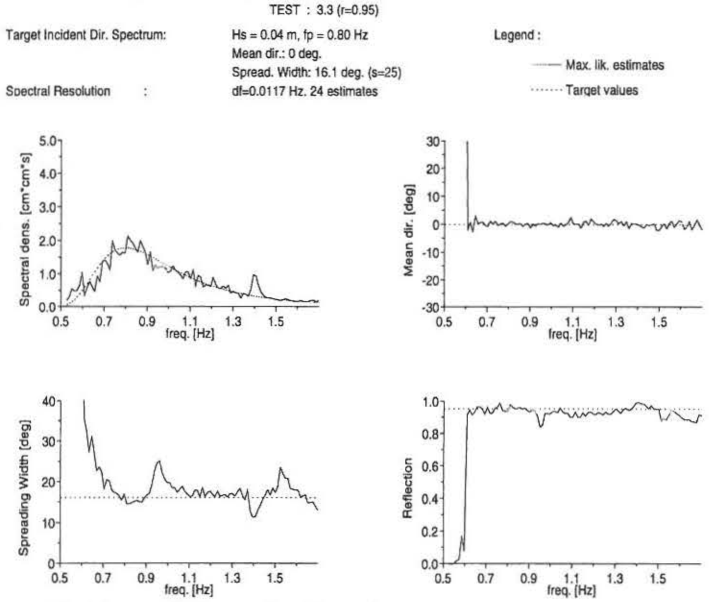

Figure 16: Est. and Target Incident directional spectrum parameters, num. test 3.3.

5 Conclusion

The maximum likelihood method for estimation of directional spectra in standard form has been presented.

The directional spectrum estimation is based on surface elevation time series measured simultanously in an arbitrary number of wave gauges. The recorded time series are expressed as Fourier sums, and a likelihood function is formulated in terms of the probability density function of the Fourier coefficients. The maximum likelihood estimates of the unknown parameters in the directional spectrum are found by maximising the likelihood function, i.e.

by maximising the probability of observing the Fourier coefficients obtained. Two different types of applications were considered: one in which the wave field is assumed to be comprised by the incident wave field only and one in which the wave field is assumed to be the sum of the incident wave field and a reflected wave field.

Numerical tests have been performed in order to determine the performance of the method. In general, reliable estimates were obtained.

6 References

Borgman, L. E., 1969.
"Ocean Wave Simulation for Engineering Design"
Journal of the Waterways and Harbors Division, ASCE, Vol. 95, No. WW4, pp. 557-583.

Isobe, M. and K. Kondo, 1984.
"Method for Estimating Directional Wave Spectrum in Incident and Reflected Wave Field"
Proc. 19th Int. Conf. on Coastal Eng., pp. 467-483.

Isobe, M., 1990.
"Estimation of Directional Spectrum Expressed in Standard Form"
Proc. 22nd Int. Conf. on Coastal Eng., pp. 647-660.

Nelder, J. A. and R. Mead, 1965.
Computer Journal, vol. 7, p. 308.

Nielsen, S. R. K., 1993.
"Vibration Theory, Vol. 3. Linear Stochastic Vibration Theory".
Aalborg tekniske Universitetsforlag.

Press, W. H., B. P. Flannery, S. A. Teukolsky and W. T. Vetterling, 1989.
"Numerical Recipes in Pascal".
Cambridge University Press, Cambridge.

Svendsen, I. A. and Jonsson, I. G., 1980.
"Hydrodynamics of Coastal Regions".
Den Private Ingeniørfond, Technical University of Denmark, Lyngby.

Yokoki, H., M. Isobe and A. Watanabe, 1992.
"A Method for Estimating Reflection Coefficient in Short Crested Random Seas"
Proc. 23rd Int. Conf on Coastal Eng., pp. 765-776.

Chapter 1

Introduction

Coastal engineering problems are often solved by means of physical models. Physical modelling of coastal engineering phenomena requires the capability of reproducing natural conditions in the laboratory environment. In order to perform experiments involving wave-wave, wave-current and wave-structure interaction, laboratory facilities for water wave generation must be made available.

The desire to reproduce all observed natural wave characteristics in physical models has caused an extensive effort to develop sophisticated techniques and equipment for laboratory wave generation. Wave generation capability has evolved from the time when researchers were completely at the mercy of a limited technology to the present where the capability of wave generators and computers exceeds the current understanding of wave dynamic processes (Funke and Mansard, 1987). The earliest wave generators generated regular, unidirectional (2-D) waves. At present, several hydraulic laboratories have wave basins equipped with mechanical wave generators capable of reproducing irregular, directional (3-D) wave fields.

One of the problems associated with laboratory reproduction of water waves is the reflection of wave energy from the boundaries of the test facility. At the open sea, waves can propagate over large distances without meeting physical obstacles. In the laboratory environment the wave basin walls will reflect the generated waves, thus introducing unwanted reflected waves. The problem of reflection can be reduced by installing wave absorbers along the basin walls. In general, wave absorbers applied in physical models are divided into two categories

- *Passive wave absorbers* which damp incident wave energy through dissipation. Passive wave absorbers are typically gently sloping beaches of porous material.
- *Active wave absorbers* which are mechanical devices which can move in response to the incident wave train so that the incident wave train is absorbed.

When a highly reflective structure is being tested in the wave basin, the presence of

reflected waves is unavoidable. If reflected waves are allowed to propagate back towards the wave generator they will be reflected off the front of the wave generator, thus giving rise to a rereflected wave field travelling back towards the test structure. The presence of this rereflected wave field will alter the characteristics of the wave field incident to the test structure in an uncontrolled way. Under these conditions, performing tests involving specific incident wave field characteristics will be impossible.
The problem of rereflection can be reduced by applying a so-called *absorbing wave generator*. An absorbing wave generator is a combined mechanical wave generator and active wave absorber, which simultaneously generates the incident wave field and absorbs the reflected wave field. Recently, several authors have presented absorbing wave generators based on different principles.

The scope of the present thesis is to present methods for mechanical generation and absorption of linear 2- and 3-dimensional waves in physical models.
The hydrodynamic transfer functions for 2- and 3-dimensional wave generation will be given, and methods for generating wave generator control signals for reproduction of specified wave fields will be presented. Furthermore, the results of a series of tests involving reproduction of different irregular 3-D wave fields in a laboratory wave basin will be presented and discussed.
A new principle for design of absorbing wave generators for wave channels (2-D waves) will be presented. An absorbing wave generator based on this principle will be tested. Finally, a principle for design of absorbing directional wave generators will be given, and an absorbing directional wave generator based on this principle will be applied to laboratory tests.

Chapter 2

2-D Wave Generation

2.1 Introduction

Wind generated ocean waves are stochastic in nature. In linear, irregular wave modelling, the surface elevation is assumed to be a stationary, ergodic Gaussian stochastic process produced by superposition of many infinitesimal linear wavelets, i.e. for 2-D waves (unidirectional waves) the surface elevation is given by

$$\eta(x,t) = \sum_{i=1}^{I} A_i \sin(\omega_i t - k_i x + \phi_i) \tag{2.1}$$

$$\text{where} \quad \omega_i = 2\pi f_i$$
$$k_i = 2\pi / L_i$$

and f, L and ϕ denote frequency, wave length, and phase, respectively.
The most common approach in laboratory wave generation is mechanical wave generation where a movable partition (wave paddle) is placed in the wave facility and waves are generated by oscillation of the partition. In order to generate a specified irregular wave train, the hydrodynamic transfer function relating the wave paddle displacement signal to the generated surface elevation signal must be determined. The hydrodynamic transfer function corresponding to a so-called piston-type wave generator is presented in sec. 2.2.
In most cases laboratory reproduction of the wave conditions at a given location is complicated by the absence of prototype surface elevation recordings. Instead, sea states defined by empirical surface elevation frequency spectra $S_\eta(\omega)$ (e.g. JONSWAP or Pierson-Moskowitz) are generated. Thus, methods for synthesising irregular wave signals are required. Methods for irregular wave synthesis are described in sec. 2.3.
Generation of linear, irregular waves in laboratory environments combines the synthesis of irregular wave signals with the transfer functions describing the relations between wave generator displacements and generated surface elevations for sinusoidal motion of

the wave generator. The procedure in synthesising wave generator control signals for generation of irregular waves is given in sec. 2.4.

2.2 2-D Hydrodynamic Transfer Functions

Biésel and Suquet (1951) applied linear potential theory to solve the boundary value problem involving a harmonically oscillating piston-type wave generator in a wave flume (see fig. 2.1).

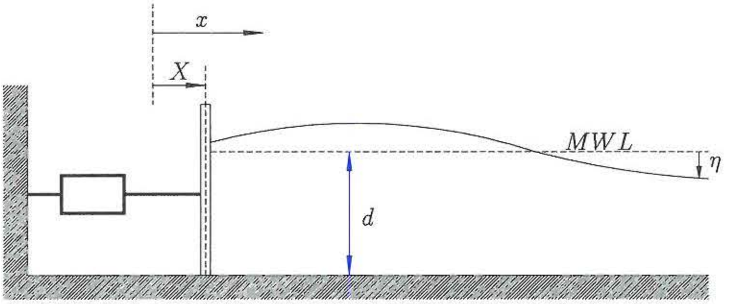

Figure 2.1: Piston type wave generator in wave flume. Definition sketch.

For a wave paddle motion given by

$$X(t) = e\sin(\omega t) \tag{2.2}$$

the surface elevation was determined as

$$\eta(x,t) = eK_f \sin(\omega t - kx + \phi_f) + eK_n \sin(\omega t) \tag{2.3}$$

where

$$K_f = \frac{2\sinh^2 kd}{\sinh kd \cosh kd + kd} \tag{2.4}$$

$$K_n = \sum_{n=1}^{\infty} \frac{2\sin^2 k_n d \exp(-k_n x)}{\sin k_n d \cos k_n d + k_n d} \tag{2.5}$$

$$\phi_f = \frac{\pi}{2} \tag{2.6}$$

and k and k_n are determined from the relations

$$\omega^2 = kg \tanh kd \tag{2.7}$$

$$\omega^2 = -k_n g \tan k_n d \tag{2.8}$$

The first term in eq. (2.3) represents a progressive wave of constant form whereas the second term represents a series of standing waves which decay exponentially away from the wave generator. Consequently, in the *far field*, i.e. far from the wave paddle, the waves will be progressive waves of constant form, whereas local disturbances will occur in the *near field* close to the wave paddle.

Comparison of eqs. (2.2) and (2.3) shows that the Biésel far field coefficient K_f represents the ratio of the amplitude of the generated progressive wave, A, and the amplitude of the wave paddle displacement, e, i.e.

$$K_f = \frac{A}{e} \tag{2.9}$$

In fig. 2.2 K_f is plotted against the relative water depth kd. It is seen that as kd approaches zero, K_f approaches zero. Thus, in order to generate long waves (low frequency waves), large wave generator displacement amplitudes are required. As kd increases, the generated wave amplitude approaches twice the wave generator displacement amplitude.

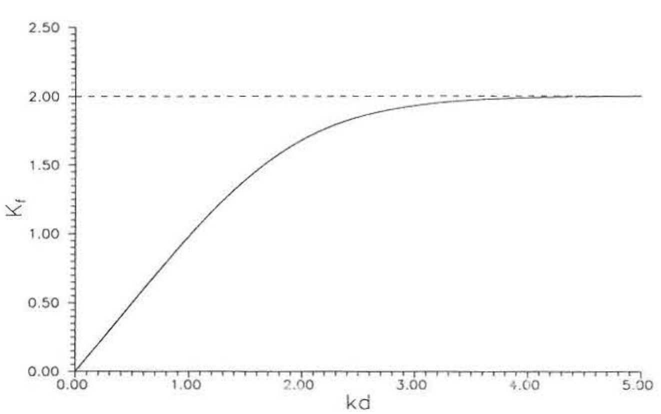

Figure 2.2: Biésel far field coefficient versus relative water depth.

It can be shown that the Biésel near field coefficient K_n decreases by more than 99 % from $x = 0$ to $x = 3d$ (Biésel and Suquet, 1951). Consequently, at distances from the wave paddle of more than three times the water depth, the local disturbances will be insignificant.

2.3 Numerical 2-D Wave Synthesis Methods

2.3.1 Introduction

In most cases laboratory reproduction of the wave conditions at a given location is complicated by the absence of prototype surface elevation recordings. Instead, sea states defined by empirical surface elevation frequency spectra $S_\eta(\omega)$ (e.g. JONSWAP or Pierson-Moskowitz) are generated. Irregular wave synthesis addresses the problem of generating realizations of the surface elevation process which exhibit specific characteristics.

Several authors have suggested different definitions for categorising the methods for synthesising irregular waves. Funke and Mansard (1987) suggested dividing the methods into two main categories:

- **Nondeterministic methods**
  Methods in which the surface elevation is assumed to be a Gaussian process with a specified variance spectrum.
- **Partly deterministic methods**
  Methods in which the surface elevation is assumed to be a Gaussian process with a specified variance spectrum, but additional constraints are placed on spectral properties (phasing or spectral amplitudes) or non-spectral properties (e.g. grouping of waves).

This classification links the concept of **deterministic methods** to the reproduction of measured wave trains.

2.3.2 Irregular Wave Synthesis Models

Tuah and Hudspeth (1982) presented two numerical irregular wave synthesis models. In both models, a N point realisation of the surface elevation process in a given position was represented by the following discrete Fourier series

$$\begin{aligned}
\eta(j\Delta t) &= \sum_{i=1}^{N/2} \left(a_i \cos(\omega_i j\Delta t) - b_i \sin(\omega_i j\Delta t)\right) && (2.10)\\
&= \sum_{i=1}^{N/2} A_i \cos(\omega_i j\Delta t + \phi_i) \quad ,j = 1..N && (2.11)
\end{aligned}$$

where

$$\omega_i = 2\pi i\Delta f \qquad ,\Delta f = \frac{1}{N\Delta t} \tag{2.12}$$

This representation allows for the use of the efficient FFT algorithm in the synthesis process when waves are simulated in the frequency domain.
In the **Deterministic Spectral Amplitude Model** (DSA) amplitudes and phases are determined from

$$A_i = \sqrt{2S_\eta(\omega_i)\Delta\omega} \tag{2.13}$$
$$\phi_i : 2\pi\mathcal{U}[0..1] \tag{2.14}$$

where $\mathcal{U}[0..1]$ denotes a random variable which is uniformly distributed in the interval from 0 to 1. Thus, the wave amplitudes are deterministic whereas the phases are chosen at random (partially deterministic wave synthesis).
When the DSA model is applied, the sample spectrum will be identical to the target spectrum for each realization. This is in poor agreement with the assumption that the surface elevation is a stochastic process: the Fourier coefficients a_i and b_i obtained from a single realisation of a zero-mean Gaussian stochastic process will be zero-mean Gaussian random variables with variance $\sigma_i^2 = S_\eta(\omega_i)\Delta\omega$ (Sand (1985)). Consequently, a more realistic realisation of the surface elevation process is obtained by applying the **Non-deterministic Spectral Amplitude Model** (NSA) in which amplitudes and phases are determined from

$$A_i = \sqrt{a_i^2 + b_i^2} \tag{2.15}$$
$$\phi_i = \arctan\left(\frac{b_i}{a_i}\right) \tag{2.16}$$
$$[a_i, b_i] = \sqrt{S_\eta(\omega_i)\Delta\omega}[\alpha_i, \beta_i] \tag{2.17}$$
$$\alpha_i, \beta_i : \mathcal{N}(0,1) \tag{2.18}$$

where $\mathcal{N}(0,1)$ denotes a normal random variable with mean 0 and variance 1 (standard normal random variable). Thus, the sample spectrum obtained from a single realisation generated by means of the NSA method will differ significantly from the target spectrum.

2.3.3 Irregular Wave Synthesis Methods

Tuah and Hudspeth (1982) implemented the NSA model in the *frequency domain.* Irregular waves were simulated by means of filtering of Gaussian white noise in the frequency domain and subsequent use of the IFFT-algorithm in order to obtain the time domain representation of the wave train.

Another implementation of the NSA model was presented by Borgman (1969) who performed surface elevation simulations in the *time domain* using non-recursive linear digital filters (an introduction to the subject of linear digital filters is given in App. A). In the method presented by Borgman, the surface elevation at time step n is determined as the result y_n of the following discrete convolution

$$y_n = \sum_{j=1}^{J} h_j \alpha_{n-j} \tag{2.19}$$

where h_j denotes a filter operator of length J, and α_j are independent standard normal distributed random numbers, i.e.

$$\alpha_j : \mathcal{N}(0,1) \tag{2.20}$$

Several methods for numerical generation of normal distributed numbers are available, see e.g. Ross (1987). The sequence of random numbers α_j represents a discrete-time realisation of a white noise process, i.e. a process with uniform spectral density. With a Nyquist frequency of $\omega_N = \pi/\Delta t$, the spectral density of this process is given by

$$S_\alpha(\omega) = \frac{\Delta t}{\pi} \tag{2.21}$$

The basic problem in the time domain approach to numerical wave generation is to design the filter operator h so that the output process y is characterised by the desired frequency spectrum $S_\eta(\omega)$.
The spectral density of the output process y is given by

$$S_y(\omega) = |\mathcal{H}(\omega)|^2 S_\alpha(\omega) \tag{2.22}$$

where $\mathcal{H}(\omega)$ represents the frequency response of the linear filter operator h.
The desired filter operator frequency response, $\mathcal{D}(\omega)$, is the filter frequency response for which the spectral density of the output process y equals the desired frequency spectrum $S_\eta(\omega)$, i.e

$$|\mathcal{D}(\omega)|^2 S_\alpha(\omega) = S_\eta(\omega) \tag{2.23}$$

Combining eqs. (2.23) and (2.21) yields the gain of the desired frequency response

$$|\mathcal{D}(\omega)| = \sqrt{\frac{\pi}{\Delta t}}\sqrt{S_\eta(\omega)} \tag{2.24}$$

The remaining problem is to design a filter operator h characterised by a gain $|\mathcal{H}(\omega)|$ which represents an acceptable approximation to the desired gain $|\mathcal{D}(\omega)|$ given by eq. (2.24). A method for design of a non-recursive digital filter operator characterised by a specified frequency response is given in App. A.

2.4 2-D Wave Generator Signal Synthesis

Mechanical generation of linear, irregular waves in laboratory environments combines the mathematical description of the surface elevation process given by eq. (2.1) with the hydrodynamic transfer function describing the relation between wave generator displacements and generated surface elevations for sinusoidal motion of the generator (see sec. 2.2).

From linear potential theory (see sec. 2.2), the following relation between the far field wave amplitude A and the amplitude of the wave paddle motion e has been established

$$A = K_f(\omega)e \tag{2.25}$$

where K_f is given by eq. (2.4).
Thus, the wave generator displacement signal required to reproduce the surface elevation signal given by eq. (2.1) is

$$X(t) = \sum_{i=1}^{I} \frac{A_i}{K_f(\omega_i)} \sin(\omega_i t + \phi_i - \phi_f) \tag{2.26}$$

The linear relation (2.25) yields the following relation between the target wave frequency spectrum and corresponding wave generator displacement frequency spectrum

$$S_X(\omega) = \frac{S_\eta(\omega)}{K_f(\omega)^2} \tag{2.27}$$

In numerical wave generator signal synthesis, $S_X(\omega)$ represents the target frequency spectrum. By applying the irregular wave synthesis methods described in sec. 2.3.3, wave paddle displacement signals corresponding to specified target wave frequency spectra may now be generated.

Chapter 3

2-D Active Wave Absorption

3.1 Introduction

One of the problems associated with the physical modelling of water waves in laboratory wave channels is the presence of rereflected waves.
In nature the sea constitutes an open boundary which absorbs waves reflected by the coastal system.
A wave channel is a closed system: waves reflected from a model structure will be rereflected at the wave paddle, thus altering the characteristics of the wave train incident to the model structure. Consequently, the reproduction of a specified incident wave train will often be impossible when a reflective structure is being tested.

One way of eliminating the problem of rereflection is to stop the test before the rereflected waves reach the test structure. This approach is unsatisfactory, because it limits the maximum length of the test run.
An alternative approach is to subdivide the channel at the test section in such a way that the reflective structure occupies only part of its width and an efficient passive wave absorber spans the remainder of the channel cross section. This would reduce the total amount of reflected wave energy, thus reducing the problem of rereflection. However, significant water motions across the width of the channel will be introduced, and the width of the test structure will be reduced.
Chilo and Corsini (1994) suggested compensating for the presence of rereflected waves by calibrating the generated incident wave spectrum so that the incident wave spectrum corresponding to the superposed incident and rereflected wave trains would match the target spectrum. The disadvantage of this approach is that several tests must be performed before a reasonable matching of the target incident spectrum is achieved.

The problem of rereflection can be reduced without compromise by applying a so-called absorbing wave generator: a combined wave generator and active wave absorber, which, in addition to generating incident waves, absorbs waves reflected from the test

structure.
The construction of an absorbing wave generator requires (Gilbert (1978)):

1. A means of detecting reflected waves as they approach the wave generator
2. A means of making the paddle generate waves that are, in effect, equal and opposite to the reflected waves so that the reflected waves are cancelled out as they reach the paddle. This requirement is over and above the need to generate the primary incident waves.

Milgram (1970) presented a system in which waves in a channel were absorbed by means of a moving termination at the end of the channel. The motion of the termination needed for absorption was determined by analog filtering of a surface elevation signal measured in front of the termination. This active wave absorber was not used in a combined generation and absorption mode.
Deriving the reflected wave signal from a combined wave field requires a means of separating incident and reflected wave signals. The common approach to separating incident and reflected wave signals when performing simultaneous wave generation and active wave absorption is by measuring the surface elevation on the face of the wave paddle. The reflected wave signal is then determined as the difference between the measured surface elevation signal and the generated surface elevation signal (which is estimated based on the wave generator control signal). Systems based on this approach were described by Bullock and Murton (1989), Hirakuchi et al. (1990) and Schäffer et al. (1994).

In the following an absorbing wave generator based on a new principle will be presented, and its performance is evaluated based on the results of physical model tests. The absorbing wave generator has previously been presented by Christensen and Frigaard (1994).

3.2 Principle

The absorbing wave generator is operated by non-recursive linear digital filters working in real time. A short introduction to the subject of non-recursive digital filters is given in App. A.

The paddle displacement correction signal needed for absorption of reflected waves is determined by means of digital filtering and subsequent superposition of surface elevation signals measured in two positions in front of the wave generator (fig. 3.1). The wave gauges are placed in the far field (see sec. 2.2).
When active absorption is applied, the paddle displacement correction signal is added to the input paddle displacement signal read from the signal generator, causing the wave generator to operate in a combined generation/absorption mode.
Having outlined the principle of the system, the only remaining problem in the design process is to specify the frequency response of the linear filters applied.

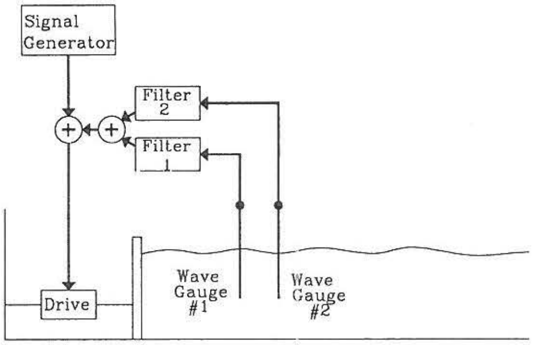

Figure 3.1: Principle of absorbing wave generator.

3.3 Theory

In fig. 3.2, a wave channel equipped with two wave gauges is shown.

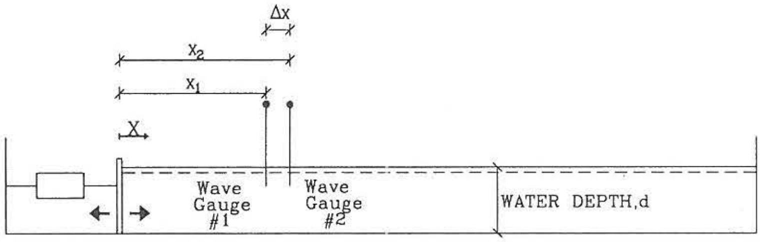

Figure 3.2: Wave channel with piston-type wave generator.

The surface elevation signal at a position x may be regarded as a sum of harmonic components. Considering an isolated component, the surface elevation arising from this component may be written as the sum of the corresponding incident and reflected wave components

$$\begin{aligned}\eta(x,t) &= \eta_I(x,t) + \eta_R(x,t) \\ &= A_I \cos(\omega t - kx + \phi_I) + A_R \cos(\omega t + kx + \phi_R) \qquad (3.1)\end{aligned}$$

where indices I and R denote incident and reflected, respectively.

As the reflected wave components reach the wave generator, they are reflected at the front of the wave generator giving rise to a rereflected wave component. Assuming that the wave generator is fully reflective, the rereflected wave component is given by

$$\eta_{RR}(x,t) = A_R \cos(\omega t - kx + \phi_R) \qquad (3.2)$$

In principle, active absorption of reflected wave components is performed by generating wave components which are identical to the rereflected components except for a phase shift of π. When superposed, rereflected and generated wave components cancel out, and the problem of rereflection is eliminated. Thus, the generated wave component corresponding to absorption of the reflected wave component is given by

$$\eta_{-RR}(x,t) = A_R\cos(\omega t - kx + \phi_R + \pi) \tag{3.3}$$

The corresponding wave generator displacement signal is given by (see sec. 2.2)

$$X_{-RR}(t) = \frac{1}{K_f(\omega)}A_R\cos(\omega t + \phi_R - \phi_f + \pi) \tag{3.4}$$

Thus, eq. (3.4) defines the paddle displacement correction signal needed for absorption of the reflected wave component.

In the following it is shown that it is possible to amplify and phase shift the surface elevation signals from the two wave gauges in such a way that their sum is identical to the paddle correction signal corresponding to absorption of the reflected component as given by eq. (3.4).

At the two wave gauges (fig. 3.2) the surface elevation signals are given by

$$\eta(x_1,t) = A_I\cos(\omega t - kx_1 + \phi_I) + A_R\cos(\omega t + kx_1 + \phi_R) \tag{3.5}$$

$$\begin{aligned}\eta(x_2,t) &= A_I\cos(\omega t - kx_2 + \phi_I) + A_R\cos(\omega t + kx_2 + \phi_R)\\ &= A_I\cos(\omega t - kx_1 - k\Delta x + \phi_I) +\\ &\quad A_R\cos(\omega t + kx_1 + k\Delta x + \phi_R)\end{aligned} \tag{3.6}$$

where $x_2 = x_1 + \Delta x$ has been substituted into eq. (3.6).

By means of linear filtering, the surface elevation signals measured at wave gauges #1 and #2 are amplified by $|\mathcal{D}(\omega)|$ and phase shifted by $\Phi_1(\omega)$ and $\Phi_2(\omega)$, respectively. The modified signals, denoted by superscript $*$, are

$$\begin{aligned}\eta^*(x_1,t) &= |\mathcal{D}(\omega)|A_I\cos(\omega t - kx_1 + \phi_I + \Phi_1(\omega)) +\\ &\quad |\mathcal{D}(\omega)|A_R\cos(\omega t + kx_1 + \phi_R + \Phi_1(\omega))\end{aligned} \tag{3.7}$$

$$\begin{aligned}\eta^*(x_2,t) &= |\mathcal{D}(\omega)|A_I\cos(\omega t - kx_1 - k\Delta x + \phi_I + \Phi_2(\omega)) +\\ &\quad |\mathcal{D}(\omega)|A_R\cos(\omega t + kx_1 + k\Delta x + \phi_R + \Phi_2(\omega))\end{aligned} \tag{3.8}$$

The sum of $\eta^*(x_1,t)$ and $\eta^*(x_2,t)$, which is denoted $X^*(t)$, is

$$\begin{aligned}X^*(t) &= \eta^*(x_1,t) + \eta^*(x_2,t)\\ &= 2|\mathcal{D}(\omega)|A_I\cos(\frac{k\Delta x + \Phi_1(\omega) - \Phi_2(\omega)}{2})\\ &\quad \cos(\omega t - kx_1 + \phi_I + \frac{-k\Delta x + \Phi_1(\omega) + \Phi_2(\omega)}{2}) +\\ &\quad 2|\mathcal{D}(\omega)|A_R\cos(\frac{-k\Delta x + \Phi_1(\omega) - \Phi_2(\omega)}{2})\\ &\quad \cos(\omega t + kx_1 + \phi_R + \frac{k\Delta x + \Phi_1(\omega) + \Phi_2(\omega)}{2})\end{aligned} \tag{3.9}$$

It is seen that $X^*(t)$ and $X_{-RR}(t) = \frac{1}{K_f(\omega)} A_R \cos(\omega t + \phi_R - \phi_f + \pi)$ are identical signals in case

$$\begin{aligned} 2|\mathcal{D}(\omega)| \cos(\frac{k\Delta x - \Phi_1(\omega) + \Phi_2(\omega)}{2}) &= \frac{1}{K_f(\omega)} && (3.10) \\ kx_1 + \frac{k\Delta x + \Phi_1(\omega) + \Phi_2(\omega)}{2} &= -\phi_f + \pi + n \cdot 2\pi, \ n \in (0, \pm 1, ..) && (3.11) \\ \frac{k\Delta x + \Phi_1(\omega) - \Phi_2(\omega)}{2} &= \frac{\pi}{2} + m \cdot \pi, \ m \in (0, \pm 1, \pm 2, ..) && (3.12) \end{aligned}$$

Solving eqs. (3.10)-(3.12) with respect to $\Phi_1(\omega), \Phi_2(\omega)$ and $|\mathcal{D}(\omega)|$ with $n = m = 0$ yields

$$\begin{aligned} \Phi_1(\omega) &= -\phi_f - k\Delta x - kx_1 + 3\pi/2 && (3.13) \\ \Phi_2(\omega) &= -\phi_f - kx_1 + \pi/2 && (3.14) \\ |\mathcal{D}(\omega)| &= \frac{1}{K_f(\omega)} \cdot \frac{1}{2\cos(-k\Delta x + \pi/2)} && (3.15) \end{aligned}$$

Eqs. (3.13)-(3.15) specify the frequency responses, i.e. the amplification factors and phase shifts, of the linear filters #1 and #2 in fig. 3.1.

As mentioned above, the linear filters applied are so-called non-recursive filters. For a non-recursive filter operator with an odd number of coefficients N, the output is delayed by $\frac{N-1}{2f_s}$, where f_s denotes the sampling frequency. In order to compensate for the phase shift introduced by the delay, an additional phase shift of

$$\phi_d = \frac{N-1}{2f_s}\omega \qquad (3.16)$$

is introduced in eqs. (3.13) and (3.14). This yields the following desired frequency response of non-recursive filters #1 and #2

$$\begin{aligned} \Phi_1(\omega) &= -\phi_f - k\Delta x - kx_1 + 3\pi/2 + \frac{N-1}{2f_s}\omega && (3.17) \\ \Phi_2(\omega) &= -\phi_f - kx_1 + \pi/2 + \frac{N-1}{2f_s}\omega && (3.18) \\ |\mathcal{D}(\omega)| &= \frac{1}{K_f(\omega)} \cdot \frac{1}{2\cos(-k\Delta x + \pi/2)} && (3.19) \end{aligned}$$

Inspection of eq. (3.19) reveals that $|\mathcal{D}(\omega)|$ is the product of two terms.
The first term is the inverse Biésel far field coefficient. This term approaches infinity as f approaches 0 Hz (see fig. 2.2). Thus, absorption of low frequency reflected wave components requires large piston stroke length. In practice, this term must be truncated at low frequencies in order to avoid that the wave paddle displacement signal exceeds the maximum paddle displacement.

The second term is associated with the separation of incident and reflected wave signals. This term approaches infinity at frequencies for which

$$k\Delta x = n \cdot \pi, \qquad n = 0, 1, 2... \tag{3.20}$$

For frequencies in the vicinity of these singularities, noise in the measured surface elevation signals will be amplified, resulting in significant errors in the paddle displacement correction signal $X^*(t)$. Consequently, the gauge distance Δx must be chosen so that the singularities fall outside the range of wave frequencies.
The problem is identical to that described by Goda and Suzuki (1976), and it can be eliminated by replacing the two wave gauges applied here with two colocated gauges, i.e. a wave gauge (or pressure gauge) and a current meter located on the same vertical line in the channel (Hughes, 1993).

3.4 Physical Model Tests

3.4.1 Test Set-up

In order to determine the performance of the active absorption method described above, the method was implemented in the control system of a piston-type wave generator placed in a wave channel at the Hydraulics & Coastal Eng. Laboratory, Aalborg University. The geometry of the wave channel and the wave gauge positions are given in fig. 3.3. A water depth of $d = 0.5$ m was maintained throughout the test series.

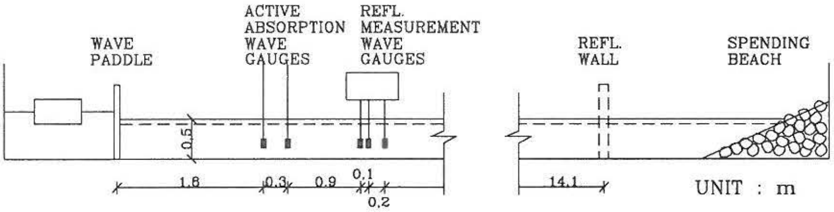

Figure 3.3: Wave channel and wave gauge positions.

The active absorption system was based on surface elevation measurements obtained in wave gauges positioned at distances of $x_1 = 1.80$ m and $x_2 = 2.10$ m from the wave paddle. Thus, both wave gauges were positioned in the far field, i.e. at distances exceeding $3d$ (see sec. 2.2).
The wave spectra reproduced in the wave channel are typically characterised by spectral peak frequencies of 0.5 Hz to 1.0 Hz. With the wave gauge distance of $\Delta x = 0.30$ m, the singularities in the desired gain are well outside this frequency range (see fig. 3.4).
When active absorption was applied, the surface elevation time series were recorded and digitized by means of a PC equipped with an A/D-D/A-card, digital filtering and superposition were performed, and the resulting paddle displacement correction signal was added to the input signal read from the signal generator.
At the far end of the channel, a spending beach was situated. In order to be able to

perform tests with different degrees of reflection from the channel termination, provision was made for mounting a vertical reflecting wall in front of the spending beach.

3.4.2 Filter Design

Non-recursive filters with $N = 123$ coefficients and a sample frequency of $f_s = 40\,\text{Hz}$ were applied. The desired frequency response, $\mathcal{D}(\omega)$, of the filters is given by eqs. (3.17)-(3.19). The desired frequency response of filter #2 is plotted in fig. 3.4.

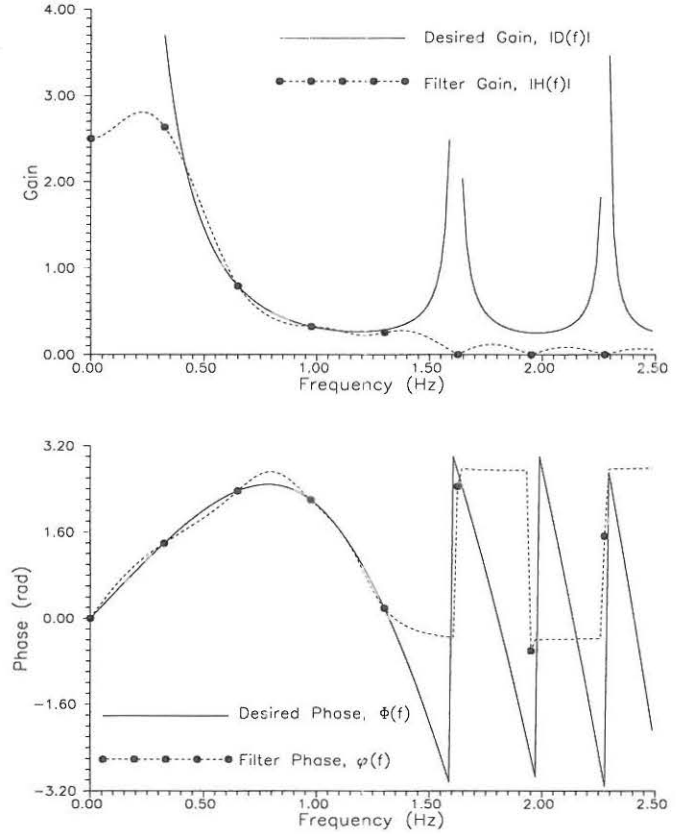

Figure 3.4: Frequency response of filter #2, model test. Dots mark sample frequencies.

The filter design is complicated by the presence of multiple singularities in the desired gain. In the vicinity of these singularities, the desired gain is characterised by quick transitions which cannot be modelled with finite length non-recursive filters (see App. A).

As mentioned above, the energy in the wave spectra generated in the wave channel is normally concentrated in the frequency range 0.5 Hz-1.0 Hz. Consequently, the filter frequency response should be in good agreement with the desired frequency response in this frequency range.

The filters were designed by means of the trial-and-error approach described in App. A. In order to obtain the smooth filter frequency response $\mathcal{H}(f)$ given in fig. 3.4, the frequency response at the sample frequencies was manipulated in the following way:

The singularity in the desired filter gain at $f = 0$ Hz, was removed by prescribing gains of 2.5 and 2.6 at sample frequencies 0 and 1. These manipulations yield a filter gain in poor agreement with the desired gain at low frequencies (0 Hz-0.4 Hz). However, they are necessary in order to avoid oscillations in the filter frequency response due to quick transitions (see App. A). Furthermore, as mentioned in sec. 3.3, the gain should be truncated at low frequencies in order to avoid wave paddle displacement signals exceeding the maximum paddle displacement.

The desired frequency response at higher frequencies is characterised by multiple singularities in the gain, appearing at a growing rate as the frequency increases. Furthermore, the phase shifts at high frequencies are characterised by quick transitions. It was found, that it was impossible to design a non-recursive filter with this frequency response. Therefore, zero gain was prescribed at sample frequencies above 1.5 Hz, introducing a low pass filter effect which effectively removed all singularities (see fig. 3.4).

The final filter frequency response given in fig. 3.4 is in good agreement with the desired frequency response in the frequency area 0.4 Hz-1.3 Hz, and consequently the filter is well-suited for the physical model tests.

Similar manipulations were performed in the design of filter #1.

3.4.3 Test Results

In order to evaluate the efficiency of the absorbing wave generator when applied to irregular wave tests involving test structures with different degrees of reflection, tests covering all four permutations of the alternatives

- Either with or without active absorption applied
- Either with the spending beach or the reflecting wall at the far end of the channel

were performed.

All tests were performed with exactly the same input from the signal generator: a wave paddle displacement signal corresponding to a JONSWAP-spectrum with significant wave height $H_s = 0.04$ m, peak frequency $f_p = 0.6$ Hz and peak enhancement factor $\gamma = 3.3$ sampled at a frequency of $f_s = 40$ Hz and generated by means of digital filtering of Gaussian white noise in the time domain (see sec. 2.3.3).

The wave channel is equipped with three wave gauges mounted on a beam at distances of 3.0 m, 3.1 m and 3.3 m from the wave paddle (see fig. 3.3). In each test the incident and reflected spectra were resolved as described by Mansard and Funke (1980) based on surface elevation time series measured in these gauges. Surface elevation time series of length $T = 1280\,\mathrm{s}$ sampled at a frequency of $f_s = 10\,\mathrm{Hz}$ were applied. In the data analysis, the measured time series were divided into subseries of length $256\Delta t = 25.6\,\mathrm{s}$ which yields 50 spectral estimates and a frequency domain resolution of $\Delta f \approx 0.039\,\mathrm{Hz}$. The incident spectra are given in fig. 3.5.

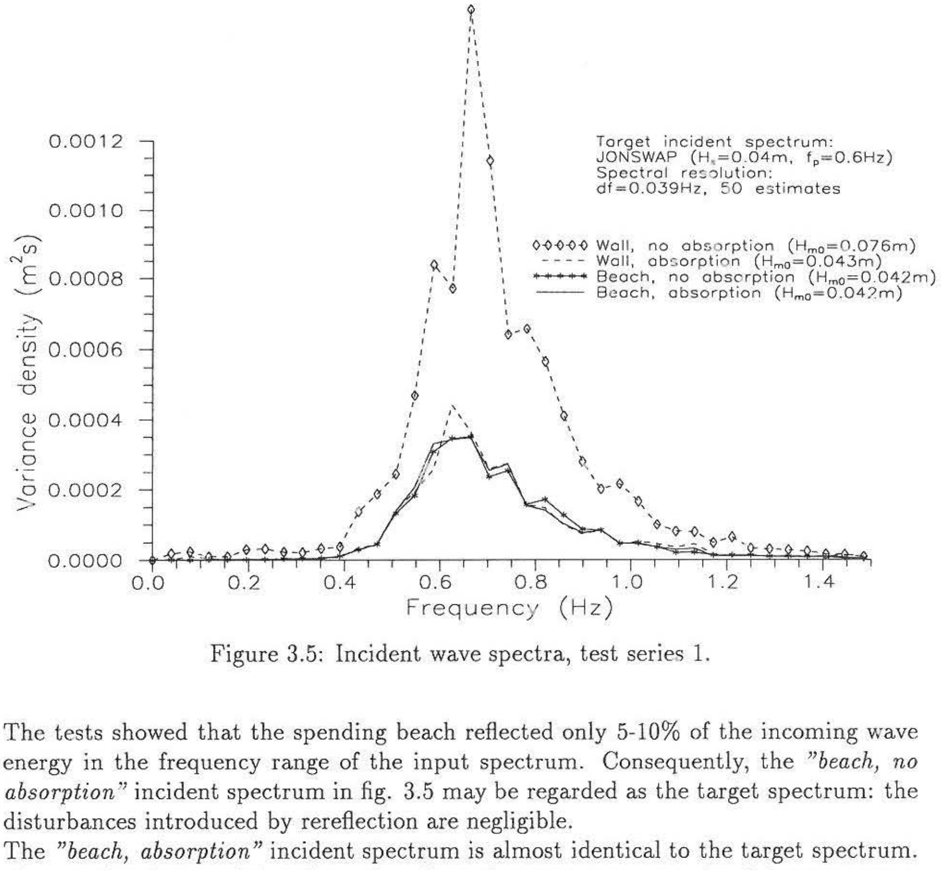

Figure 3.5: Incident wave spectra, test series 1.

The tests showed that the spending beach reflected only 5-10% of the incoming wave energy in the frequency range of the input spectrum. Consequently, the *"beach, no absorption"* incident spectrum in fig. 3.5 may be regarded as the target spectrum: the disturbances introduced by rereflection are negligible.

The *"beach, absorption"* incident spectrum is almost identical to the target spectrum. This implies that applying the active absorption system to tests involving test structures with little reflection will not introduce disturbances in the incident spectrum.

The efficiency of the active absorption system is demonstrated by the test results obtained with the reflecting wall installed at the far end of the channel. When active absorption is applied, the incident spectrum is in excellent agreement with the target spectrum, whereas the incident spectrum obtained without active absorption is significantly distorted by rereflection (see fig. 3.5).

Subsequently, the significant wave height of the target JONSWAP-spectrum was raised to $H_s = 0.08\,\mathrm{m}$, and the four tests were repeated in order to determine the performance of the absorbing wave generator when applied to more severe wave conditions. The measured incident wave spectra corresponding to this test series are given in fig. 3.6.

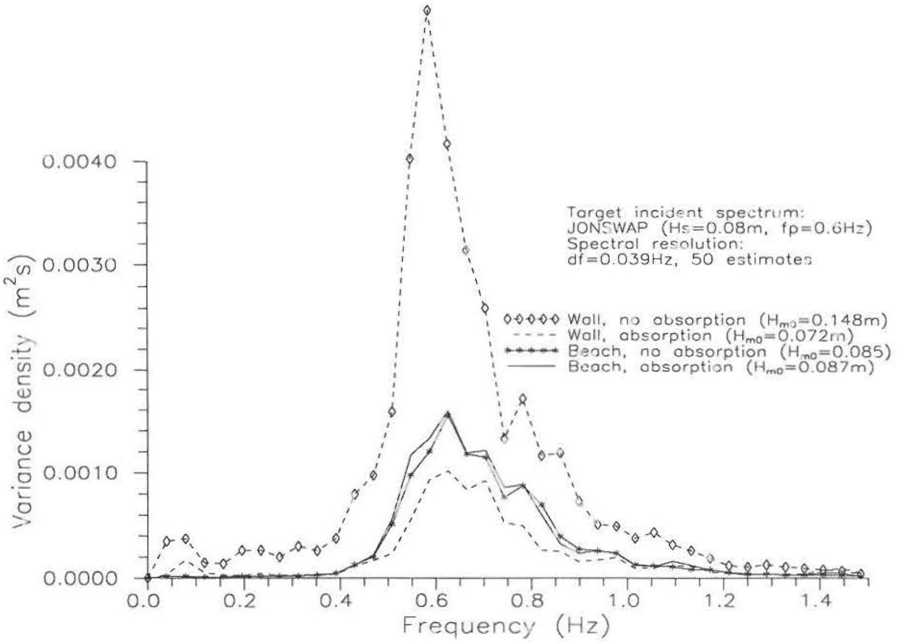

Figure 3.6: Incident wave spectra, test series 2.

Again, the *"beach, absorption"* incident spectrum is almost identical to the target spectrum, indicating excellent performance of the absorbing wave generator at low levels of reflection.
However, with the reflecting wall installed at the channel termination, the incident wave spectrum is distorted despite the application of the absorbing wave generator: the incident wave energy is reduced in the entire frequency range. These discrepancies may indicate poorer performance of the absorbing wave generator due to the increased wave height (the desired frequency responses of the filters applied were derived based on the linear hydrodynamic transfer function presented in sec. 2.2, which is valid for small-amplitude waves only). However, the reduction in incident wave energy may have been caused by wave breaking: when the reflecting wall is installed, a significant reflected wave train is introduced resulting in an increase in the total wave energy, which may cause wave breaking. In fact, wave breaking was observed during both tests with the reflecting wall installed at the far end of the channel, whereas no wave breaking occured in the two tests performed with the spending beach at the channel termination. In any case, comparison of the incident wave spectra obtained with and without the absorbing wave generator indicates that the application of an absorbing wave generator has reduced the problem of rereflection.

In order to visualize the effect of active absorption in the time domain, the following test was performed: the reflecting wall was installed in the far end of the channel, and irregular waves were generated. After 60 seconds, wave generation was terminated, and

active absorption was applied. A surface elevation time series recorded at $x = 3.0\,\mathrm{m}$ is given in fig. 3.7 a.
For comparison, a time series recorded in a similar test in which active absorption was not applied is given in fig. 3.7 b.

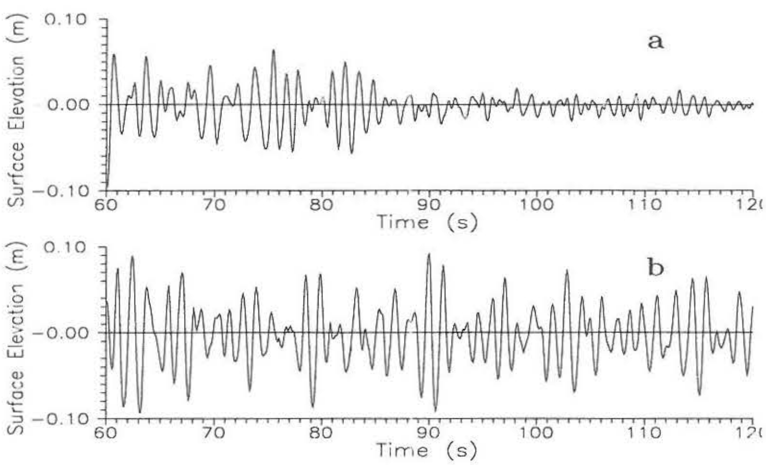

Figure 3.7: Time series obtained with (a) and without absorption (b).

Furthermore, the stability of the system was tested.
Again, the reflecting wall was mounted at the far end of the channel. The active absorption system was applied, and a paddle displacement time series of length $T = 51.2\,\mathrm{s}$ was generated and sent repeatedly to the wave generator.
Two sets of surface elevation time series of length T were recorded starting from $t = T$ and $t = 25\,T$, respectively, and the incident and reflected spectra were resolved. The resulting incident spectra are given in fig. 3.8.

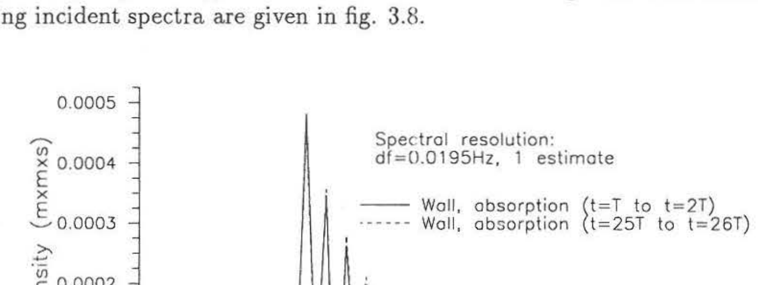

Figure 3.8: Incident wave spectra.

Fig. 3.8 indicates that the system is stable. Apparently, 25 repetitions of the input signal (approx. 20 minutes of wave generation) have not caused significant disturbance in the incident spectrum despite reflection from the wall at the channel termination.

3.5 Conclusion

A method for active absorption of reflected waves in wave channels by means of an absorbing wave generator has been presented.
The motion of the wave generator, which is needed for absorption, is determined by means of linear digital filtering and subsequent superposition of surface elevations measured in two fixed positions in front of the wave generator.
The method has been implemented in the control system of a piston-type wave generator installed in a wave channel, and irregular wave tests involving test structures with different degrees of reflection have been carried out in order to determine the performance of the absorbing wave generator.
The tests performed imply that excellent absorption characteristics have been achieved. The absorbing wave generator is capable of reducing the problem of rereflection considerably even at very high levels of reflection. Furthermore, the active absorption system appears to be stable.
Converting a conventional wave generator to an absorbing wave generator based on the method presented above is relatively inexpensive considering the improvements achieved: the only requirements are two conventional wave gauges and a PC equipped with an A/D-D/A-card. These facilities will normally already be available in most laboratory environments (if a PC equipped with an A/D-D/A-card is used as signal generator for the wave generator, the wave gauges can be connected to this computer, allowing the computer to perform signal generation and correction signal calculation simultaneously).

Compared to the methods for design of absorbing wave makers presented previously, the new method presented above has the advantage that the reflected wave signal is determined based on measurements obtained in the far field, i.e. the disturbances from the near field are avoided (in the methods presented previously, measurements are obtained on the face of the wave paddle, where the local disturbances from the near field may cause a high degree of wave breaking). Furthermore, no prediction of the incident wave train based on the wave generator control signal is needed for separation of the incident and reflected wave trains.
However, the new method has the disadvantage of requiering two wave gauges (the methods presented previously only require a single gauge placed on the face of the paddle) and the problem of the singularities appearing in the desired frequency response, a problem which can be solved by replacing one of the two wave gauges with a current meter.

Chapter 4

3-D Wave Generation

4.1 Introduction

Unidirectional (2-D) waves represent a simplified model of the sea states occurring in nature. Ocean waves are generally multidirectional. Often the three-dimensional structure of ocean waves must be taken into account when physical model tests are performed.

In general, laboratory facilities for directional wave generation are basins of rectangular shape, in which the wave generator takes up one side of the basin and passive wave absorbers are placed along one or all of the remaining three sides. Wave generators for generation of directional seas are comprised by several narrow, individually controlled wave paddles arranged on a straight line. Such segmented wave generators are referred to as *serpent-type* wave generators.
A serpent-type wave generator is capable of generating waves with wave crests oblique to the wave generator front. Reproduction of directional seas is performed by simultaneous generation of wave trains travelling in different directions.

The reproduction of short-crested seas requires a mathematical model describing the three-dimensional structure of the sea surface. In three-dimensional, linear, irregular wave modelling, the surface elevation is assumed to be a stationary, ergodic Gaussian stochastic process produced by superposition of many infinitesimal linear wavelets with different directions of travel, i.e. the surface elevation is given by

$$\begin{aligned} \eta(x,y,t) &= \sum_{i=1}^{I} A_i \sin(\omega_i t - k_i x \cos\theta_i - k_i y \sin\theta_i + \phi_i) \\ &= \sum_{i=1}^{I} A_i \sin(\omega_i t - \overline{k}_i \overline{x} + \phi_i) \qquad (4.1) \end{aligned}$$

where

$$\overline{k}_i = k_i \begin{bmatrix} \cos\theta_i \\ \sin\theta_i \end{bmatrix} \tag{4.2}$$

$$\overline{x} = \begin{bmatrix} x \\ y \end{bmatrix} \tag{4.3}$$

In order to describe the distribution of variance over frequencies and directions in irregular, directional seas, the directional spectrum $S_\eta(\omega,\theta)$ is introduced.
The directional spectrum is often considered a product of the frequency spectrum, $S_\eta(\omega)$, and a directional spreading function, $D(\omega,\theta)$. That is

$$S_\eta(\omega,\theta) = D(\omega,\theta)S_\eta(\omega) \tag{4.4}$$

where θ is the wave propagation angle and $D(\omega,\theta)$ must satisfy

$$\int_{-\pi}^{\pi} D(\omega,\theta)d\theta = 1 \tag{4.5}$$

to assure identical wave energy in $S_\eta(\omega,\theta)$ and $S_\eta(\omega)$.

Several semi-empirical proposals to the formulation of $D(\omega,\theta)$ have been suggested. Mitsuyasu (1975) presented the *Cosine-power* or $\cos^{2s}$ spreading function given by

$$D(\omega,\theta) = \frac{s^{2s-1}}{\pi}\frac{\Gamma^2(s+1)}{\Gamma(2s+1)}\cos^{2s}\left(\frac{\theta-\theta_0}{2}\right) \tag{4.6}$$

where s is a spreading parameter, θ_0 is the mean direction and Γ the Gamma function.

In fig. 4.1, D is plotted as a function of θ for various values of s. The spreading width, σ_θ, defined as the standard deviation of the spreading function D is plotted as a function of the spreading parameter in fig. 4.2.

In the following, the principle in mechanical 3-D wave generation is presented and the transfer function for oblique wave generation is derived. Sources of error in laboratory 3-D wave generation are presented, and methods for synthesis of control signals for serpent type wave generators are described. Finally, the results of a series of laboratory 3-D wave generation tests will be presented and discussed.

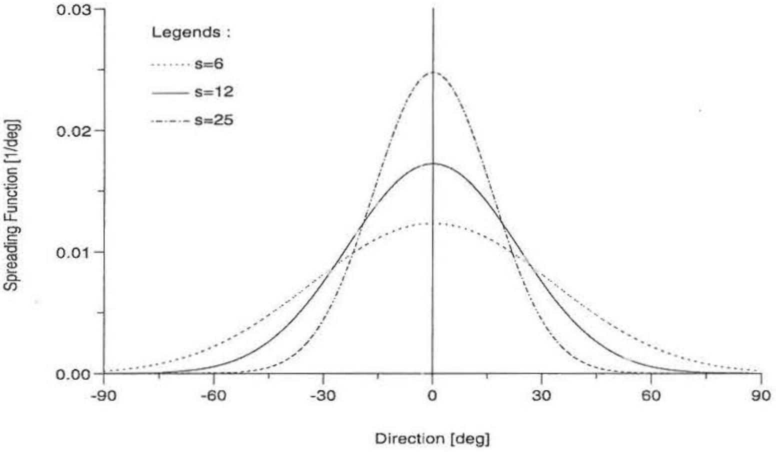

Figure 4.1: Mitsuyasu-type spreading functions.

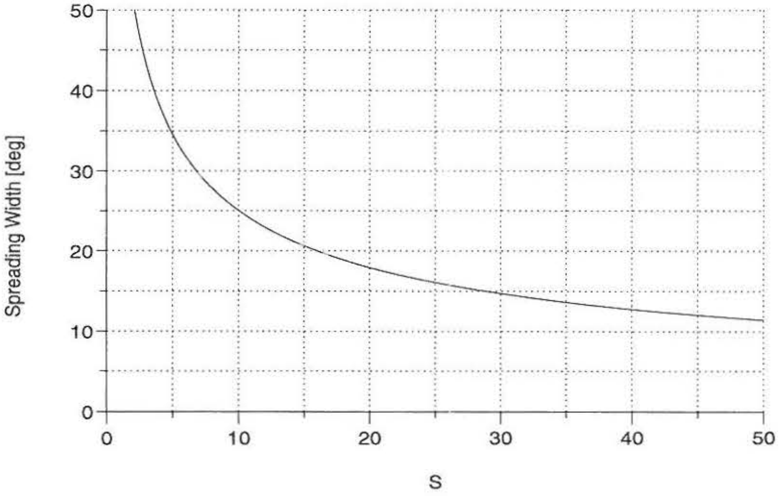

Figure 4.2: Spreading width as a function of s-parameter.

4.2 3-D Hydrodynamic Transfer Function

In sec. 2.2, the hydrodynamic transfer function for uni-directional linear waves was given for a piston-type wave generator. To generate oblique linear waves travelling in a direction different from the x-axis direction perpendicular to the front of the generator, a different transfer function must be applied. In the following, the principle in generation of oblique, regular waves by means of a serpent-type wave generator is presented, and the 3-D hydrodynamic transfer function is derived.

Consider a serpent-type wave generator consisting of a number of infinitely small paddles (fig. 4.3).

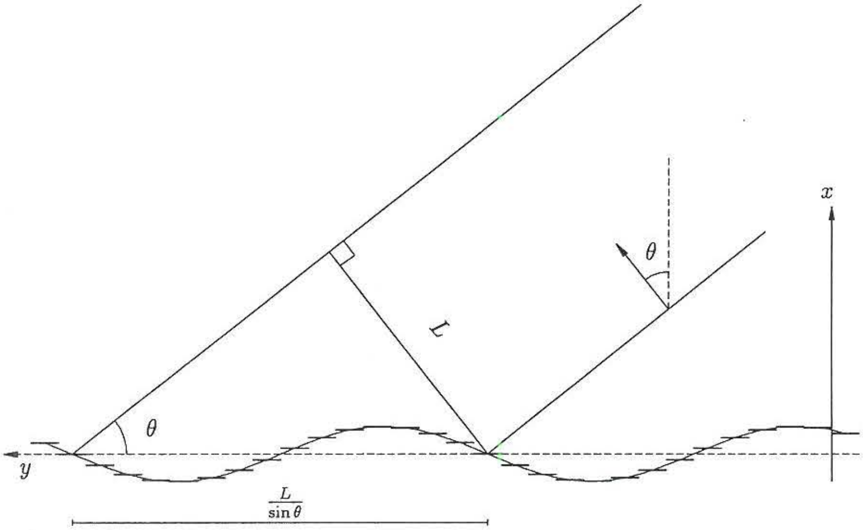

Figure 4.3: Oblique wave generated by serpent-type wave generator.

Each wave paddle moves harmonically in the x-axis direction with the amplitude e. If the wave generator was to produce a long crested regular wave travelling in the x-direction ($\theta = 0\,\text{deg}$) the paddles should move as one solid unit as described in sec. 2.2. In order to produce a regular oblique wave travelling in the θ direction, phase shifts must be introduced between the individual paddles. It is evident that the required phase shifts between individual wave paddles will lead to a sinusoidal shape of the front of the wave generator. If the wave length of the generated wave is L the wave length of the sinusoidal front of the wave generator is $l = L/\sin\theta$ (see fig. 4.3). Thus, for a wave paddle centred in y, the phase shift relative to the origin is

$$\begin{aligned}\phi &= 2\pi\frac{y}{l}\\ &= ky\sin\theta \qquad (4.7)\end{aligned}$$

Furthermore, the magnitude of the 3-D hydrodynamic transfer function differs from the magnitude of the 2-D transfer function derived in sec. 2.2.
Consider part of the wave generator of length Δl, and let the generated regular wave energy travel in the θ direction with the group celerity c_g (see fig. 4.4).

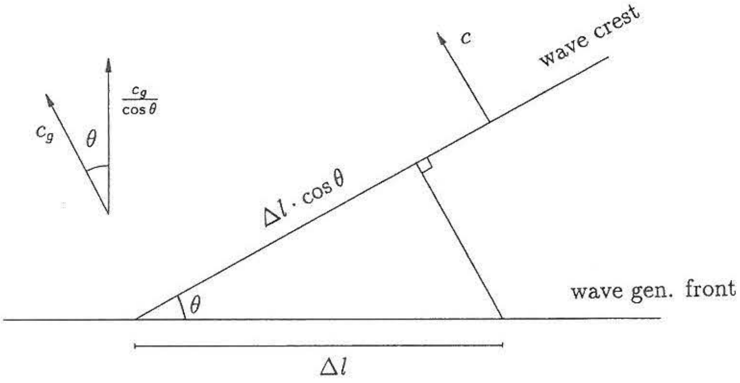

Figure 4.4: Wave generator generating oblique, regular wave.

The energy flux, E_f, over the length l is proportional to the amplitude squared multiplied by the group velocity (Dean and Dalrymple (1984)), i.e.

$$E_f \sim A^2 c_g l \tag{4.8}$$

Consequently, the energy flux in the generated oblique wave over the length $\Delta l \cos\theta$ in fig. 4.4 is

$$E_f \sim A^2 c_g \Delta l \cos\theta \tag{4.9}$$

Assuming that no diffraction occurs (i.e. that the wave generator is infinitely long), this energy flux must be balanced by the energy flux over the length Δl just in front of the wave generator. As the wave amplitude in front of the wave generator corresponding to the progressive term in eq. (2.3) is $eK_f(\omega)$, and the corresponding group velocity is $c_g/\cos\theta$, this energy flux is

$$E_f \sim (eK_f(\omega))^2 \frac{c_g}{\cos\theta} \Delta l \tag{4.10}$$

Combining eqs. (4.9) and (4.10) the amplitude in the generated oblique wave can be written as

$$A = K_f(\omega,\theta)e \quad , K_f(\omega,\theta) = \frac{K_f(\omega)}{\cos\theta} \tag{4.11}$$

Thus, for a wave paddle motion given by

$$X(y,t) = e\sin(\omega t - ky\sin\theta) \tag{4.12}$$

the far field surface elevation is given by

$$\eta(\overline{x},t) = K_f(\omega,\theta)e\sin(\omega t - \overline{k}\overline{x} + \phi_f) \tag{4.13}$$

4.3 Numerical 3-D Wave Synthesis Methods

In general, numerical methods for synthesising surface elevation and wave generator control signals corresponding to directional seas are divided into two categories: Single Summation Models and Double Summation Models, according to the way in which the directional spectrum is decomposed.
In the following, a short introduction to both types of models is given.

4.3.1 Single Summation Models

In Single Summation Models the directional spectrum is decomposed as follows

$$\eta(x,y,t) = \sum_{n=1}^{N} A_n \cos(\omega_n t - k_n x \cos\theta_n - k_n y \sin\theta_n + \phi_n) \tag{4.14}$$

where $\omega_n = n\Delta\omega$
$A_n = \sqrt{2S_\eta(\omega_n)\Delta\omega}$
$\phi_n : 2\pi\mathcal{U}[0,1]$ (DSA-formulation)

Thus, each frequency component is assigned a unique wave propagation angle θ_n.
Several wave synthesis methods based on the Single Summation Method have been suggested.
Sand and Mynett (1987) presented a method in which the propagation angles are selected at random according to the cumulative distribution of $D(\omega,\theta)$.
Miles (1989) suggested rewriting eq. (4.14) in the following form

$$\eta(x,y,t) = \sum_{i=1}^{I}\sum_{j=1}^{J} A_{ij} \cos(\omega_{ij} t - k_{ij} x \cos\theta_{ij} - k_{ij} y \sin\theta_{ij} + \phi_{ij}) \tag{4.15}$$

$$\begin{aligned} \text{where} \quad & \omega_{ij} = (J(i-1)+j)\Delta\omega \\ & A_{ij} = \sqrt{2S_\eta(\omega_{ij})D(\omega_{ij},\theta_{ij})J\Delta\omega\Delta\theta} \\ & I = N/J \\ & \theta_{ij} = (P_i(j)-1)\Delta\theta + \theta_{min} \\ & \Delta\theta = (\theta_{max}-\theta_{min})/(J-1) \\ & \phi_{ij} : 2\pi\mathcal{U}[0,1] \end{aligned}$$

and θ_{max} and θ_{min} denote the maximum and minimum discrete wave direction, respectively. Thus, the directional spreading function is discretized into J equally spaced wave directions ranging from θ_{min} to θ_{max}.
Three different formulations of the integer function $P_i(j)$ were given. $P_i(j)$ could either be chosen as one of the following functions

$$P_i(j) = j \quad , j = 1..J \tag{4.16}$$

$$P_i(2j-1) = j \ \text{ and } \ P_i(2j) = J/2 + j \quad , j = 1..J/2 \tag{4.17}$$

or as a random permutation of the integers from 1 to J.

Evidently, methods based on eq. (4.15) yield a good fit to the target spreading function over each frequency interval $J\Delta\omega$. However, this is achieved at the expense of distortions in the frequency spectrum.
In contrast, the method suggested by Sand and Mynett (1987) yields a correct reproduction of the frequency spectrum.

4.3.2 Double Summation Models

The basic Double Summation Model is given by

$$\eta(x,y,t) = \sum_{i=1}^{I}\sum_{j=1}^{J} A_{ij}\cos(\omega_i t - k_i x\cos\theta_{ij} - k_i y \sin\theta_{ij} + \phi_{ij}) \tag{4.18}$$

$$\omega_i = i\Delta\omega, \quad \theta_{ij} = (j-1)\Delta\theta + \theta_{min}$$

$$\begin{aligned} \text{where} \quad & A_{ij} = \sqrt{2S_\eta(\omega_i,\theta_{ij})\Delta\omega\Delta\theta} \\ & \phi_{ij} : \ 2\pi\mathcal{U}[0,1] \quad \text{(DSA-formulation)} \\ \text{or} \quad & A_{ij} = \sqrt{a_{ij}^2 + b_{ij}^2} \\ & \phi_{ij} = \arctan(b_{ij}/a_{ij}) \\ & a_{ij}, b_{ij} : \mathcal{N}(0, S_\eta(\omega_i,\theta_{ij})\Delta\omega\Delta\theta) \quad \text{(NSA-formulation)} \end{aligned}$$

An important characteristic of the Double Summation Models is that due to phase locking between components with identical frequencies travelling in different directions, the generated wave field is neither ergodic nor spatially homogeneous for finite values of I and J as pointed out by Jefferys (1987). However, when the time domain white noise filtering technique is applied (see sec. 4.4) the problem of phase locking is eliminated. Miles and Funke (1989) presented three methods for frequency domain simulation of waves based on the Double Summation Model.

4.4 3-D Wave Generator Signal Synthesis

As mentioned above, reproduction of directional seas is performed by simultaneous generation of wave trains travelling in different directions. Combining the double summation model described above (eq. (4.18)) with eqs. (4.12) and (4.13), a wave field characterised by the directional wave spectrum $S_\eta(\omega, \theta)$ is generated by prescribing wave generator displacements given by

$$X(y,t) = \sum_{i=1}^{I}\sum_{j=1}^{J} e_{ij}\cos(\omega_i t - k_i y \sin\theta_{ij} + \phi_{ij}) \tag{4.19}$$

$$\omega_i = i\Delta\omega, \quad \theta_{ij} = (j-1)\Delta\theta + \theta_{min}$$

where $e_{ij} = \frac{1}{K_f(\omega_i,\theta_{ij})}\sqrt{2S_\eta(\omega_i,\theta_{ij})\Delta\omega\Delta\theta}$

$\phi_{ij} : 2\pi\mathcal{U}[0,1]$ (DSA-formulation)

or $e_{ij} = \sqrt{a_{ij}^2 + b_{ij}^2}$

$\phi_{ij} = \arctan(b_{ij}/a_{ij})$

$a_{ij}, b_{ij} : \mathcal{N}(0, \frac{1}{K_f(\omega_i,\theta_{ij})^2} S_\eta(\omega_i,\theta_{ij})\Delta\omega\Delta\theta)$ (NSA-formulation)

If waves are simulated in the *frequency domain*, i.e. by white noise filtering in the frequency domain and subsequent use of IFFT, a N point realisation of the wave generator displacement signal in position y is written as the Fourier series

$$X(y, n\Delta t) = \sum_{i=1}^{N/2}\sum_{j=1}^{J} e_{ij}\cos(\omega_i n\Delta t - k_i y\sin\theta_{ij} + \phi_{ij}) \tag{4.20}$$

$$= \sum_{i=1}^{N/2} e_i \cos(\omega_i n\Delta t + \phi_i) \quad , n = 1..N \tag{4.21}$$

where $\omega_i = i\Delta\omega \quad , \Delta\omega = \frac{2\pi}{N\Delta t}$

$e_i = \sqrt{a_i^2 + b_i^2}$

$\phi_i = \arctan(b_i/a_i)$

$a_i = \sum_{j=1}^{J} e_{ij}\cos(-k_i y \sin\theta_{ij} + \phi_{ij})$

$b_i = \sum_{j=1}^{J} e_{ij}\sin(-k_i y \sin\theta_{ij} + \phi_{ij})$

where the amplitudes e_{ij} and phases ϕ_{ij} can be chosen using either the DSA or the NSA method.
Thus, each wave generator displacement signal is obtained by one N point IFFT.

Alternatively, wave generator displacement signals can be simulated in the *time domain* by means of linear filtering of white noise. This can be done by extending the time domain method for numerical unidirectional wave generation presented in sec. 2.3.3 to multidirectional wave conditions. Applying non-recursive linear digital filters (see App. A) a N point realisation of the wave generator displacement signal in position y can be determined as

$$X(y, n\Delta t) = \sum_{j=1}^{J} \sum_{i=1}^{I} h_i^j \alpha_{n-i}^j \quad , n = 1..N \tag{4.22}$$

where the desired gain and phase of the filter operator h^j are given by

$$\begin{aligned} |\mathcal{D}^j(\omega)| &= \sqrt{\frac{\pi}{\Delta t} \frac{1}{K_f(\omega, \theta_j)}} \sqrt{S_\eta(\omega, \theta_j)\Delta\theta} & (4.23) \\ \Phi^j(\omega) &= -ky \sin\theta_j & (4.24) \\ \theta_j &= (j-1)\Delta\theta + \theta_{min} & (4.25) \end{aligned}$$

and α^j represents a sequence of independent standard normal distributed random numbers, i.e.

$$\alpha_n^j : \mathcal{N}(0, 1) \tag{4.26}$$

Thus, the directional wave field is decomposed into J directions each represented by a linear filter operator h^j. The output from each linear filter j represents a wave generator displacement signal corresponding to a unidirectional, irregular wave train travelling in the θ_j direction. Each wave generator displacement signal is obtained by performing $N \cdot J$ I-point discrete convolutions.

Frequency domain simulation appears to be the most commonly used double summation method. However, the following arguments in favour of time domain simulation may be given:

Time domain simulation based on the double summation method described above avoid the problems introduced by discrete wave components, i.e. the generated wave fields are ergodic and spatially homogeneous (Jefferys (1987)).

Frequency domain simulation requires batch processing; prior to generating the desired wave field, the length of the generated signal N must be chosen and the N-point wave generator displacement signal must be determined and stored. In contrast, time domain simulation offers the possibility of generating the wave generator displacement signal on-line, i.e. during the test, with no restriction on the length of the generated signal.

Furthermore, the computational effort involved in frequency domain simulation is of the order of $N \ln(N)$ due to the use of IFFT, and the storage requirement is proportional to N (Solomonidis and Yarimer (1992)). When time domain simulation is applied, the computational effort is linear in N (see eq. (4.22)), and the storage requirement is small and does not depend on N. Consequently, for large N, time domain simulation appears to be preferable.

4.5 Sources of Error

As described in sec. 4.2 the required phase shifts between individual wave paddles in a directional wave maker generating an oblique, regular wave will lead to a sinusoidal shape of the front of the wave generator. If the front of the actual wave generator fails to reproduce this shape correctly, as always will be the case due to the finite width of the individual wave paddles, undesired (spurious) waves will be generated.

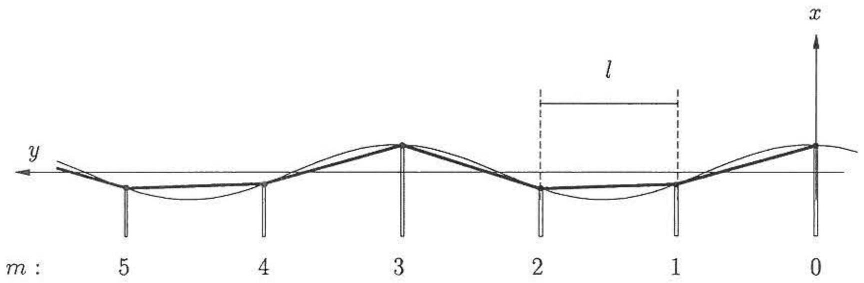

Figure 4.5: Serpent-type wave generator with hinged paddles.

Sand (1979) determined the amplitudes A_p and directions θ_p of waves generated by means of wave generators comprised by finite width wave paddles. For the wave generator given in fig. 4.5, the correct wave generator displacement signal for generating an oblique wave with frequency ω and direction θ given by eq. (4.12) is approximated by

$$\begin{aligned} X(y,t) &= e\sin(\omega t - 2\pi \tfrac{m}{N_l}) + e^{\frac{y-ml}{l}}\left(\sin(\omega t - 2\pi \tfrac{m+1}{N_l}) - \sin(\omega t - 2\pi \tfrac{m}{N_l})\right) \\ & ml < y < (m+1)l \end{aligned} \tag{4.27}$$

where N_l denotes the number of paddles per period in the y-direction, i.e.

$$N_l = \frac{L}{l\sin\theta} \tag{4.28}$$

Eq. (4.27) was represented by a Fourier series, and the regular, oblique wave generated by each term in the Fourier series was determined. For the p'th term, the amplitude and direction of the generated wave was determined as

$$A_p = K_f(\omega,\theta_p)e \quad , K_f(\omega,\theta_p) = \frac{K_f(\omega)}{\cos\theta_p}\left(\frac{\sin(\pi/N_l)}{\pi(p-1/N_l)}\right)^2 \tag{4.29}$$

$$\sin\theta_p = \frac{L(1-pN_l)}{N_l l} \tag{4.30}$$

where p is in the interval

$$\frac{1}{N_l} - \frac{l}{L} < p < \frac{1}{N_l} + \frac{l}{L} \tag{4.31}$$

The main wave propagating in the θ-direction corresponds to $p = 0$ whereas $p \neq 0$ represents spurious wave components.
Comparison of eqs. (4.29) and (4.11) shows that for a wave generator with finite width wave paddles, the hydrodynamic transfer function is reduced by a factor of $\left(\frac{\sin(\pi/N_l)}{\pi/N_l}\right)^2$.
A measure of the influence of spurious waves may be obtained by determining the ratio of the amplitude of the largest spurious wave, $p = P$, and the generated main wave

$$\frac{A_P}{A_0} = \frac{\cos\theta}{\cos\theta_P}\frac{1}{(PN_l-1)^2} \tag{4.32}$$

The ratio given by eq. (4.32) differs from that presented by Sand (1979) who applied a 3-D hydrodynamic transfer function independent of the wave direction when determining the ratio $\frac{A_1}{A_0}$.
In fig. 4.9, the ratio given by eq. (4.32) is given as a function of wave frequency and direction for a specific example.

The physical boundaries of the wave basin will inevitably introduce other undesirable effects which reduce the quality of the generated wave field. Furthermore, the control system of the wave generator represents a possible source of error. Sand and Mynett (1987) listed the following sources of error in 3-D wave generation

- *Diffraction.* The hydrodynamic transfer function presented in sec. 4.2 was derived under the assumption that no energy is transported along the crest of the generated wave. For a finite width wave generator, this assumption is not valid: diffraction of generated oblique waves will cause a reduction in wave amplitude.

- *Reflection.* Waves reflected from the boundaries of the wave basin will cause disturbances in the generated wave field. The problem of reflection can be reduced by means of passive wave absorbers placed along the far end and side walls of the wave basin.

- *Local disturbances.* As described in sec. 2.2 local disturbances will occur in the near field close to the wave board. However, at distances of $3d$ from the wave generator the effect of these disturbances will be negligible.

- *Servocontrol system.* If the amplification of the servo loop in the wave generator control system is too low, the servocontrol system will introduce phase shifts and reduced amplitudes relative to the desired wave generator control signal.

4.6 Boundaries of Test Area

Reproduction of directional seas is performed by simultaneous generation of wave trains travelling in different directions. In multidirectional wave generation, the *test area* is defined as the area in which all generated wave components will be represented. When a wave field corresponding to a given target directional wave spectrum is generated, the test area is limited by the maximum and minimum directions of propagation (θ_{min} and θ_{max}) in the decomposed target directional spectrum. This limitation is illustrated in fig. 4.6. The dashed lines indicate the limits of the generated wave components travelling in the θ_{min} and θ_{max} directions. As the generated wave components propagate away from the wave maker front, wave energy will diffract into the areas beyond the dashed lines, and the amplitudes of the wave components propagating within the test area will be reduced. Thus, the quality of the generated wave field will decrease towards the borders of the test area.

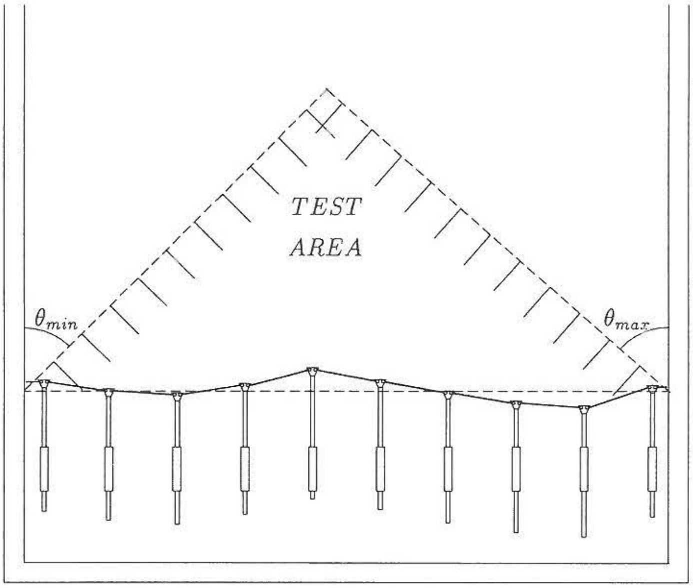

Figure 4.6: Limitations in the available test area.

4.7 Physical Model Tests

This section describes a series of tests in which wave generator control signals generated by means of the time domain white noise filtering method described above are applied to a directional wave generator in order to produce irregular, directional wave fields in a laboratory wave basin.

4.7.1 Test Set-up

The tests were performed in the 3-D wave basin at the Hydraulics & Coastal Engineering Laboratory, Aalborg University. The design of the test facility was described by Burcharth et al. (1986). In fig. 4.8, the dimensions of the basin are given.

The serpent-type wave generator consists of nine paddles hinged with vertical axes to ten hydraulic pistons (see fig. 4.8). Each paddle has a width of 0.9 m and a height of 1.0 m. A short description of the wave generator control system is given in App. B. In order to determine whether the wave generator servocontroller would represent a significant source of error in the wave generation tests (see sec. 4.5), a series of tests were performed in order to determine the wave generator servocontroller frequency response (see App. B). The measured frequency response is given in fig. 4.7.

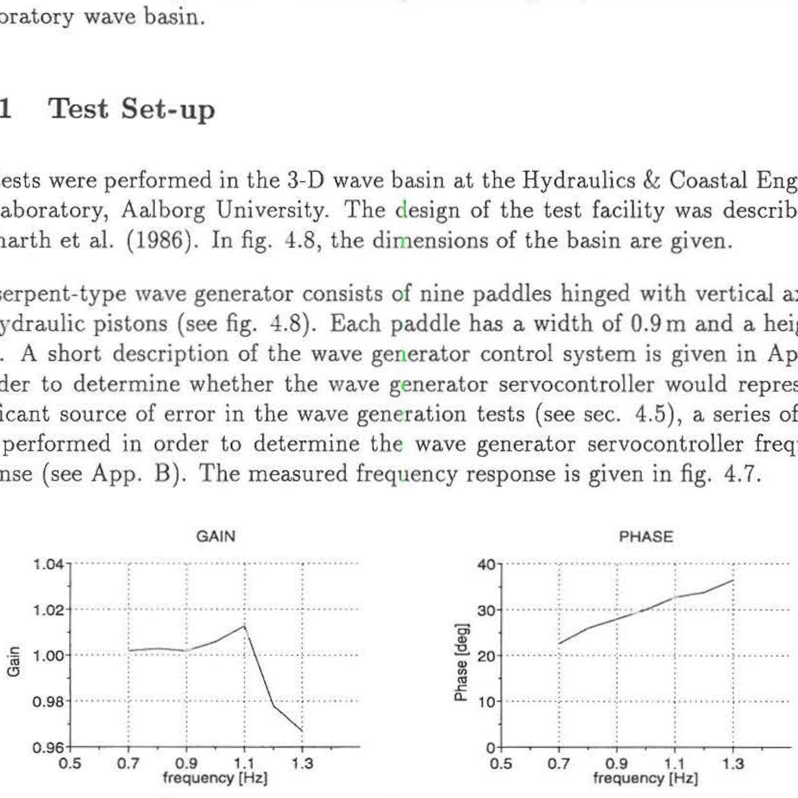

Figure 4.7: Frequency response of servocontrol system (see App. B).

At the far end of the basin, a passive wave absorber designed as a spending beach of perforated, corrugated glass fibre panels is installed. In order to reduce reflection from the basin sides, so-called upright passive wave absorbers made of vertical, perforated steel plates have been placed along both side walls.

All tests were performed with a water depth of $d = 0.35\,\mathrm{m}$. The performance of the passive wave absorber at the basin end is poor at low water depths. Consequently, a gravel spending beach with slope 1:6 was placed in front of the passive wave absorber.

In fig. 4.8, the test set-up is given.

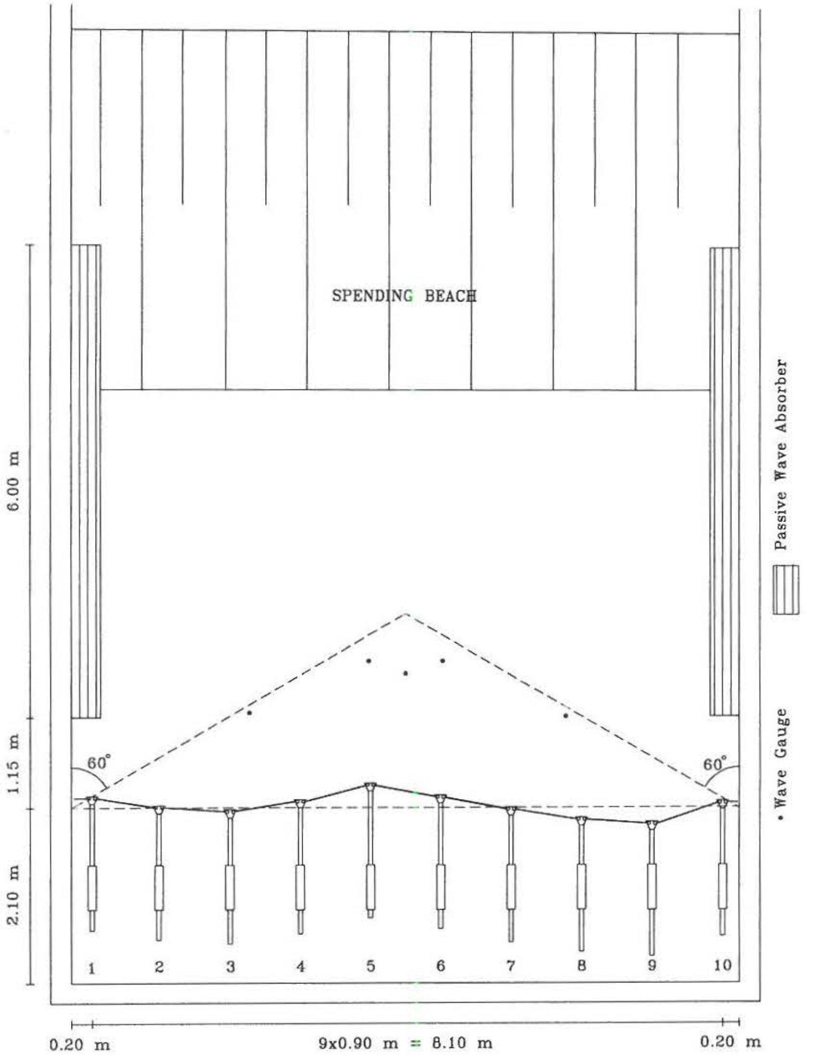

Figure 4.8: Test set-up, Hydraulics & Coastal Eng. Laboratory 3-D wave basin.

In order to predict the magnitude of the disturbances caused by spurious waves generated during the experiments, the term A_P/A_0 (the ratio of the largest spurious wave amplitude and the generated main wave amplitude) and θ_P (the direction of the largest spurious wave), see sec. 4.5, was determined as a function of wave frequency and generated main wave direction. The results are given in figs. 4.9 and 4.10, respectively. In all tests performed, the energy of the target directional spectrum is concentrated at frequencies from 0.6 Hz to 1.3 Hz, and directions of propagation of less than 60 deg. For frequencies of less than 0.9 Hz no spurious waves will appear for directions of less than 60 deg. For frequencies above 0.9 Hz, however, spurious waves will be a source of error.

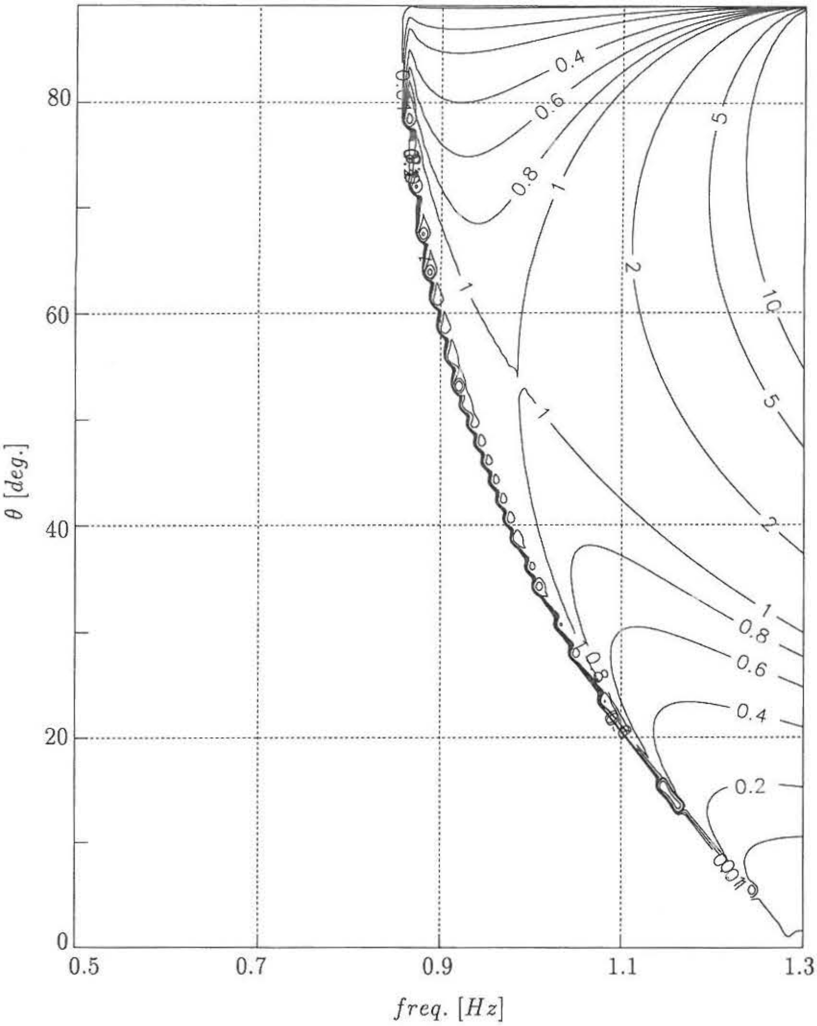

Figure 4.9: Max. spurious wave amplitude to main wave amplitude ratio.

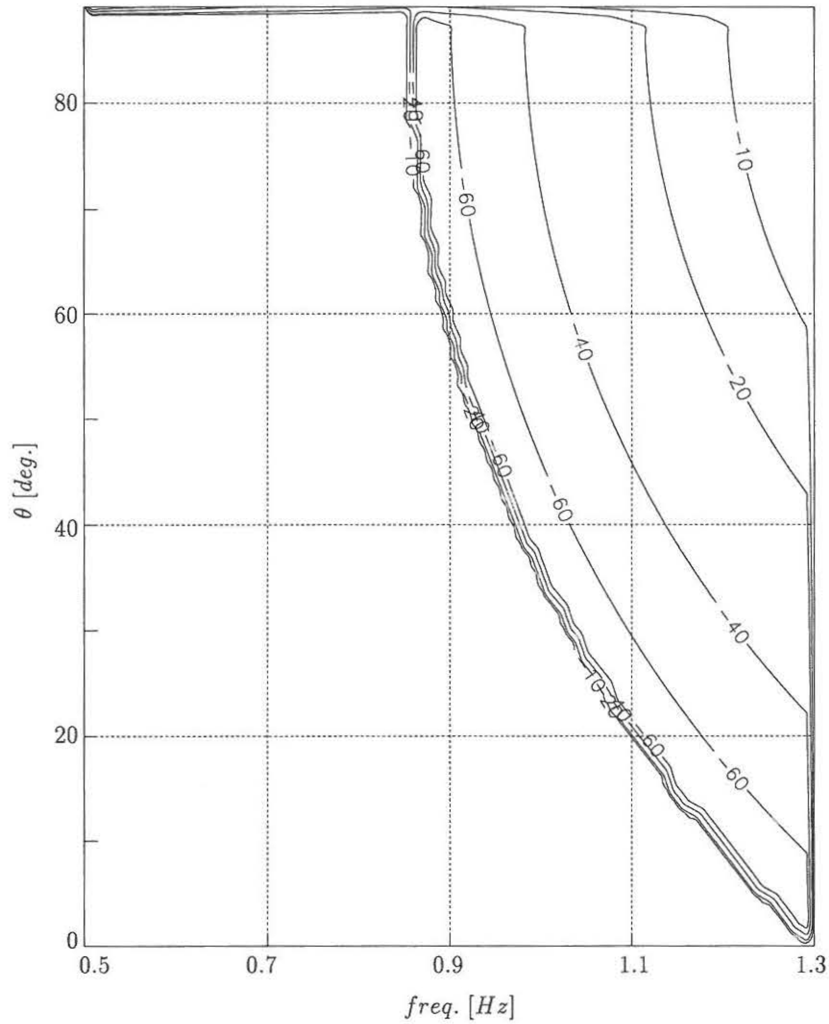

Figure 4.10: Direction of max. amplitude spurious wave.

Test no.	f_p	H_s	θ_0	s
	Hz	m	deg	
1	0.8	0.05	0	6
2	0.8	0.05	0	12
3	0.8	0.05	0	25
4	0.8	0.05	15	12
5	0.8	0.05	15	25

Figure 4.11: Test program, 3-D wave generation tests.

In the wave generation tests performed, the target frequency spectrum was a Pierson-Moskowitz type frequency spectrum with significant wave height $H_s = 0.05$ m and peak frequency $f_p = 0.8$ Hz. Tests involving five different Mitsuyasu type target directional spreading functions were performed.
The test program is shown in fig. 4.11.

4.7.2 Filter Design

As mentioned above, the wave generator displacement signals applied to the directional wave generator were generated by means of the time domain white noise filtering method described in sec. 4.4. The problem in applying this method is to design filter operators characterised by the desired frequency response given by eqs. (4.23) and (4.24).

The filter operators were designed by means of the method described in App. A. In all tests performed, a sample frequency of $f_s = 30$ Hz was chosen for the filters, and the directional spectrum was discretised into $J = 21$ directions. The remaining design parameter is the filter length I. In order to reduce the computational time required in generating the wave generator displacement signals, the filter length should be as small as possible. Thus, the design process is reduced to the problem of determining the minimum filter length I required to obtain a filter operator characterised by a frequency response $\mathcal{H}(\omega)$, which represents an acceptable approximation to the desired frequency response $\mathcal{D}(\omega)$.

In the following, the design of a specific filter operator is described. The example involves a filter operator applied in test 2, in which a directional resolution of $\Delta\theta = 5.314$ deg was used ($\theta_{max} = -\theta_{min} = 53.14$ deg).
The filter operator was designed for wave generator 1, positioned at $y = 4.5 \cdot 0.9$ m (see fig. 4.8). The filter operator corresponds to $j = 1$ ($\theta_1 =$ -53.14 deg).

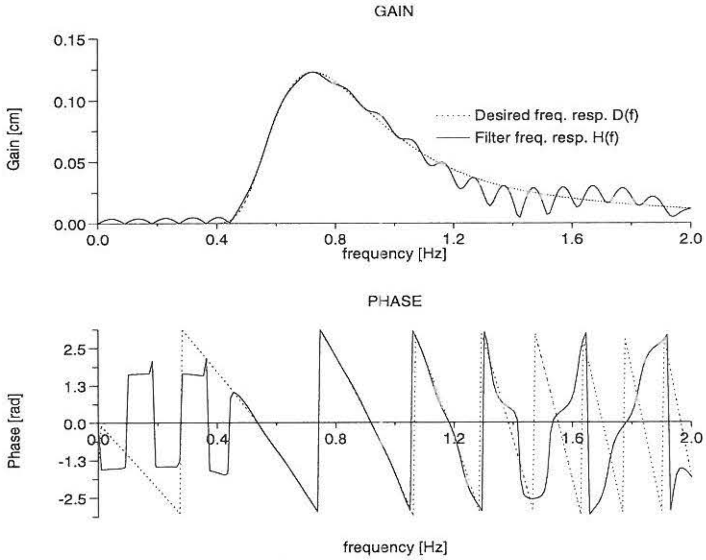

Figure 4.12: Frequency response of filter, $I = 331$.

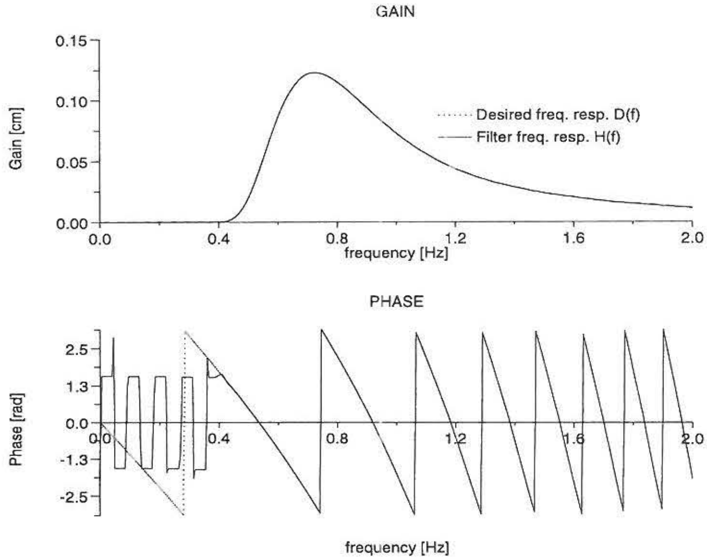

Figure 4.13: Frequency response of filter, $I = 665$.

Fig. 4.12 shows the frequency response of the filter operator with a length of $I = 331$. The desired frequency response is plotted for comparison. The frequency response of the filter operator is in poor agreement with the desired frequency response, particularly at high frequencies, where the the desired phase response is characterised by quick transitions. Consequently, the filter operator length must be increased.
If the filter operator length is doubled, the filter frequency response represents an excellent approximation to the desired frequency response (see fig. 4.13). Consequently, a filter length of $I = 665$ was chosen.

4.7.3 Test Results

In order to enable estimation of the directional spectrum of the generated wave fields, a wave gauge array was installed in the basin. The geometry of the wave gauge array had to be chosen in such a way that the array would fit into the test area defined by maximum and minimum directions of propagation $\theta_{max} = -\theta_{min} = 60\,\mathrm{deg}$ (see fig. 4.8). Furthermore, all gauges had to be placed at distances of more than $3d = 1.05\,\mathrm{m}$ from the wave generator front in order to avoid the effect of local disturbances (see sec. 4.5). Based on these requirements, a wave gauge array identical to array 2 described in Encl. 1 was chosen and installed in the basin (see fig. 4.8).
In each test, surface elevation time series of length $T = 2048\,\mathrm{s}$ were sampled with a sample frequency of $f_s = 6\,\mathrm{Hz}$. In the data analysis, the measured time series were divided into subseries of length $512\Delta t \approx 85.3\,\mathrm{s}$ which yields 24 spectral estimates and a frequency domain resolution of $\Delta f \approx 0.0117\,\mathrm{Hz}$.

In each of the five tests, the directional spreading function $D(f, \theta)$ corresponding to the peak frequency was estimated based on the measured surface elevation time series by means of two different methods for directional spectrum estimation. The methods applied were

- The maximum likelihood method based on standard directional spreading functions (Isobe (1990)).
- The Bayesian Directional Spectrum Estimation Method (Hashimoto et al. (1987)).

The maximum likelihood method based on standard directional spreading functions (MLM) estimates the directional spectrum of the wave field under the assumption that the directional spreading function is given in a specified mathematical form. Here, the Mitsuyasu type spreading function is applied, i.e. a mean direction θ_0 and a spreading parameter s are estimated. In Encl. 1, a description of the MLM method is given. In order to determine the performance of the MLM method, the method was applied to numerically generated surface elevation time series corresponding to each of the five target directional spectra listed in fig. 4.11. The results of these numerical tests are given in Encl. 1.

In contrast to the maximum likelihood method applied here, the Bayesian Directional Spectrum Estimation Method (BDM) is not based on the assumption that the spreading function has a certain mathematical form. In this method, the only assumptions made are that the spreading function is smooth and that it only takes on values larger than zero. Consequently, this method should be capable of identifying spreading functions of arbitrary shape (e.g. asymmetrical and multi-mode spreading functions). The BDM method is applied in order to determine whether the unimodal Mitsuyasu type standard directional spreading function applied in the maximum likelihood method can be expected to provide a good estimate of the spreading function of the generated wave field.

In figs. 4.14-4.18 the spreading functions corresponding to the peak frequency estimated with the MLM method and the BDM method are given for each of the five physical model tests performed.
For comparison, the target spreading functions are plotted.

The MLM and BDM estimates are generally in good agreement. No additional modes have been identified by the BDM method (if present, reflected waves would appear at directions close to 180 deg, transversal waves at ±90 deg), and the spreading functions estimated using the BDM method are symmetrical.
In general, the estimated spreading functions are in excellent agreement with the target spreading functions, even with relatively large spreading widths and with oblique mean directions. However, in test 4 (see fig. 4.17), the spreading function estimated by means of BDM differs somewhat from the target spreading function.

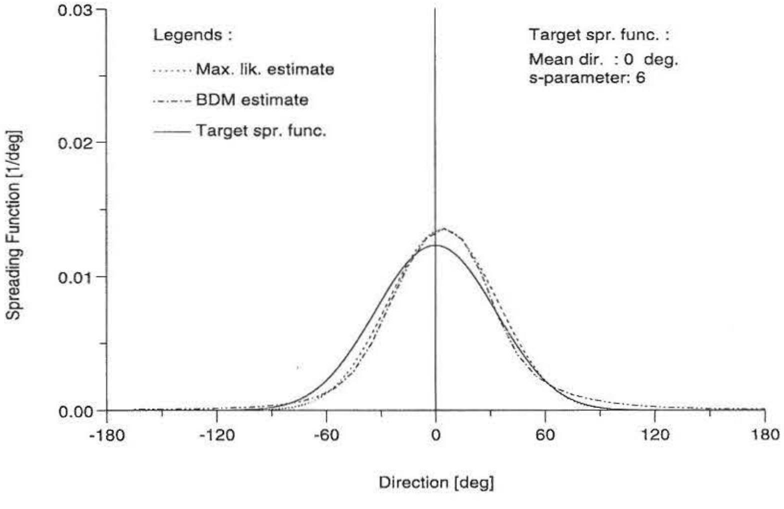

Figure 4.14: Estimated and Target spreading functions, f =0.797 Hz, test 1.

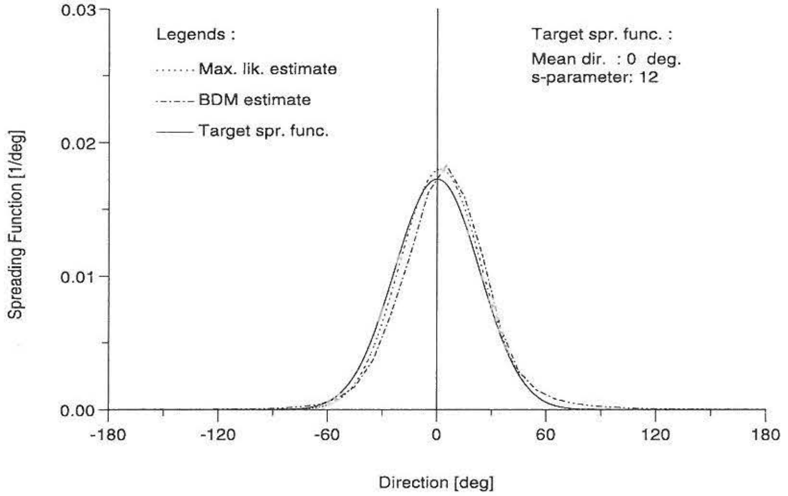

Figure 4.15: Estimated and Target spreading functions, $f = 0.797\,\mathrm{Hz}$, test 2.

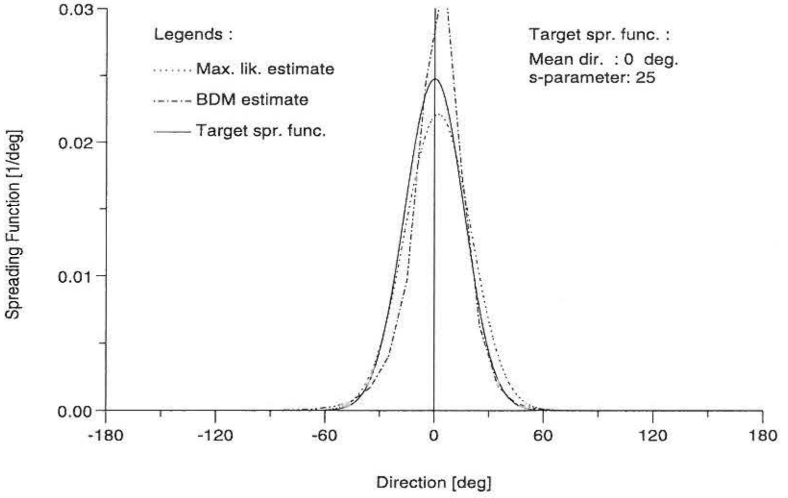

Figure 4.16: Estimated and Target spreading functions, $f = 0.797\,\mathrm{Hz}$, test 3.

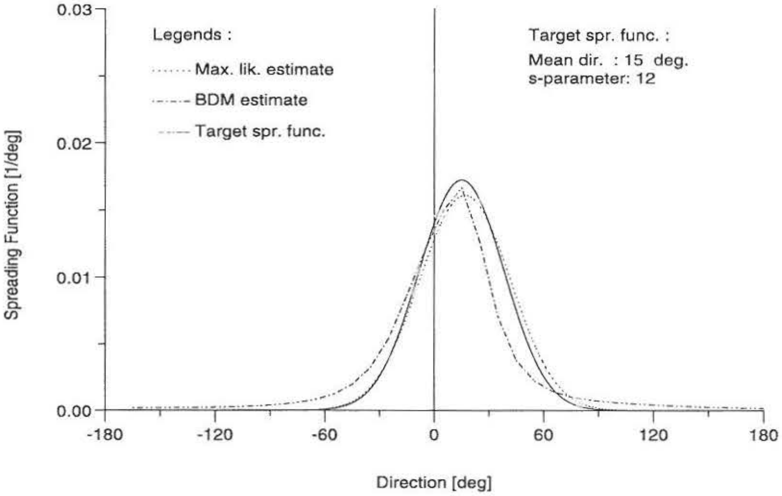

Figure 4.17: Estimated and Target spreading functions, $f = 0.797\,\mathrm{Hz}$, test 4.

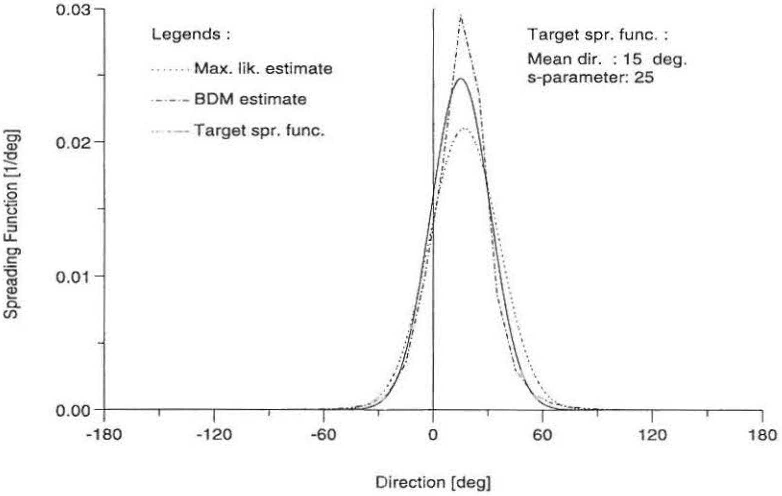

Figure 4.18: Estimated and Target spreading functions, $f = 0.797\,\mathrm{Hz}$, test 5.

Subsequently, the spectral density, mean direction and spreading width was estimated in the entire frequency range of the target directional spectrum for each of the five physical model tests using the MLM method. The results are given in figs. 4.19-4.23.

In general, the parameters estimated based on the measured surface elevation time series are in good agreement with the target values. However, discrepancies do occur.

At low frequencies ($f < 0.7\,\mathrm{Hz}$) the estimated spreading width is generally higher than the target value. However, comparison with the numerical test results (fig. 7-11, Encl. 1) shows that similar discrepancies appear when the MLM method is applied to numerically generated wave data. Therefore, these discrepancies are not necessarily due to sources of error present in the physical model.

In test 1 ($s = 6$, $\theta_0 = 0\,\mathrm{deg}$, fig. 4.19), the estimated spectral density is generally lower than the target value at high frequencies. Furthermore, the estimated spreading width is considerably lower than the target value at high frequencies. Comparing the estimates in fig. 4.19 to the estimates obtained from the corresponding numerical test (Encl. 1, fig. 7) shows that these discrepancies only occur in the estimates obtained from the physical model test. Consequently, the discrepancies must be due to sources of error present in the physical model.
Comparing the estimates for test 1 to the estimates for test 2 ($s = 12$, $\theta_0 = 0\,\mathrm{deg}$, fig. 4.20) and test 3 ($s = 25$, $\theta_0 = 0\,\mathrm{deg}$, fig. 4.21) shows that the reduction of spectral density and spreading width with increasing frequency is particularly pronounced for target spectra with large spreading widths.

These discrepancies could be due to *diffraction*. More energy is lost through diffraction at high frequencies than at low frequencies: generated high frequency wave components would loose relatively more energy through diffraction while travelling towards the wave gauge array than low frequency components travelling in the same direction. Furthermore, the amount of energy lost through diffraction will increase as the angle of propagation increases. This would explain the fact that the estimated spreading width tends to become smaller than the target value as the frequency increases, particularly for target spectra with large spreading widths.

The presence of *spurious waves* could provide another explanation to the discrepancies observed at high frequencies. As described above, figs. 4.9 and 4.10 show that for frequencies above 0.9 Hz, spurious waves will appear. In fact, the discrepancies do start to appear for frequencies above 0.9-1.0 Hz. The amount of energy lost to generation of spurious wave components will increase with increasing frequency and angle of propagation, causing a decreasing main wave amplitude and increasing spurious wave amplitude.

As described in sec. 4.5, the *servocontrol system* of the wave generator may introduce reductions in amplitude relative to the prescribed wave generator displacement signals, thus reducing the spectral density. However, inspection of fig. 4.7 shows that the frequency response of the wave generator servocontroller is characterised by a gain of $|\mathcal{W}(\omega)| = 1.01\text{-}0.97$ (i.e. approximately unity gain) in the frequency range $f = 0.7\text{-}1.3\,\text{Hz}$. Consequently, the reduction in spectral density caused by the wave generator servocontrol system will be negligible.

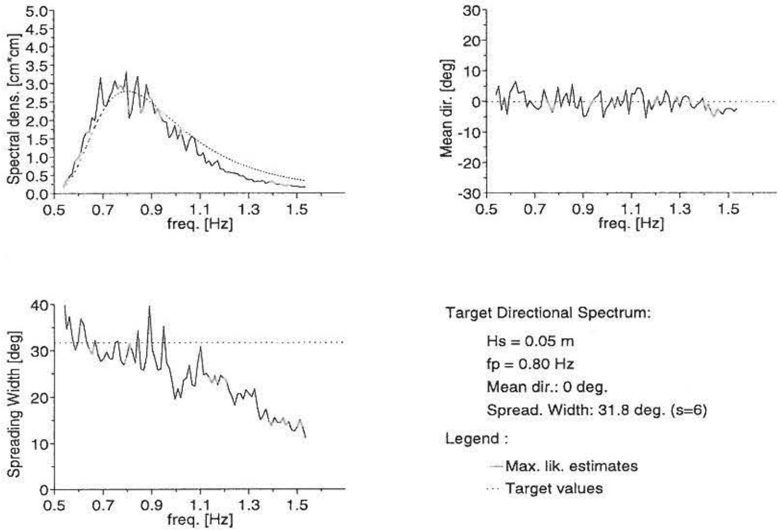

Figure 4.19: Estimated and Target directional spectrum parameters, test 1.

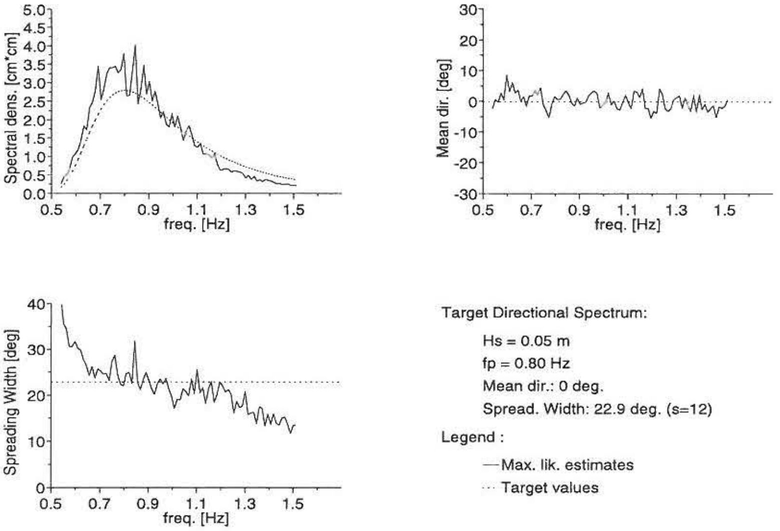

Figure 4.20: Estimated and Target directional spectrum parameters, test 2.

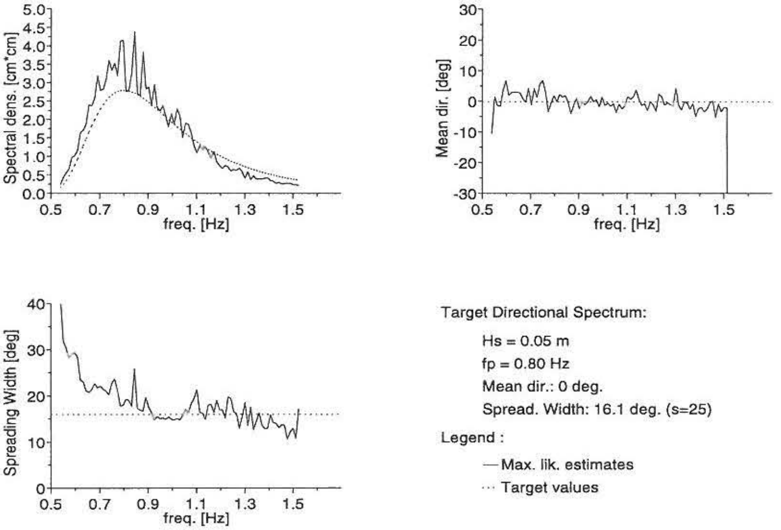

Figure 4.21: Estimated and Target directional spectrum parameters, test 3.

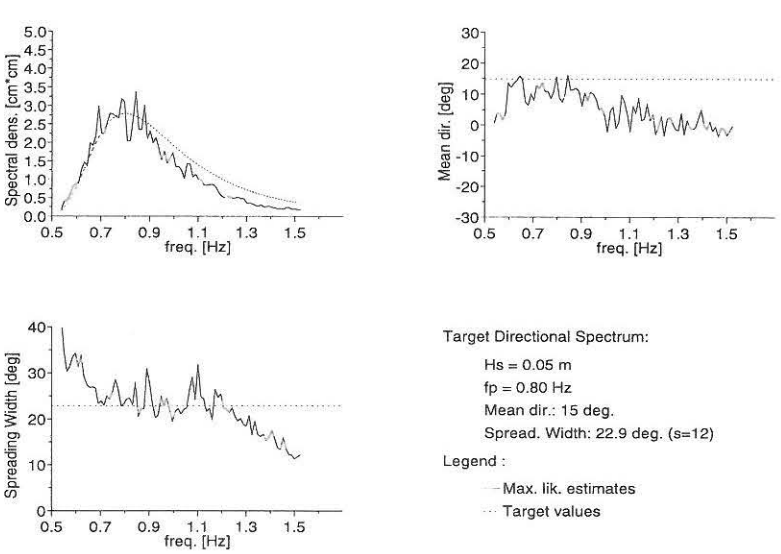

Target Directional Spectrum:
Hs = 0.05 m
fp = 0.80 Hz
Mean dir.: 15 deg.
Spread. Width: 22.9 deg. (s=12)

Figure 4.22: Estimated and Target directional spectrum parameters, test 4.

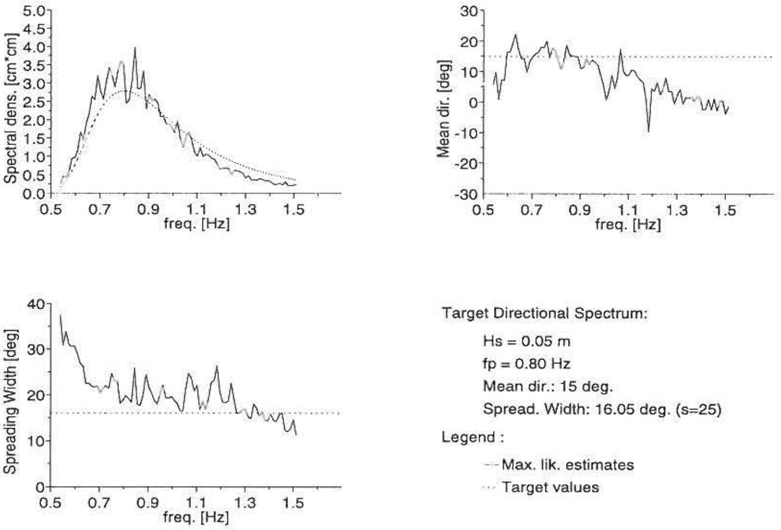

Target Directional Spectrum:
Hs = 0.05 m
fp = 0.80 Hz
Mean dir.: 15 deg.
Spread. Width: 16.05 deg. (s=25)

Figure 4.23: Estimated and Target directional spectrum parameters, test 5.

4.8 Conclusion

The principle in mechanical laboratory 3-D wave generation has been presented, and the 3-D hydrodynamic transfer function has been derived. Sources of error in 3-D wave generation have been described.

A description of the Single Summation Model and Double Summation Model for numerical synthesis of wave signals and wave generator displacement signals corresponding to specified target directional wave spectra has been given.
Time and frequency domain methods for simulation of wave generator displacement signals have been presented.

A series of laboratory 3-D wave generation tests have been performed. The test series involved reproduction of 5 different multidirectional wave fields. Wave generator displacement signals were generated by means of white noise filtering in the time domain. In contrast to white noise filtering in the frequency domain, which appears to be the most commonly used method, white noise filtering in the time domain offers the possibility of generating the wave generator displacement signals on-line with no restriction on the lengths of the signals and with relatively small storage requirements and computational efforts.
For each test the directional spectrum was estimated based on surface elevation time series measured in 5 positions in the wave basin. The MLM and BDM methods for directional spectrum estimation were applied.
The measured directional wave spectra are generally in good agreement with the corresponding target directional wave spectra. However, discrepancies do occur. These discrepancies appear to have been caused by diffraction and the presence of spurious waves.
Based on the results obtained in the laboratory tests it is concluded that wave fields corresponding to the 5 target directional wave spectra can be successfully reproduced in the laboratory wave basin when the wave generator displacement signals are generated by means of the time domain white noise filtering method.

Chapter 5

3-D Active Wave Absorption

5.1 Introduction

As described in sec. 3.1, the presence of rereflected waves is a significant source of error in laboratory tests involving reflective test structures. The problem of rereflection can be solved by application of absorbing wave generators, i.e. wave generators capable of simultaneously generating the desired incident wave field and absorbing the reflected wave field.

Several authors have presented absorbing wave generators for wave channels, i.e. wave generators capable of absorbing unidirectional reflected waves (see chap. 3). When laboratory tests involving multidirectional waves are performed, the problem of rereflection is complicated by the directional spreading present in the wave field. In this case, absorbing directional wave generators, i.e. serpent-type wave generators capable of simultaneously generating the desired multidirectional incident wave field and absorbing the multidirectional reflected wave field, are required.

Hirakuchi et al. (1992) described an absorbing directional wave generator for laboratory wave basins. The displacement signal for each individual wave paddle corresponding to absorption of the reflected wave field was determined based on a method for active absorption of unidirectional waves (Hirakuchi et al. (1990)). Consequently, the effect of wave obliqueness was neglected.

In the following, an absorbing directional wave generator based on a new method for active absorption of reflected waves in multidirectional seas will be presented. The method is based on the correct frequency and direction dependent 3-D hydrodynamic transfer function derived in chap. 4, i.e. the effect of wave obliqueness is taken into account. The performance of an absorbing directional wave generator based on the new method will be determined by means of physical model tests.

5.2 Principle

The principle applied in the absorbing directional wave generator represents an extension of the principle on which the absorbing unidirectional wave generator presented in chap. 3 was based: the displacement correction signal for each individual wave paddle needed for absorption of the reflected wave field is estimated in real time by means of linear filtering and subsequent superposition of surface elevations measured in P positions in the wave field in front of the directional wave generator. When active absorption is applied, the paddle displacement correction signal for each individual wave paddle, $X^*(\overline{x}_m, t)$, is added to the input paddle displacement signal read from the signal generator, $X(\overline{x}_m, t)$, causing the directional wave generator to operate in a combined generation/absorption mode.

The principle is illustrated in fig. 5.1 for an absorbing directional wave generator in which $P = 3$ filtered surface elevation signals are superposed in order to obtain the displacement correction signal for each individual paddle. Two paddles are shown.

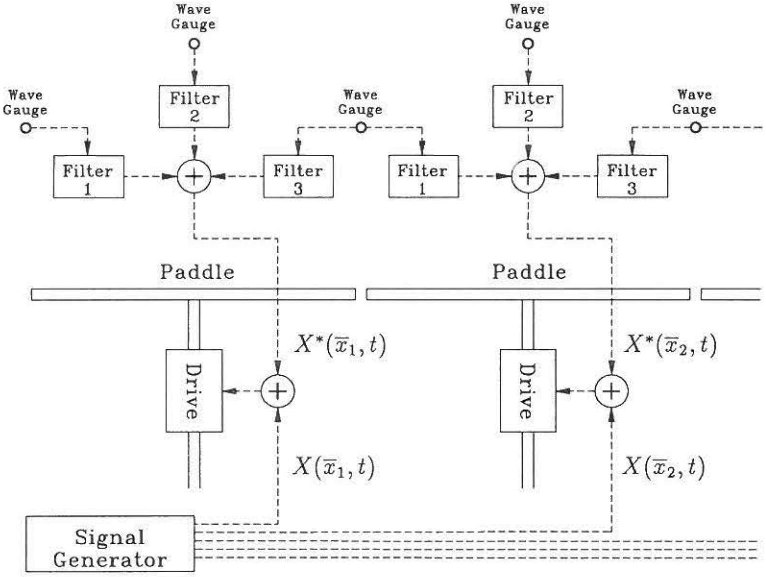

Figure 5.1: Principle of absorbing wave generator.

With a given geometry of the wave gauge array placed in front of the wave generator, the remaining problem in the process of designing the absorbing directional wave generator is to determine the filter characteristics of filters p, $p = 1..P$, which yield the best estimate of the individual paddle displacement correction signals corresponding to absorption of the reflected wave field. In the following, these filter characteristics will be determined.

5.3 Theory

Fig. 5.2 illustrates a directional wave generator in a laboratory wave basin.

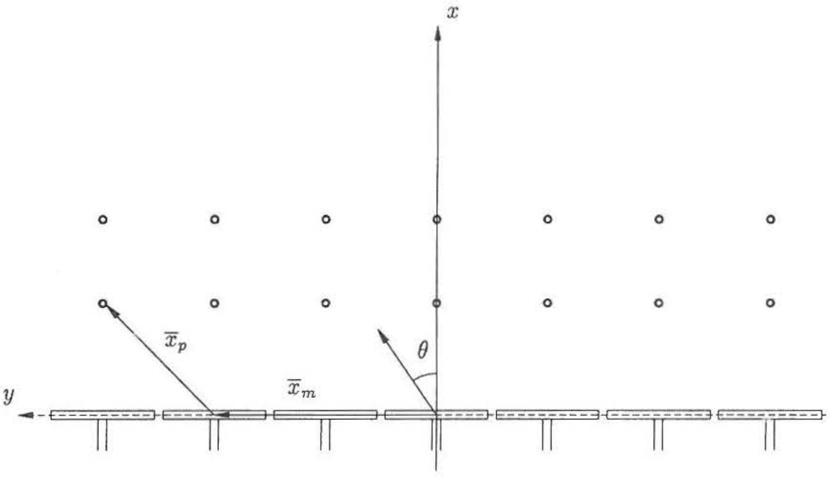

Figure 5.2: Definition sketch.

When tests involving reproduction of irregular, multidirectional waves are performed, the surface elevation in the position $\overline{x} = (x, y)$ in the wave field in front of the wave generator is given by

$$\begin{aligned} \eta(\overline{x}, t) &= \eta^I(\overline{x}, t) + \eta^R(\overline{x}, t) \\ &= \sum_{i=1}^{I} \sum_{j=1}^{J} A_{ij}^I \cos(\omega_i t - \overline{k}_{ij}\overline{x} + \phi_{ij}^I) + \\ &\quad \sum_{i=1}^{I} \sum_{j=1}^{J} A_{ij}^R \cos(\omega_i t + \overline{k}_{ij}\overline{x} + \phi_{ij}^R) \end{aligned} \tag{5.1}$$

where $\omega_i = i\Delta\omega$

$$\overline{k}_{ij} = k_i \begin{bmatrix} \cos\theta_j \\ \sin\theta_j \end{bmatrix}$$

$$\theta_j = j\Delta\theta - \tfrac{\pi}{2}$$

$$\Delta\theta = \tfrac{\pi}{J}$$

and superscript I and R denote incident and reflected, respectively. Thus, the incident wave field is comprised by waves propagating at directions ranging from $-\frac{\pi}{2}$ to $\frac{\pi}{2}$, and

waves propagating at directions from $\frac{\pi}{2}$ to $\frac{3\pi}{2}$ are regarded as reflected waves.
As the reflected wave components reach the wave generator, they are reflected off the front of the wave generator giving rise to a rereflected wave field. Assuming that the wave generator is fully reflective and that Snells law is applicable, the rereflected wave field is given by

$$\eta^{RR}(\overline{x},t) = \sum_{i=1}^{I}\sum_{j=1}^{J} A_{ij}^{R} \cos(\omega_i t - \overline{k}_{ij}\overline{\overline{T}}\overline{x} + \phi_{ij}^{R}) \tag{5.2}$$

where $\overline{\overline{T}} = \begin{bmatrix} 1 & 0 \\ 0 & -1 \end{bmatrix}$

In principle, active absorption of reflected wave components is performed by generating wave components which are identical to the rereflected components except for a phase shift of π. When superposed, these rereflected and generated wave components cancel out, and the problem of rereflection is eliminated. Thus, the generated wave field corresponding to absorption of the reflected wave components is given by

$$\eta^{-RR}(\overline{x},t) = \sum_{i=1}^{I}\sum_{j=1}^{J} A_{ij}^{R} \cos(\omega_i t - \overline{k}_{ij}\overline{\overline{T}}\overline{x} + \phi_{ij}^{R} + \pi) \tag{5.3}$$

The corresponding wave generator displacement signal is given by (see sec. 4.2)

$$X^{-RR}(\overline{x},t) \quad = \quad \sum_{i=1}^{I}\sum_{j=1}^{J} \frac{\cos(\theta_j)}{K_f(\omega_i)} A_{ij}^{R} \cos(\omega_i t - \overline{k}_{ij}\overline{\overline{T}}\overline{x} + \phi_{ij}^{R} - \phi_f + \pi) \tag{5.4}$$

Considering an individual wave paddle centred in the position $\overline{x}$, the desired paddle displacement signal, i.e. the paddle displacement signal which would cause the directional wave generator to absorb the reflected wave components, is given by eq. (5.4). However, determining the correct displacement signal by means of eq. (5.4) requires a priori knowledge of the reflected wave field (amplitudes, directions and phases of the components comprising the wave field) which is, in general, not available. Consequently, the correct paddle displacement signal must be estimated based on measured quantities.

As described above (sec. 5.2), the displacement signal corresponding to each individual wave paddle is obtained by means of linear filtering and subsequent superposition of surface elevation time series measured at locations $\overline{x}_p$, $p = 1..P$ in the wave field in front of the wave generator (see fig. 5.2).
Consider an individual wave paddle centred in $\overline{x}_m = (0, y_m)$.
Denoting the gain and phase of the p'th linear filter by $|\mathcal{H}_p(\omega_i)|$ and $\Phi_p(\omega_i)$, respectively, we obtain the following displacement signal

$$X^{*}(\overline{x}_m,t) \quad = \quad X^{*I}(\overline{x}_m,t) + X^{*R}(\overline{x}_m,t)$$

$$\begin{aligned}
&= \sum_{p=1}^{P}\sum_{i=1}^{I}\sum_{j=1}^{J} |\mathcal{H}_p(\omega_i)| A_{ij}^{I} \cos(\omega_i t - \overline{k}_{ij}(\overline{x}_m + \overline{x}_p) + \phi_{ij}^{I} + \Phi_p(\omega_i)) \\
&\quad + \sum_{p=1}^{P}\sum_{i=1}^{I}\sum_{j=1}^{J} |\mathcal{H}_p(\omega_i)| A_{ij}^{R} \cos(\omega_i t + \overline{k}_{ij}(\overline{x}_m + \overline{x}_p) + \phi_{ij}^{R} + \Phi_p(\omega_i)) \\
&= \sum_{p=1}^{P}\sum_{i=1}^{I}\sum_{j=1}^{J} |\mathcal{H}_p(\omega_i)| A_{ij}^{I} \cos(\omega_i t - k_i y_m \sin\theta_j - \overline{k}_{ij}\overline{x}_p + \phi_{ij}^{I} + \Phi_p(\omega_i)) \\
&\quad + \sum_{p=1}^{P}\sum_{i=1}^{I}\sum_{j=1}^{J} |\mathcal{H}_p(\omega_i)| A_{ij}^{R} \cos(\omega_i t + k_i y_m \sin\theta_j + \overline{k}_{ij}\overline{x}_p + \phi_{ij}^{R} + \Phi_p(\omega_i))
\end{aligned} \tag{5.5}$$

The displacement signals defined by eq. (5.5) cause the wave generator to generate an additional wave field. Assuming that the width of the individual paddles is infinitesimal (no spurious waves appear, see sec. 4.5), this additional wave field is given by

$$\begin{aligned}
\eta^*(\overline{x},t) &= \eta^{*I}(\overline{x},t) + \eta^{*R}(\overline{x},t) \\
&= \sum_{p=1}^{P}\sum_{i=1}^{I}\sum_{j=1}^{J} |\mathcal{H}_p(\omega_i)| \frac{K_f(\omega_i)}{\cos(\theta_j)} A_{ij}^{I} \cos(\omega_i t - \overline{k}_{ij}\overline{x} - \overline{k}_{ij}\overline{x}_p + \phi_{ij}^{I} + \phi_f + \Phi_p(\omega_i)) \\
&\quad + \sum_{p=1}^{P}\sum_{i=1}^{I}\sum_{j=1}^{J} |\mathcal{H}_p(\omega_i)| \frac{K_f(\omega_i)}{\cos(\theta_j)} A_{ij}^{R} \cos(\omega_i t - \overline{k}_{ij}\overline{\overline{T}}\overline{x} + \overline{k}_{ij}\overline{x}_p + \phi_{ij}^{R} + \phi_f + \Phi_p(\omega_i))
\end{aligned} \tag{5.6}$$

In order to cancel out the rereflected wave field, $\eta^*(\overline{x},t)$ should equal $\eta^{-RR}(\overline{x},t)$.
Consequently, our objective is to minimise the difference between $\eta^*(\overline{x},t)$ given by eq. (5.6) and the correct value of $\eta^{-RR}(\overline{x},t)$ given by eq. (5.3). Comparison of eqs. (5.6) and (5.3) reveals that this is achieved by

1. Minimising the difference between $\eta^{*R}(\overline{x},t)$ and $\eta^{-RR}(\overline{x},t)$.
2. Minimising $\eta^{*I}(\overline{x},t)$.

because $\eta^{*R}(\overline{x},t)$ and $\eta^{-RR}(\overline{x},t)$ are functions of the reflected wave field parameters (A_{ij}^{R} and ϕ_{ij}^{R}) whereas $\eta^{*I}(\overline{x},t)$ is a function of the incident wave field parameters (A_{ij}^{I} and ϕ_{ij}^{I}).
The variables in this minimisation problem are the filter characteristics $|\mathcal{H}_p(\omega_i)|$ and $\Phi_p(\omega_i)$. In the following, requirements no. 1 and no. 2 will be formulated in terms of these variables.
The variables $|\mathcal{H}_p(\omega_i)|$ and $\Phi_p(\omega_i)$ are functions of ω_i. Thus the optimal choice of these values, i.e. the choice of $|\mathcal{H}_p(\omega_i)|$ and $\Phi_p(\omega_i)$ which minimises the difference between the generated signal $\eta^*(\overline{x},t)$ and the correct signal $\eta^{-RR}(\overline{x},t)$, must be determined at each frequency ω_i.
Considering the frequency ω_i we obtain the generated signal

$$\begin{aligned}
\eta_i^*(\overline{x},t) &= \eta_i^{*I}(\overline{x},t) + \eta_i^{*R}(\overline{x},t) \\
&= \sum_{p=1}^{P}\sum_{j=1}^{J} |\mathcal{H}_p(\omega_i)| \frac{K_f(\omega_i)}{\cos(\theta_j)} A_{ij}^{I} \cos(\omega_i t - \overline{k}_{ij}\overline{x} - \overline{k}_{ij}\overline{x}_p + \phi_{ij}^{I} + \phi_f + \Phi_p(\omega_i)) \\
&\quad + \sum_{p=1}^{P}\sum_{j=1}^{J} |\mathcal{H}_p(\omega_i)| \frac{K_f(\omega_i)}{\cos(\theta_j)} A_{ij}^{R} \cos(\omega_i t - \overline{k}_{ij}\overline{\overline{T}}\overline{x} + \overline{k}_{ij}\overline{x}_p + \phi_{ij}^{R} + \phi_f + \Phi_p(\omega_i))
\end{aligned} \tag{5.7}$$

whereas the correct signal is given by

$$\eta_i^{-RR}(\overline{x},t) = \sum_{j=1}^{J} A_{ij}^R \cos(\omega_i t - \overline{k}_{ij}\overline{\overline{T}}\overline{x} + \phi_{ij}^R + \pi) \tag{5.8}$$

Furthermore, taking only one directional component j into consideration yields the following generated signal

$$\begin{aligned}
\eta_{ij}^*(\overline{x},t) &= \eta_{ij}^{*I}(\overline{x},t) + \eta_{ij}^{*R}(\overline{x},t) \\
&= \sum_{p=1}^{P} |\mathcal{H}_p(\omega_i)| \frac{K_f(\omega_i)}{\cos(\theta_j)} A_{ij}^I \cos(\omega_i t - \overline{k}_{ij}\overline{x}_p - \overline{k}_{ij}\overline{x} + \phi_{ij}^I + \phi_f + \Phi_p(\omega_i)) \\
&\quad + \sum_{p=1}^{P} |\mathcal{H}_p(\omega_i)| \frac{K_f(\omega_i)}{\cos(\theta_j)} A_{ij}^R \cos(\omega_i t + \overline{k}_{ij}\overline{x}_p - \overline{k}_{ij}\overline{\overline{T}}\overline{x} + \phi_{ij}^R + \phi_f + \Phi_p(\omega_i))
\end{aligned} \tag{5.9}$$

whereas the correct signal is given by

$$\eta_{ij}^{-RR}(\overline{x},t) = A_{ij}^R \cos(\omega_i t - \overline{k}_{ij}\overline{\overline{T}}\overline{x} + \phi_{ij}^R + \pi) \tag{5.10}$$

In the following, requirement no. 1 is formulated.

Rewriting eqs. (5.9) and (5.10), the generated signal $\eta_{ij}^{*R}(\overline{x},t)$ and the correct signal $\eta_{ij}^{-RR}(\overline{x},t)$ can be written as

$$\eta_{ij}^{*R}(\overline{x},t) = a_{ij}^{*R} \cos(\omega_i t - \overline{k}_{ij}\overline{\overline{T}}\overline{x} + \phi_{ij}^R) - b_{ij}^{*R} \sin(\omega_i t - \overline{k}_{ij}\overline{\overline{T}}\overline{x} + \phi_{ij}^R) \tag{5.11}$$

$$\eta_{ij}^{-RR}(\overline{x},t) = -A_{ij}^R \cos(\omega_i t - \overline{k}_{ij}\overline{\overline{T}}\overline{x} + \phi_{ij}^R) \tag{5.12}$$

where the coefficients a_{ij}^{*R} and b_{ij}^{*R} are given by

$$a_{ij}^{*R} = \sum_{p=1}^{P} |\mathcal{H}_p(\omega_i)| \frac{K_f(\omega_i)}{\cos(\theta_j)} A_{ij}^R \cos(\overline{k}_{ij}\overline{x}_p + \Phi_p(\omega_i) + \phi_f) \tag{5.13}$$

$$b_{ij}^{*R} = \sum_{p=1}^{P} |\mathcal{H}_p(\omega_i)| \frac{K_f(\omega_i)}{\cos(\theta_j)} A_{ij}^R \sin(\overline{k}_{ij}\overline{x}_p + \Phi_p(\omega_i) + \phi_f) \tag{5.14}$$

Introducing the complex filter frequency response $\mathcal{H}_p(\omega_i) = \mathcal{H}_{ip}$ (see App. A and below), eqs. (5.13) and (5.14) are rewritten as

$$a_{ij}^{*R} = A_{ij}^R \sum_{p=1}^{P} (\mathcal{G}_{ijp}^R.re \cdot \mathcal{H}_{ip}.re - \mathcal{G}_{ijp}^R.im \cdot \mathcal{H}_{ip}.im) \tag{5.15}$$

$$b_{ij}^{*R} = A_{ij}^R \sum_{p=1}^{P} (\mathcal{G}_{ijp}^R.re \cdot \mathcal{H}_{ip}.im + \mathcal{G}_{ijp}^R.im \cdot \mathcal{H}_{ip}.re) \tag{5.16}$$

where

$$\begin{aligned}
\mathcal{G}^R_{ijp}.re &= \frac{K_f(\omega_i)}{\cos(\theta_j)}\cos(\overline{k}_{ij}\overline{x}_p + \phi_f) && (5.17)\\
\mathcal{G}^R_{ijp}.im &= \frac{K_f(\omega_i)}{\cos(\theta_j)}\sin(\overline{k}_{ij}\overline{x}_p + \phi_f) && (5.18)\\
\mathcal{H}_{ip}.re &= |\mathcal{H}_p(\omega_i)|\cos(\Phi_p(\omega_i)) && (5.19)\\
\mathcal{H}_{ip}.im &= |\mathcal{H}_p(\omega_i)|\sin(\Phi_p(\omega_i)) && (5.20)
\end{aligned}$$

The ratio of the amplitude of the difference between the generated signal $\eta^{*R}_{ij}(\overline{x},t)$ and the correct signal $\eta^{-RR}_{ij}(\overline{x},t)$ and the amplitude of the correct signal is given by

$$\begin{aligned}
\epsilon^R_j(\omega_i) &= \frac{amp\left(\eta^{*R}_{ij}(\overline{x},t) - \eta^{-RR}_{ij}(\overline{x},t)\right)}{amp\left(\eta^{-RR}_{ij}(\overline{x},t)\right)}\\
&= \frac{1}{A^R_{ij}}\sqrt{(a^{*R}_{ij} + A^R_{ij})^2 + (b^{*R}_{ij})^2}\\
&= \sqrt{(\sum_{p=1}^{P}(\mathcal{G}^R_{ijp}.re \cdot \mathcal{H}_{ip}.re - \mathcal{G}^R_{ijp}.im \cdot \mathcal{H}_{ip}.im) + 1)^2 + (\sum_{p=1}^{P}(\mathcal{G}^R_{ijp}.re \cdot \mathcal{H}_{ip}.im + \mathcal{G}^R_{ijp}.im \cdot \mathcal{H}_{ip}.re))^2} && (5.21)
\end{aligned}$$

where $amp\,(x(t))$ denotes the amplitude of the harmonic function $x(t)$.
The ratio $\epsilon^R_j(\omega_i)$ represents the relative *amplitude* of the difference between the generated signal $\eta^{*R}_{ij}(\overline{x},t)$ and the correct signal $\eta^{-RR}_{ij}(\overline{x},t)$ at the direction j. Thus, the squared ratio $\epsilon^R_j(\omega_i)^2$ represents the relative *energy* of the difference between the generated signal $\eta^{*R}_{ij}(\overline{x},t)$ and the correct signal $\eta^{-RR}_{ij}(\overline{x},t)$ at the direction j. In order to obtain a measure of relative energy of the difference between the generated signal $\eta^{*R}_{i}(\overline{x},t)$ and the correct signal $\eta^{-RR}_{i}(\overline{x},t)$, the distribution of wave energy over the directions θ_j, $j = 1..J$ in the reflected wave field must be taken into consideration. Thus, each squared ratio $\epsilon^R_j(\omega_i)^2$ is assigned a weight c^R_j proportional to the value of the expected directional spreading function of the reflected wave field (see sec. 4.1). The weighted sum of the squared ratios $\epsilon^R_j(\omega_i)^2$ corresponding to directions $j = 1..J$ is computed

$$\begin{aligned}
\delta^R(\omega_i) &= \sum_{j=1}^{J} c^R_j \epsilon^R_j(\omega_i)^2\\
&= \sum_{j=1}^{J} c^R_j \left(\sum_{p=1}^{P}(\mathcal{G}^R_{ijp}.re \cdot \mathcal{H}_{ip}.re - \mathcal{G}^R_{ijp}.im \cdot \mathcal{H}_{ip}.im) + 1\right)^2\\
&\quad + \sum_{j=1}^{J} c^R_j \left(\sum_{p=1}^{P}(\mathcal{G}^R_{ijp}.re \cdot \mathcal{H}_{ip}.im + \mathcal{G}^R_{ijp}.im \cdot \mathcal{H}_{ip}.re)\right)^2 && (5.22)
\end{aligned}$$

This function is a measure of the difference between $\eta^{*R}_{i}(\overline{x},t)$ and $\eta^{-RR}_{i}(\overline{x},t)$, i.e. a measure of how well requirement no. 1 is met.

Using the same procedure, a measure of the difference between $\eta^{*I}_{i}(\overline{x},t)$ and 0 (as mentioned above in requirement no. 2, $\eta^{*I}_{i}(\overline{x},t)$ should be minimised) can be obtained as

$$\begin{aligned}
\delta^I(\omega_i) &= \sum_{j=1}^{J} c_j^I \epsilon_j^I(\omega_i)^2 \\
&= \sum_{j=1}^{J} c_j^I \left(\frac{amp\left(\eta_{ij}^{*I}(\overline{x},t)\right)}{amp\left(\eta_{ij}^{I}(\overline{x},t)\right)} \right)^2 \\
&= \sum_{j=1}^{J} c_j^I \left(\sum_{p=1}^{P} (\mathcal{G}_{ijp}^I.re \cdot \mathcal{H}_{ip}.re - \mathcal{G}_{ijp}^I.im \cdot \mathcal{H}_{ip}.im) \right)^2 \\
&\quad + \sum_{j=1}^{J} c_j^I \left(\sum_{p=1}^{P} (\mathcal{G}_{ijp}^I.re \cdot \mathcal{H}_{ip}.im + \mathcal{G}_{ijp}^I.im \cdot \mathcal{H}_{ip}.re) \right)^2 \qquad (5.23)
\end{aligned}$$

where

$$\mathcal{G}_{ijp}^I.re = \frac{K_f(\omega_i)}{\cos(\theta_j)} \cos(-\overline{k}_{ij}\overline{x}_p + \phi_f) \qquad (5.24)$$

$$\mathcal{G}_{ijp}^I.im = \frac{K_f(\omega_i)}{\cos(\theta_j)} \sin(-\overline{k}_{ij}\overline{x}_p + \phi_f) \qquad (5.25)$$

Requirements no. 1 and 2 have now been formulated in terms of the complex filter frequency response $\mathcal{H}_{ip}$ of filters $p = 1..P$. The function $\delta^R(\omega_i)$ provides a measure of how well requirement no. 1 is met and $\delta^I(\omega_i)$ provides a measure of how well requirement no. 2 is met. In order to minimise the difference between the generated signal $\eta_i^*(\overline{x},t)$ and the correct signal $\eta_i^{-RR}(\overline{x},t)$, both $\delta^R(\omega_i)$ and $\delta^I(\omega_i)$ should be minimised. However, this would result in two different sets of complex filter frequency responses $\mathcal{H}_{ip}$ of filters $p = 1..P$. In order to obtain one set of complex filter frequency responses, the *sum* of $\delta^R(\omega_i)$ and $\delta^I(\omega_i)$ is minimised (In principle, $\delta^R(\omega_i)$ and $\delta^I(\omega_i)$ should be weighted according to the total amount of wave energy present in the reflected and incident wave fields, respectively. However, for convenience, this will not be done). The function

$$\delta(\omega_i) = \delta^I(\omega_i) + \delta^R(\omega_i) \qquad (5.26)$$

may thus be regarded as a measure of the difference between the total generated signal $\eta_i^*(\overline{x},t)$ and the correct signal $\eta_i^{-RR}(\overline{x},t)$. This function is minimised in order to minimise the difference between the generated signal and the correct signal (as described above, the variables in the function are the complex frequency responses $\mathcal{H}_{ip},\ p = 1..P$ of the linear filters).

Thus, the derivative of $\delta(\omega_i)$ with respect to $\mathcal{H}_{ip}$ is determined and set equal to zero

$$\frac{\partial \delta(\omega_i)}{\partial \mathcal{H}_{ip}.re} = 0, \quad p = 1..P \qquad (5.27)$$

$$\frac{\partial \delta(\omega_i)}{\partial \mathcal{H}_{ip}.im} = 0, \quad p = 1..P \qquad (5.28)$$

This yields a linear equation system with $2 \cdot P$ equations and $2 \cdot P$ unknowns. This system of equations can be written as

$$\overline{\overline{E}} \cdot \overline{z} = \overline{f} \tag{5.29}$$

where

$$
\begin{aligned}
E[p', p] &= \sum_{j=1}^{J} c_j^I \cdot (\mathcal{G}_{ijp}^I.re \cdot \mathcal{G}_{ijp'}^I.re + \mathcal{G}_{ijp}^I.im \cdot \mathcal{G}_{ijp'}^I.im) \\
&\quad + \sum_{j=1}^{J} c_j^R \cdot (\mathcal{G}_{ijp}^R.re \cdot \mathcal{G}_{ijp'}^R.re + \mathcal{G}_{ijp}^R.im \cdot \mathcal{G}_{ijp'}^R.im) && (5.30) \\
E[p', p+P] &= \sum_{j=1}^{J} c_j^I \cdot (-\mathcal{G}_{ijp}^I.im \cdot \mathcal{G}_{ijp'}^I.re + \mathcal{G}_{ijp}^I.re \cdot \mathcal{G}_{ijp'}^I.im) \\
&\quad + \sum_{j=1}^{J} c_j^R \cdot (-\mathcal{G}_{ijp}^R.im \cdot \mathcal{G}_{ijp'}^R.re + \mathcal{G}_{ijp}^R.re \cdot \mathcal{G}_{ijp'}^R.im) && (5.31) \\
E[p'+P, p] &= \sum_{j=1}^{J} c_j^I \cdot (-\mathcal{G}_{ijp}^I.re \cdot \mathcal{G}_{ijp'}^I.im + \mathcal{G}_{ijp}^I.im \cdot \mathcal{G}_{ijp'}^I.re) \\
&\quad + \sum_{j=1}^{J} c_j^R \cdot (-\mathcal{G}_{ijp}^R.re \cdot \mathcal{G}_{ijp'}^R.im + \mathcal{G}_{ijp}^R.im \cdot \mathcal{G}_{ijp'}^R.re) && (5.32) \\
E[p'+P, p+P] &= \sum_{j=1}^{J} c_j^I \cdot (\mathcal{G}_{ijp}^I.im \cdot \mathcal{G}_{ijp'}^I.im + \mathcal{G}_{ijp}^I.re \cdot \mathcal{G}_{ijp'}^I.re) \\
&\quad + \sum_{j=1}^{J} c_j^R \cdot (\mathcal{G}_{ijp}^R.im \cdot \mathcal{G}_{ijp'}^R.im + \mathcal{G}_{ijp}^R.re \cdot \mathcal{G}_{ijp'}^R.re) && (5.33) \\
f[p'] &= -\sum_{j=1}^{J} c_j^R \mathcal{G}_{ijp'}^R.re && (5.34) \\
f[p'+P] &= \sum_{j=1}^{J} c_j^R \mathcal{G}_{ijp'}^R.im && (5.35) \\
z[p'] &= \mathcal{H}_{ip'}.re && (5.36) \\
z[p'+P] &= \mathcal{H}_{ip'}.im && (5.37) \\
p' &= 1..P && (5.38) \\
p &= 1..P && (5.39)
\end{aligned}
$$

Solving this equation system with respect to $\overline{z}$ yields the complex frequency responses of linear filters $1..P$ corresponding to the minimum error between the generated signal and the signal corresponding to absorption of reflected wave components.

5.4 Physical Model Tests

5.4.1 Test Set-up

In order to determine the performance of an absorbing directional wave generator based on the method described above, a series of physical model tests were performed.

The conventional directional wave generator applied in the laboratory wave generation tests presented in chap. 4 (the directional wave generator in the 3-D wave basin at the Hydraulics & Coastal Engineering Laboratory, Aalborg University) was converted into an absorbing directional wave generator based on the new method. As described in sec. 4.7, this directional wave generator is comprised by nine wave paddles of width 0.90 m hinged with vertical axes to ten hydraulic pistons (see fig. 5.3).

Converting a conventional directional wave generator into an absorbing directional wave generator based on the method described above is relatively simple: only the wave generator control system is modified; the wave generator itself requires no modifications.

In fig. 5.3, the test set-up is depicted.

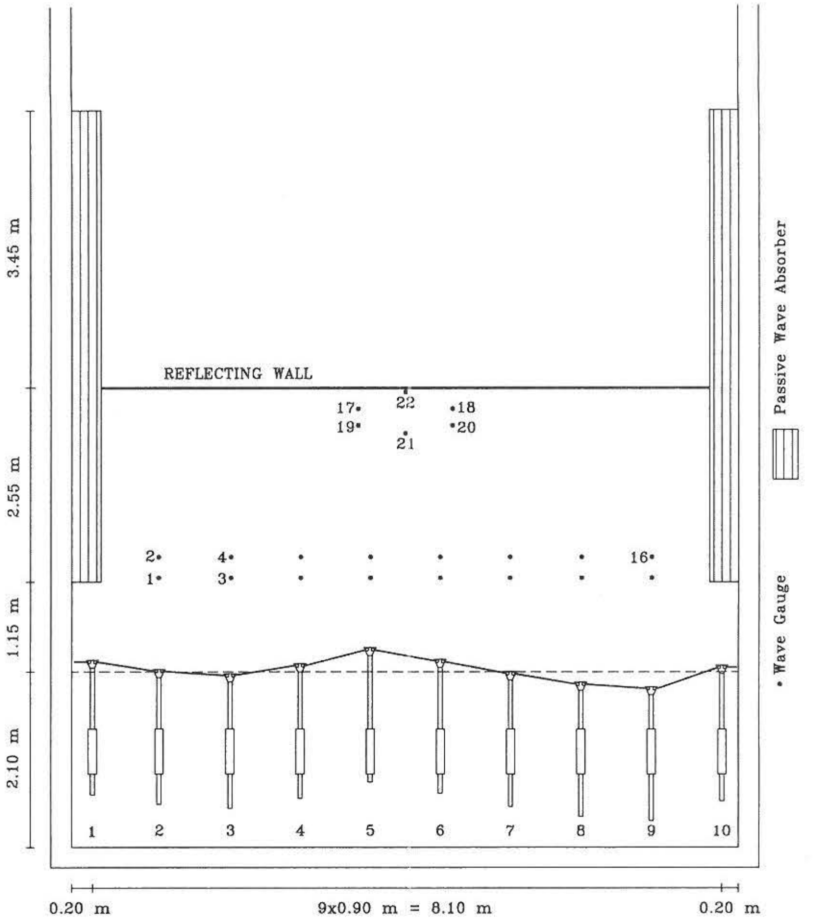

Figure 5.3: Test set-up, Hydraulics & Coastal Eng. Laboratory 3-D wave basin.

The active absorption system was based on surface elevation signals measured in 16 positions in the wave field in front of the directional wave generator. The 16 wave gauges were arranged along two lines parallel to the front of the wave generator as shown in fig. 5.3 (wave gauges 1-16).

For pistons 3-8 (see fig. 5.3), the individual piston displacement correction signals corresponding to absorption of the reflected wave field were estimated by means of linear filtering and subsequent superposition of surface elevation signals measured in $P = 6$ positions in front of the piston. The surface elevation signals from the 6 nearest wave gauges were applied. The geometries of the wave gauge arrays corresponding to pistons 3-8 is given in fig. 5.4.

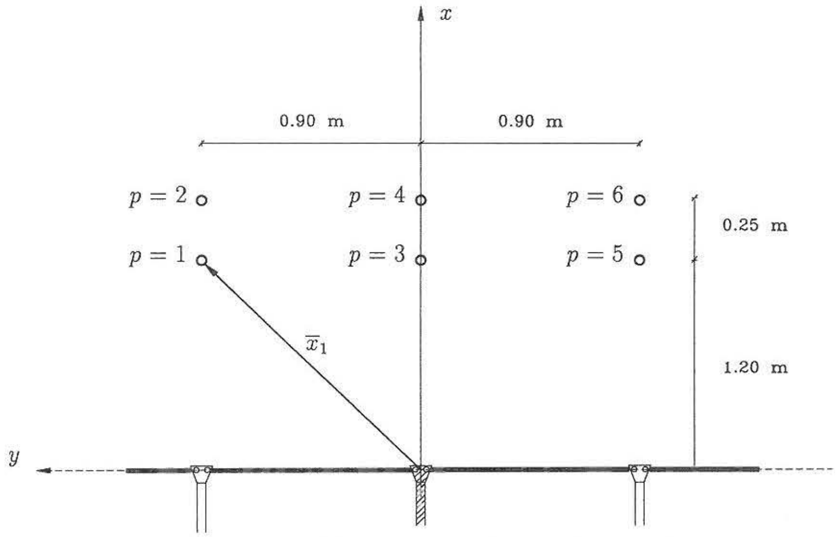

Figure 5.4: Wave gauge positions, pistons 3-8.

For pistons 2 and 9, the individual piston displacement correction signals were estimated based on surface elevation signals measured in the two wave gauges in front of the piston. The piston displacement correction signals for pistons 2 and 9 were also applied to pistons 1 and 10, respectively.

In order to obtain a high degree of reflection from the far end of the wave basin, a reflecting wall was installed at a distance of 3.70 m from the directional wave generator parallel to the wave generator front. The reflecting wall spanned the entire width of the basin (see fig. 5.3).

All tests were performed with a water depth of $d = 0.35\,\mathrm{m}$, i.e. the water depth was the same as in the wave generation tests described in sec. 4.7.

The tests performed represented an attempt to reproduce the incident wave fields generated in laboratory wave generation tests 1 and 2 described in sec. 4.7 with a highly reflective structure (the reflecting wall) installed in the basin. Consequently, a Pierson-Moskowitz type target incident wave frequency spectrum was applied, and tests involving two different Mitsuyasu type target incident wave directional spreading functions were performed. In order to compare the performance of the absorbing directional wave generator with the performance of a conventional directional wave generator, each test was performed both with and without applying the active absorption system.
In fig. 5.5, the test program is given. The target significant wave height has been reduced by 20% relative to the corresponding wave generation tests described in sec. 4.7. This reduction was made in order to obtain approximately the same level of total wave energy as in the wave generation tests described in sec. 4.7 (where no wave reflection occured) and thus the same level of higher order effects and the same signal/noise-ratio.

Test no.	f_p	H_s	θ_0	s	abs.
	Hz	m	deg		on/off
1a	0.8	0.04	0	6	on
1b	0.8	0.04	0	6	off
2a	0.8	0.04	0	12	on
2b	0.8	0.04	0	12	off

Figure 5.5: Test program, 3-D active wave absorption tests.

5.4.2 Filter Design

Having defined the geometry of the wave gauge array corresponding to each individual piston, the remaining problem in converting the conventional wave generator into an absorbing wave generator is to determine the desired filter frequency response of the linear filters applied and designing linear filters which match the desired frequency responses.

For pistons 3-8, the geometry of the wave gauge array, i.e. the wave gauge positions $\overline{x}_p$ ($p = 1..6$), is given in fig. 5.4. At first, the desired complex frequency responses of filters 1 to 6 corresponding to a frequency of $f_i = 0.80\,\text{Hz}$ (the target incident frequency spectrum peak frequency) were determined as described in the previous section by solving the linear equation system eq. (5.29). The weighting functions c_j^I and c_j^R were determined based on Mitsuyasu-type spreading functions characterised by a mean direction of $\theta_0 = 0\,\text{deg}$ and a spreading parameter of $s = 12$. $J = 288$ directions of propagation were applied. For all directions of propagation outside the interval $-\frac{\pi}{4} < \theta_j < \frac{\pi}{4}$, values of $c_j^I = 0$ and $c_j^R = 0$ were applied. The gain and phase of the freq. responses corresponding to $f_i = 0.80\,\text{Hz}$ ($\omega_i \approx 5.03\,\text{rad/s}$) are given below.

p	$\vert\mathcal{H}_p(0.8Hz)\vert$	$\Phi_p(0.8Hz)$
		rad
1	0.2468	-2.5433
2	0.2022	1.3310
3	0.6064	-0.7162
4	0.6084	3.0825
5	0.2468	-2.5433
6	0.2022	1.3310

Due to the symmetry of the wave gauge array around the x-axis (see fig. 5.4), the frequency responses of the linear filters corresponding to wave gauges 1 and 2 are identical to the frequency responses of the linear filters corresponding to wave gauges 5 and 6, respectively. Consequently, only 4 linear filters are required.

Based on the frequency responses given above, the performance of the absorbing directional wave generator for a wave frequency of $f_i = 0.8\,\mathrm{Hz}$ was determined by computing parameters $\epsilon_j^R(0.80Hz)$ and $\epsilon_j^I(0.80Hz)$ for directions θ_j, $j = 1..J$ as described in sec. 5.3.
The ratio $\epsilon_j^R(\omega_i)$ of the amplitude of the difference between the generated signal $\eta_{ij}^{*R}(\overline{x},t)$ and the correct signal $\eta_{ij}^{-RR}(\overline{x},t)$ and the amplitude of the correct signal $\eta_{ij}^{-RR}(\overline{x},t)$, given by eq. (5.21), is plotted in fig. 5.6a.
The ratio $\epsilon_j^I(\omega_i)$ of the amplitude of the generated signal $\eta_{ij}^{*I}(\overline{x},t)$ and the amplitude of the incident wave field $\eta_{ij}^I(\overline{x},t)$ is plotted in fig. 5.6b.

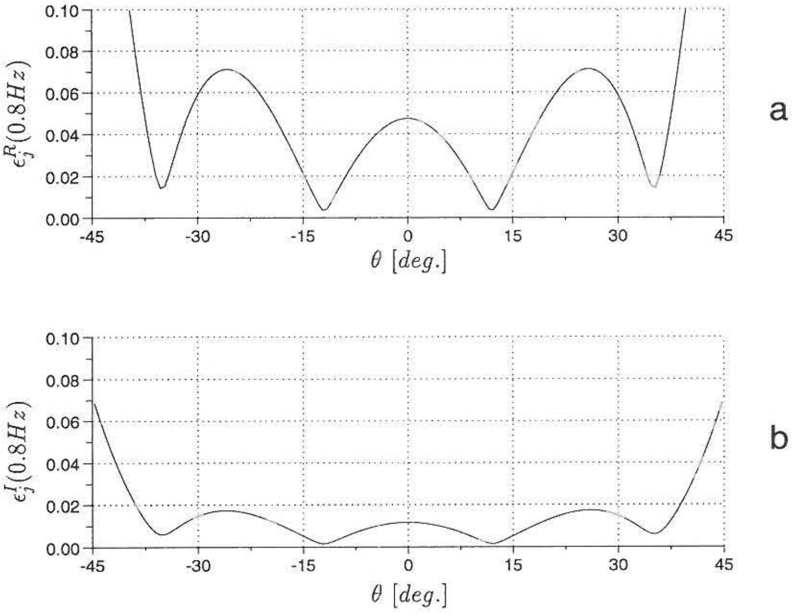

Figure 5.6: Parameters $\epsilon_j^I(\omega_i)$ and $\epsilon_j^R(\omega_i)$, $f_i = 0.8\,\mathrm{Hz}$.

Fig. 5.6a shows that the amplitude of the error $\eta_{ij}^{*R}(\overline{x},t) - \eta_{ij}^{-RR}(\overline{x},t)$ is generally less than 7% of the amplitude of the correct signal $\eta_{ij}^{-RR}(\overline{x},t)$. Consequently, requirement no. 1 (see sec. 5.3) has been met satisfactorily.
Fig. 5.6b shows that the amplitude of the generated signal $\eta_{ij}^{*I}(\overline{x},t)$ is generally less than 2% of the amplitude of the incident signal $\eta_{ij}^I(\overline{x},t)$. Thus, requirement no. 2 (see sec. 5.3) has also been met.

The process of determining the desired frequency response for filters $p = 1..4$ was repeated for frequencies of $f_i = \text{i} \cdot 0.08\,\text{Hz}$, $i = 1..25$ and linear digital filters matching the determined frequency responses were designed.
Non-recursive filter operators were used (see App. A). A sample frequency of $f_s = 30\,\text{Hz}$ was chosen and filters with $N = 75$ components were applied. In order to compensate for the phase shift introduced by the delay of the filter operators (see App. A) and the phase shift introduced by the wave generator servocontrol system (see App. B), an additional phase shift of

$$\phi(\omega) = \left(\frac{N-1}{2f_s} + 0.1s\right)\omega \tag{5.40}$$

was introduced in the desired filter operator frequency responses.
The filters were designed by means of the trial-and-error approach described in App. A. For high frequencies, the desired frequency response was characterised by quick transitions in the phase shifts, as was the case with the filters applied in the 2-D active absorption system (see sec. 3.4.2). Thus, for high frequencies, it was found that it was impossible to design non-recursive filters with the desired filter frequency response. Consequently, zero gain was prescribed for $f > 1.5\,\text{Hz}$.

In order to predict the performance of the absorbing directional wave generator in test 2, a numerical test was performed. Surface elevation time series corresponding to gauge positions $\overline{x}_p$, $p = 1..6$ were generated numerically. The target incident wave field in the numerical wave generation was identical to the target incident wave field corresponding to test 2 (see fig. 5.5). The far end of the basin was assumed parallel to the wave generator and fully reflective, thus giving rise to a reflected wave field with parameters identical to those of the incident wave field. The target incident and reflected directional spectra were discretised into $I \cdot J = 15 \cdot 15 = 225$ harmonic components. Each component was assigned a random phase, and the surface elevation signals were generated using a discrete-time version of eq. (5.1).
The estimated piston displacement signal $X^*(t)$ was determined by convolving the numerically generated surface elevation signals with the non-recursive linear filter operators designed for the physical model tests and superposing the filtered signals. Furthermore, the correct piston displacement signal corresponding to full absorption of the reflected wave components, $X^{-RR}(t)$, given by eq. (5.4), was determined. Both signals are given in fig. 5.7. For comparison, the difference between the two signals is given. The piston displacement signal determined by means of linear filtering of the numerically generated surface elevation series is in good agreement with the correct signal. Consequently, the result of the numerical simulation suggests that the performance of the absorbing wave generator will be good.
Notice that the differences between $X^*(t)$ and $X^{-RR}(t)$ (see fig. 5.7) are not only caused by discrepancies between the desired frequency responses and the actual frequency responses of the filters applied: even if the desired and actual frequency responses were in perfect agreement, $X^*(t)$ would still fail to match the correct signal $X^{-RR}(t)$ due to the fact that the error functions $\delta^R(\omega_i)$ and $\delta^I(\omega_i)$ differ from 0. In contrast, the 2-D absorption system (see sec. 3) yields perfect agreement between $X^*(t)$ and $X^{-RR}(t)$ when the actual filter frequency responses match the desired filter frequency responses.

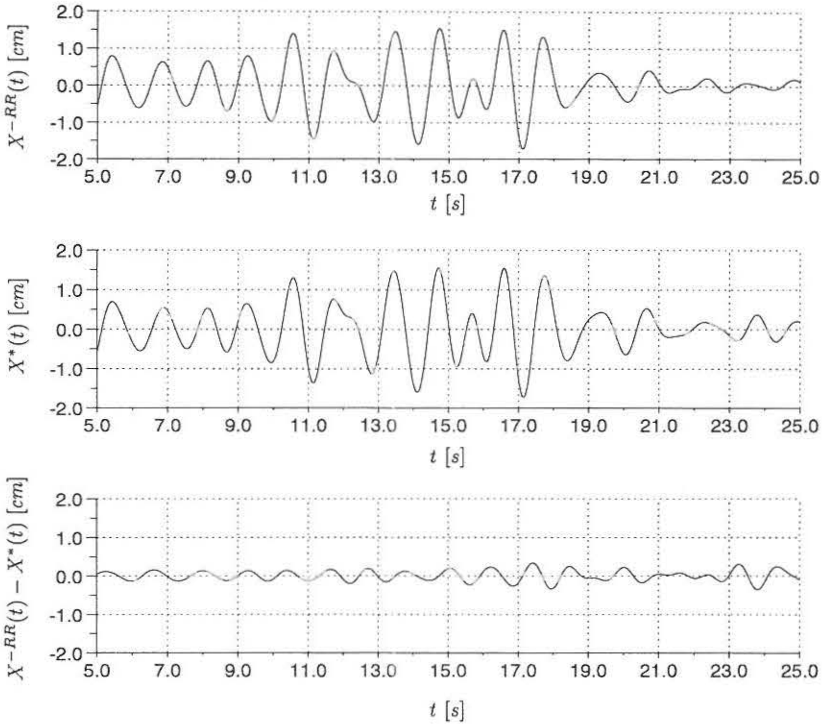

Figure 5.7: Piston displacement signals.

5.4.3 Test Results

Prior to performing the planned irregular wave tests, a series of simple *regular* wave tests involving unidirectional waves were performed.

Waves of frequency $f = 0.85\,\mathrm{Hz}$, amplitude $A^I = 0.015\,\mathrm{m}$ and direction of propagation $\theta = 0\,\mathrm{deg}$ were generated with the wave generator operating in the combined generation/absorption mode. The test was repeated with the wave generator operating as a conventional wave generator, i.e. without active absorption applied. In both tests, surface elevation time series were recorded with a wave gauge installed at a distance of 0.05 m from the reflecting wall (wave gauge 22, fig. 5.3). The recorded surface elevation time series are shown in fig. 5.8.
The regular wave tests were repeated with a direction of propagation of $\theta = 10\,\mathrm{deg}$. Again, surface elevation time series were recorded from wave gauge 22 (see fig. 5.9).

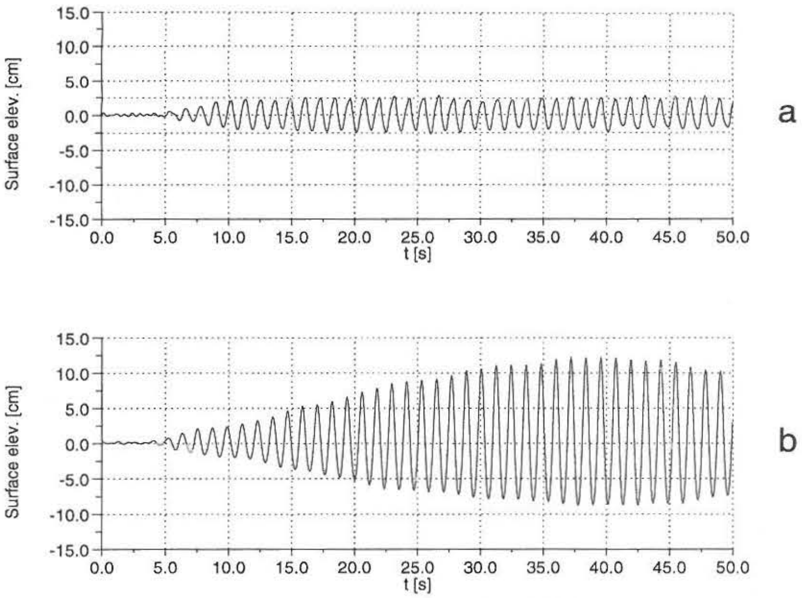

Figure 5.8: Surface elevation time series obtained with (a) and without absorption (b). Regular wave test 1 ($A^I = 0.015\,\mathrm{m}$, $f = 0.85\,\mathrm{Hz}$, $\theta = 0\,\mathrm{deg}$).

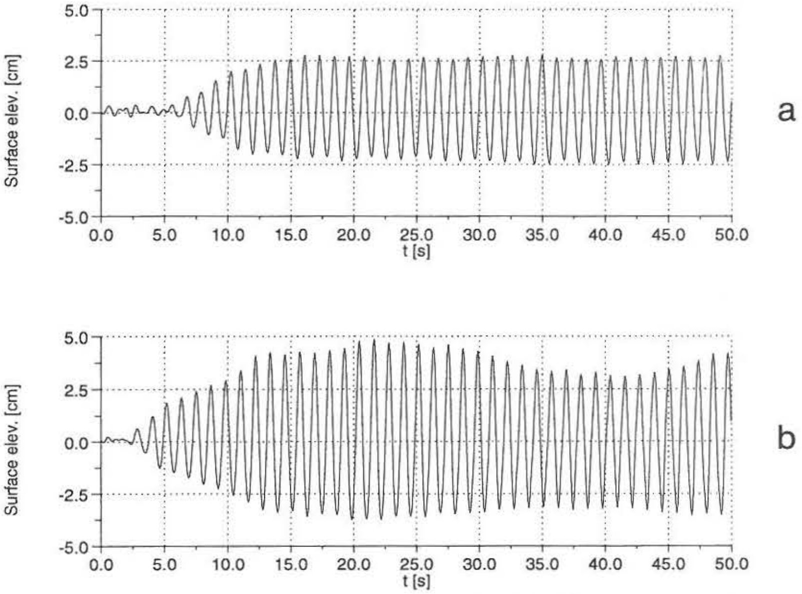

Figure 5.9: Surface elevation time series obtained with (a) and without absorption (b). Regular wave test 2 ($A^I = 0.015\,\mathrm{m}$, $f = 0.85\,\mathrm{Hz}$, $\theta = 10\,\mathrm{deg}$).

Provided the absorbing directional wave generator is capable of eliminating the problem of rereflection, the wave field in front of the wave generator will be a combined wave field comprised by the generated incident wave field and a reflected wave field. The incident and reflected wave fields will form a standing wave pattern with an antinode at the reflecting wall. Thus, a surface elevation time series measured directly in front of the reflecting wall will be a harmonic signal with amplitude $2A^I = 0.030\,\mathrm{m}$ (assuming that the wall is fully reflective and no diffraction occurs).

Figs. 5.8a and 5.9a show that with the wave generator operating as an absorbing directional wave generator, the problem of rereflection is insignificant: the measured time series are harmonic signals with amplitudes of approximately 0.025 m. The reduction in amplitude relative to $2A^I = 0.030\,m$ is as expected: the wall is not fully reflective and diffraction will occur. Furthermore, wave gauge 22 is not placed directly in front of the wall.

Without absorption applied, i.e. with the wave generator operating as a conventional directional wave generator, the wave field is significantly disturbed by rereflection (see figs. 5.8b and 5.9b).

Subsequently, *irregular* wave tests 1a, 1b, 2a and 2b (see fig. 5.5) were performed.

In order to enable estimation of the directional spectrum of the incident wave field in each test, a wave gauge array identical to array 3 described in Encl. 1 was installed in the basin (wave gauges 17-21, see fig. 5.3). In each test, surface elevation time series of length $T = 2048\,\mathrm{s}$ were sampled from wave gauges 17-21 and 22 with a sample frequency of $f_s = 6\,\mathrm{Hz}$.

In the data analysis, the measured time series were divided into subseries of length $512\Delta t \approx 85.3\,\mathrm{s}$ which yields 24 spectral estimates and a frequency domain resolution of $\Delta f \approx 0.0117\,\mathrm{Hz}$.

For each of the 4 irregular wave tests the frequency spectrum of the surface elevation time series measured in wave gauge 22 was determined.

As described above, an efficient absorbing directional wave generator will eliminate the rereflected wave field so that the wave field in front of the wave generator will be a combined wave field comprised only by the generated incident wave components and the corresponding reflected wave components. Each generated incident wave component will form a standing wave pattern with the corresponding reflected wave component with an antinode at the reflecting wall. Consequently, if no rereflection occurs, i.e. if the wave generator is capable of absorbing the reflected wave components, the frequency spectrum of a surface elevation time series measured directly in front of the reflecting wall will be identical in form to the generated incident wave frequency spectrum but with four times the total energy of the generated incident wave frequency spectrum, i.e. with a significant wave height of $H_s = 2H_s^I$ (assuming that the wall is fully reflective and no diffraction occurs).

In figs. 5.10 and 5.11 the measured frequency spectra are given. For comparison, the Pierson-Moskowitz spectrum with peak frequency $f_p = 0.80\,\mathrm{Hz}$ and significant wave height $H_s = 2H_s^I = 0.08\,\mathrm{m}$, i.e. the target frequency spectrum, is plotted.

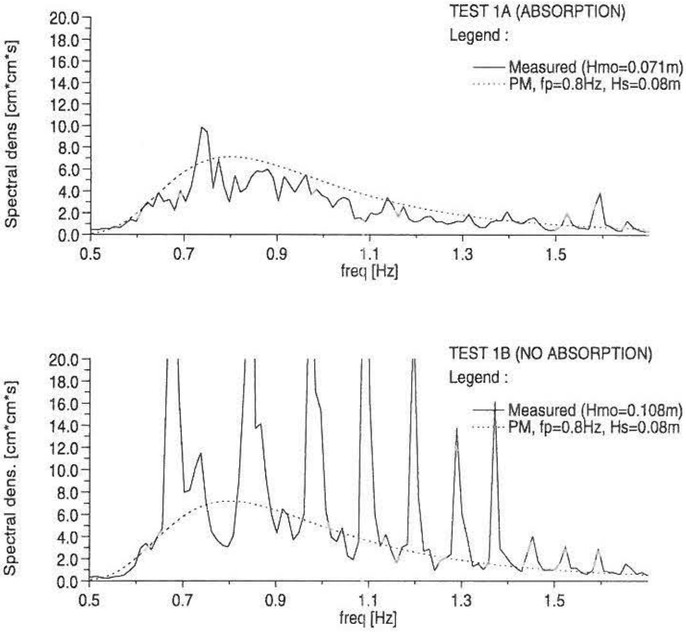

Figure 5.10: Frequency spectra, test 1a and 1b (see fig. 5.5). Wave gauge 22.

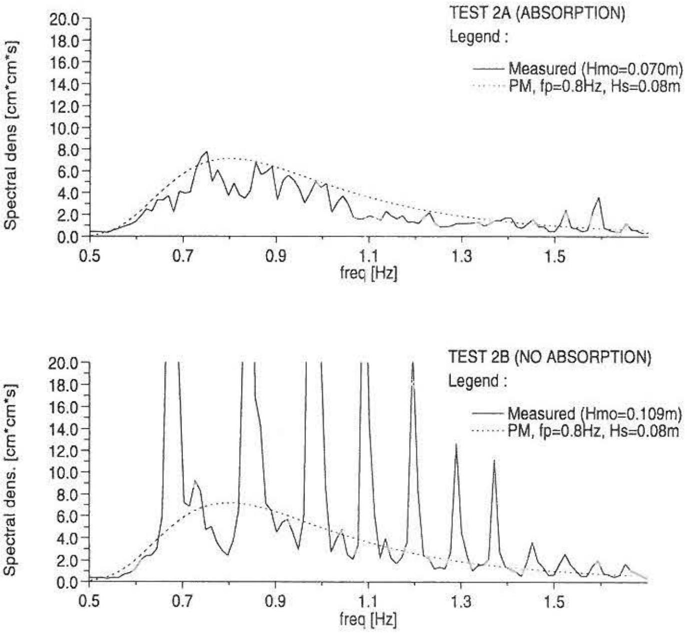

Figure 5.11: Frequency spectra, test 2a and 2b (see fig. 5.5). Wave gauge 22.

Inspection of figs. 5.10 and 5.11 shows that the absorbing directional wave generator is capable of reducing the problem of rereflection significantly.
With the wave generator operating as an absorbing directional wave generator, the measured frequency spectrum is in reasonable agreement with the target frequency spectrum (tests 1a and 2a). However, the measured spectral density is generally lower than the target value. Again, this is as expected: the wall is not fully reflective and wave energy will inevitably be lost through diffraction. Furthermore, wave gauge 22 is not placed directly in front of the wall.
When active absorption is not applied, i.e. with the wave generator operating as a conventional directional wave generator, the measured frequency spectrum is in poor agreement with the target spectrum (tests 1b and 2b). Without active absorption, the measured frequency spectrum is characterised by a number of peaks. In fig. 5.12 the frequencies at which the rereflected wave component is in phase with the generated incident wave component for a direction of propagation of $\theta = 0\,\text{deg}$ are marked (for this direction of propagation, incident and rereflected waves are in phase when twice the distance from the wave generator front to the reflecting wall equals an integer number of wave lengths). Comparison of fig. 5.12 and figs. 5.10b and 5.11b shows that the peaks in the measured frequency spectrum coincide with the frequencies at which the rereflected wave component is in phase with the generated incident wave component.

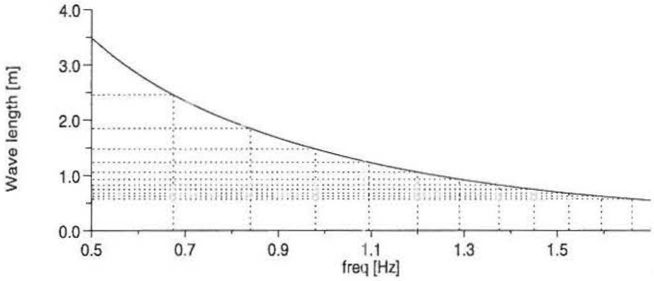

Figure 5.12: Wave length (linear wave theory). Water depth $d = 0.35\,\text{m}$.

Finally, the MLM method based on standard directional spreading functions was applied to the surface elevation time series recorded in wave gauges 17-21 in each irregular wave test in order to estimate the parameters in the *incident* directional spectrum and a frequency dependent reflection coefficient describing the reflection characteristics of the reflecting wall. The standard directional spreading function applied was the Mitsuyasu spreading function, i.e. a mean direction θ_0 and a spreading parameter s were estimated.
In Encl. 1 a detailed description of the MLM method is given (Encl. 1 also includes the results of a series of numerical tests in which the MLM method has been applied to numerically generated surface elevation time series corresponding to the target incident directional spectrum parameters in tests 1a,1b and 2a,2b and a reflection coefficient of $r(\omega) = 0.95$).
The estimated incident directional spectrum parameters and reflection coefficients corresponding to each of the four irregular wave tests are given in figs. 5.13-5.16.

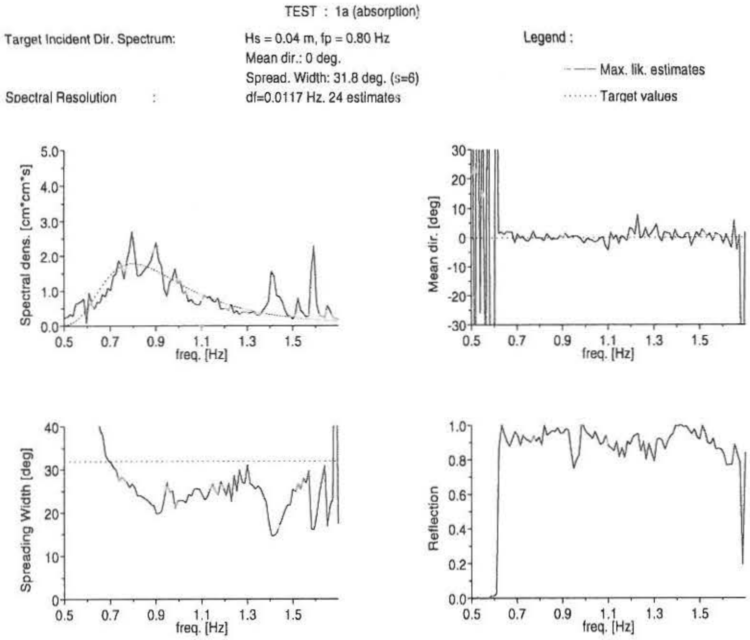

Figure 5.13: Est. and target incident dir. spectrum parameters, test 1a.

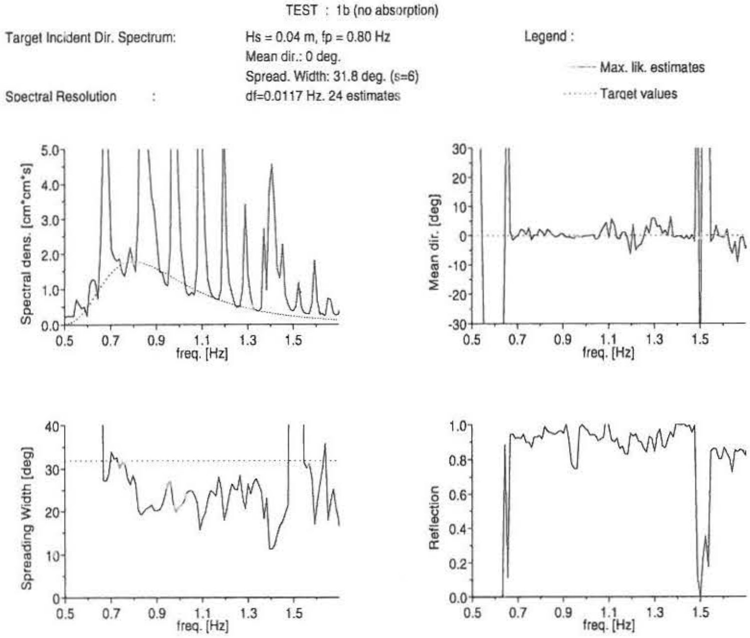

Figure 5.14: Est. and target incident dir. spectrum parameters, test 1b.

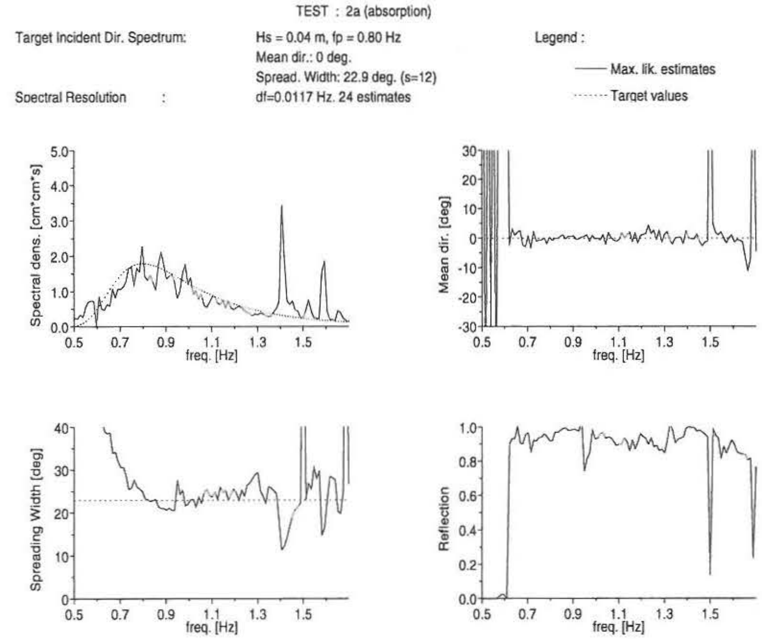

Figure 5.15: Est. and target incident dir. spectrum parameters, test 2a.

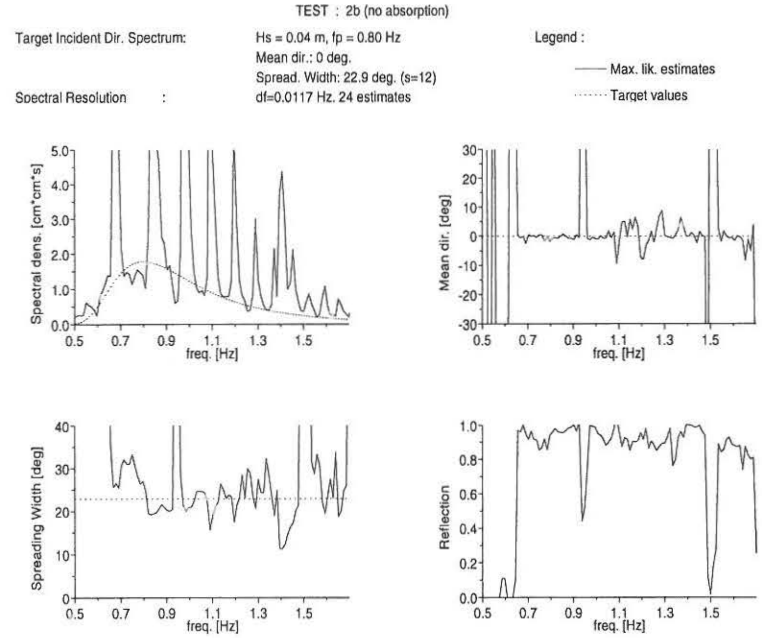

Figure 5.16: Est. and target incident dir. spectrum parameters, test 2b.

Figs. 5.13 and 5.15 show that when active absorption is applied, the estimated incident directional spectrum parameters are in reasonable agreement with the target values. In both tests the estimated parameters corresponding to frequencies of approximately 1.4 Hz differ significantly from the target parameters. Furthermore, inspection of fig. 5.13 shows that for test 1a, the estimated spreading width is generally lower than the target value whereas the estimated spectral density is higher than the target value for frequencies in the vicinity of the target peak frequency. However, comparison with the numerical test results given in Encl. 1 (figs. 14 and 15, Encl.1) shows that similar discrepancies appear in the corresponding numerical tests. Therefore, the discrepancies observed are not necessarily due to sources of error present in the physical model.
The discrepancies occurring for $f > 1.5$ Hz are due to the fact that zero gain was prescribed for the linear filters at frequencies above $f = 1.5$ Hz (sec. 5.4.2), i.e. no attempt was made to absorb reflected waves with frequencies above 1.5 Hz.

Figs. 5.14 and 5.16 demonstrate the effect of performing tests involving reflective structures without applying active absorption: in both tests, the incident wave spectrum is significantly disturbed by rereflection. As expected, peaks in the incident wave frequency spectrum appear at frequencies corresponding to constructive interference between incident and rereflected waves for a direction of $\theta = \theta_0 = 0$ deg.
For frequencies characterised by a peak in the incident wave energy, the spreading width is relatively low. This indicates that the increase in incident wave energy due to rereflection is largest for directions close to $\theta = 0$ deg.

5.5 Conclusion

A method for active absorption of multidirectional reflected wave fields in laboratory wave basins by means of an absorbing directional wave generator has been presented.

Reflected wave components are absorbed by generating additional wave components which cancel out the corresponding rereflected components. The wave paddle displacement correction signal for each individual wave paddle in the wave generator corresponding to absorption of the reflected wave field is estimated in real time by means of linear filtering and subsequent superposition of surface elevation time series measured at positions in the wave field in front of the wave generator. The frequency responses of the linear filters applied are determined so that the difference between the additional generated wave field and the wave field corresponding to elimination of the rereflected wave field is minimised. At a given frequency, this criterion yields a simple linear system of equations from which the complex filter frequency responses can be determined.

A conventional directional wave generator installed in the 3-D wave basin at the Hydraulics & Coastal Engineering Laboratory, Aalborg University, has been converted into an absorbing directional wave generator based on the method described above.

The absorbing directional wave generator has been applied to a series of tests involving generation of irregular, multidirectional wave fields in a test set-up, where a highly reflective structure spans the entire width of the basin. The test results show that the absorbing directional wave generator is capable of reducing the problem of rereflection significantly.

Chapter 6

Conclusion

Methods for mechanical generation of linear 2-dimensional (2-D) and 3-dimensional (3-D) waves in physical models have been presented.
The linear 2-D hydrodynamic transfer function relating the wave generator displacement signal to the generated surface elevation signal has been reviewed. The principle in mechanical 3-D wave generation has been presented, and the linear 3-D hydrodynamic transfer function has been derived. Methods for numerical synthesis of surface elevation signals or wave generator control signals corresponding to specified target incident (directional) wave spectra have been presented.
A series of laboratory 3-D wave generation tests have been performed. The test series involved generation of 5 different irregular, multidirectional sea states each characterised by a specified target directional wave spectrum. Wave generator displacement signals corresponding to the target directional wave spectra were synthesised by means of linear digital filtering of Gaussian white noise in the time domain. For each of the 5 tests the directional wave spectrum of the generated wave field was estimated based on surface elevation time series measured in the basin (the MLM and BDM methods for directional spectrum estimation were applied). In general, the estimated directional spectra were in excellent agreement with the corresponding target directional spectra. Consequently, it was concluded that wave fields corresponding to the 5 target directional wave spectra were successfully reproduced.

Absorbing wave generators capable of simultaneously generating the desired incident wave field and absorbing the reflected wave field have been developed and tested.
The absorbing wave generators presented are based on a new principle for active absorption of reflected waves: the wave generator displacement correction signal corresponding to absorption of the reflected wave field is determined in real time by means of linear filtering and subsequent superposition of surface elevation signals measured in P positions in the wave field in front of the wave generator.
For 2-D waves, the wave generator displacement correction signal corresponding to absorption of the reflected unidirectional wave train can be determined *exactly* by means of linear filtering of $P = 2$ measured surface elevation signals. Physical model tests were performed with an absorbing 2-D wave generator based on this principle. Irregu-

lar wave tests involving test structures with different degrees of reflection were carried out. The test results show that excellent absorption characteristics were achieved.

For 3-D waves, the displacement correction signal for each individual wave paddle corresponding to absorption of the multidirectional reflected wave field is *estimated* in real time by means of linear filtering and subsequent superposition of surface elevations measured in P positions in the wave field in front of the wave paddle. The frequency responses of the linear filters applied are determined so that the difference between the additional generated wave field and the wave field corresponding to elimination of the rereflected wave field is minimised. A conventional directional wave generator has been converted into an absorbing directional wave generator based on this principle and applied to a series of physical model tests. The tests performed involved generation of irregular, multidirectional wave fields in a test set-up where a highly reflective structure spanned the entire width of the wave basin. The test results show that the absorbing directional wave generator was capable of reducing the problem of rereflection in multidirectional wave fields significantly.

References

Biésel, F. and Suquet, F., 1951.
"Les Apparails Generateurs de Houle en Laboratorie". La Houille Blanche, Vol. 6, nos. 2,4 et 5.

Borgman, L. E., 1969.
"Ocean Wave Simulation for Engineering Design". Journal of the Waterways and Harbors Division, ASCE, Vol. 95, No. WW4, pp. 557-583.

Bullock, G.N. and Murton, G.J., 1989.
"Performance of a Wedge Type Absorbing Wave Maker". Journal of Waterway, Port, Coastal and Ocean Engineering, ASCE, Vol. 115, No.1, pp. 1-17.

Burcharth, H. F., Nielsen, S. R. K. and Schaarup-Jensen, K., 1986.
"A Three Dimensional Sea Facility for Deep and Shallow Water Waves". Proceedings of the 5th Offshore Mechanics and Arctic Engineering Symposium, Tokyo, pp 72-79.

Chilo, B. and Corsini, S., 1994.
"Wave Calibration in 2D Models". Proceedings, Int. Symposium: Waves - Physical and Numerical Modelling. UBC, Vancouver, Canada. Vol. 1, pp. 185-194.

Christensen, M. and Frigaard, P., 1994.
"Design of Absorbing Wave Maker Based on Digital Filters". Proceedings, Int. Symposium: Waves - Physical and Numerical Modelling. UBC, Vancouver, Canada. Vol. 1, pp. 100-109.

Dean, R. G. and Dalrymple, R. A., 1984.
"Water Wave Mechanics for Engineers and Scientists". Prentice-Hall Inc., Englewood Cliffs, New Jersey.

Funke, E. R. and Mansard, E. P., 1987.
"A Rationale for the Use of the Deterministic Approach to Laboratory Wave Generation". Proceedings of Wave Analysis and Generation in Laboratory Basins, 22nd Congress International Association for Hydraulic Research, pp. 153-195.

Gilbert, G., 1978.
"Absorbing Wave Generators". Hydr. Res. Station notes, Hydr. Res. Station, Wallingford, Oxon, United Kingdom, 20, 3-4.

Goda, Y. and Suzuki, Y, 1976.
"Estimation of Incident and Reflected Waves in Random Wave Experiments". Proceedings 15th Int. Conf. on Coastal Eng., pp. 828-845.

Hashimoto, N. and Kobune, K., 1987.
"Estimation of Directional Spectrum using the Bayesian Approach, and its Application to Field Data Analysis". Report of The Port and Harbour Research Institute, Vol. 26, No. 5, Ministry of Transport, Japan.

Hirakuchi, H., Kajima, R., Kawaguchi, T., 1990.
"Application of a Piston-Type Absorbing Wavemaker to Irregular Wave Experiments". Coastal Eng. Japan, Vol. 33, No. 1, pp. 11-24.

Hirakuchi, H., Kajima, R., Shimuzu, T., Ikeno, M., 1992.
"Charachteristics of Absorbing Directional Wave Maker". Proceedings 23rd Int. Conf. on Coastal Eng., pp. 281-292.

Hughes, S. A., 1993.
"Laboratory Wave Reflection Analysis Using Colocated Gages". Coastal Engineering, Vol. 20, pp. 223-247.

Isobe, M., 1990.
"Estimation of Directional Spectrum Expressed in Standard Form". Proceedings 22nd Int. Conf. on Coastal Eng., pp. 647-660.

Jefferys, E. R., 1987.
"Directional Seas should be Ergodic". Appl. Ocean Research, Vol. 9, No. 4, pp. 186-191.

Kaplan, W., 1981.
"Advanced Mathematics for Engineers". Addison-Wesley Publishing Company Inc., Reading, Massachusetts.

Karl, J. H., 1989.
"An Introduction to Digital Signal Processing". Academic Press, San Diego.

Mansard, E. and Funke, E., 1980.
"The Measurement of Incident and Reflected Spectra Using a Least Squares Method". Proceedings 17th Int. Conf. on Coastal Eng., Vol. 1, pp. 154-172.

Miles, M. D., 1989.
"A Note on Directional Random Wave Synthesis by the Single Summation Method". Proceedings, XXIII Congress of of the Int. Ass. for Hyd. Res., Ottawa, 1989.

Miles, M. D. and E. R. Funke, 1989.
"A Comparison of Methods for Synthesis of Directional Seas". J. Offshore Mech. Arct. Eng., v. 111, n. 1, pp. 43-48.

Milgram, J.S., 1970.
"Active Water-Wave Absorbers". J. Fluid Mech., 43(4), pp. 845-859.

Mitsuyasu, H., 1975.
"Observation of Directional Spectra of Ocean Waves using a Cloverleaf Buoy". Journal of Physical Oceanography, Vol. 5, pp. 750-760.

Newland, D. E., 1975.
"Random Vibrations and Spectral Analysis". Longman Group Ltd., London.

Ross, S. M., 1987.
"Introduction to Probability and Statistics for Engineers and Scientists". John Wiley & Sons, New York.

Sand, S. E., 1979.
"Three-Dimensional Deterministic Structure of Ocean Waves". Institute of Hydrodynamic and Hydraulic Engineering, , Tech. University of Denmark, Series paper no. 24.

Sand, S. E., 1985.
"Stochastic Processes: Practical Computation of Spectra". Institute of Hydrodynamic and Hydraulic Engineering, , Tech. University of Denmark.

Sand, S. E. and Mynett, A. E., 1987.
"Directional Wave Generation and Analysis". IAHR Seminar on Wave Analysis and Generation in Laboratory Basins, Lausanne, pp. 363-376.

Schäffer, H. A., Stolborg, T. and Hyllested, P., 1994.
"Simultaneous Generation and Active Absorption of Waves in Flumes". Proceedings, Int. Symposium: Waves - Physical and Numerical Modelling. UBC, Vancouver, Canada. Vol. 1, pp. 90-99.

Solomonidis, C. and Yarimer, E., 1992.
"Design of Recursive Filters for Random Wave Simulation". Appl. Math. Modelling, Vol. 16, pp. 357-373.

Tuah, H. and Hudspeth, R. T., 1982.
"Comparisons of Numerical Random Sea Simulations". Journal of the Waterway, Port, Coastal and Ocean Division, ASCE, Vol. 108, No. WW4, pp. 569-584.

Appendix A

Non-Recursive Digital Filters

The following is a short introduction to non-recursive digital filters. The introduction includes a presentation of the general recursive form of digital filters. Recursive filters are classified as linear, time-invariant systems (LTI-systems).
Subsequently, the frequency response of non-recursive filters is presented, and a simple technique for non-recursive filter design is introduced. Finally, the concept of causality will be defined.

A.1 LTI-systems

A digital filter is a discrete-time system, transforming a discrete sequence of input data, x_n, into a discrete sequence of output data, y_n.
The general form of a so-called *recursive* digital filter is given by

$$y_n = \sum_{j=-J}^{J} c_j x_{n-j} + \sum_{k=1}^{K} d_k y_{n-k} \tag{A.1}$$

where c_j and d_k are the filter coefficients.
The term "recursive" refers to the latter of the two sums in eq. (A.1) which relates the present output to previous outputs. If the coefficients d_k are chosen as 0, the filter is non-recursive.
The *impulse response* of a digital filter is defined as the output produced when the input is a digital impulse p_n defined as

$$p_n = \begin{cases} 1 & \text{if n=0} \\ 0 & \text{otherwise} \end{cases} \tag{A.2}$$

Digital filters are often classified in accordance with their impulse response. Thus recursive filters are generally Infinite Impulse Response filters (*IIR-filters*) whereas non-recursive filters are Finite Impulse Response filters (*FIR-filters*).

It is easily verified that a recursive filter S exhibits the following properties (Karl, 1989)

1. *Linearity:*
   If x_n and z_n are discrete-time data sequences, then
   $S(ax_n + bz_n) = aS(x_n) + bS(z_n)$
   where a and b are arbitrary constants.
2. *Time-invariance:*
   The rule used to compute the output does not depend on the time at which the input is applied. That is, an impulse applied as input to the filter will produce the same output independent of when the input occurs, except for the corresponding time shift.

Consequently, recursive filters are so-called *LTI-systems* (Linear Time-Invariant systems).
In the following, only non-recursive filters will be treated. In general, a given frequency response can be modelled with considerably fewer filter coefficients when applying a recursive filter, thus providing faster data processing. However, non-recursive filters are easier to understand, design and use.

A.2 Frequency Response

The input-output relation of a *non-recursive* digital filter of odd length N is given by the discrete convolution integral

$$y_n = \sum_{j=-J}^{J} c_j x_{n-j} \qquad , J = \frac{N-1}{2} \tag{A.3}$$

If the input to a non-recursive filter is a discrete-time complex exponential

$$x_n = e^{i\omega n} \tag{A.4}$$

the output becomes

$$\begin{aligned} y_n &= \sum_{j=-J}^{J} c_j e^{i\omega(n-j)} && \text{(A.5)} \\ &= e^{i\omega n} \sum_{j=-J}^{J} c_j e^{-i\omega j} && \text{(A.6)} \end{aligned}$$

Thus, the output is likewise a discrete-time complex exponential modified only by the factor

$$\mathcal{H}(\omega) = \sum_{j=-J}^{J} c_j e^{-i\omega j} \tag{A.7}$$

which is called the *frequency response* of the filter operator.
The frequency response is normally expressed in terms of magnitude (gain) $|\mathcal{H}(\omega)|$ and phase $\phi(\omega)$

$$\mathcal{H}(\omega) = |\mathcal{H}(\omega)| e^{i\phi(\omega)} \tag{A.8}$$

where

$$\begin{aligned} |\mathcal{H}(\omega)| &= \sqrt{\mathcal{H}(\omega).re^2 + \mathcal{H}(\omega).im^2} && \text{(A.9)} \\ \phi(\omega) &= \arctan\left(\frac{\mathcal{H}(\omega).im}{\mathcal{H}(\omega).re}\right) && \text{(A.10)} \end{aligned}$$

If the filter has *real* coefficients, the frequency response for positive frequencies is related to the response for negative frequencies. Applying the Euler identity to eq. (A.7) yields

$$\begin{aligned} \mathcal{H}(\omega).re &= \sum_{j=-J}^{J} c_j \cos(\omega j) && \text{(A.11)} \\ \mathcal{H}(\omega).im &= -\sum_{j=-J}^{J} c_j \sin(\omega j) && \text{(A.12)} \end{aligned}$$

Thus, the real part of the frequency response is a sum of even (cosine) functions of ω, whereas the imaginary part is a sum of odd (sine) functions of ω. Therefore

$$\begin{aligned} \mathcal{H}(\omega).re &= \mathcal{H}(-\omega).re && \text{(A.13)} \\ \mathcal{H}(\omega).im &= -\mathcal{H}(-\omega).im && \text{(A.14)} \end{aligned}$$

i.e. for real filter coefficients c_j, the frequency response is Hermitian (Karl (1989)). In terms of magnitude and gain, this yields

$$\begin{aligned} |\mathcal{H}(\omega)| &= |\mathcal{H}(-\omega)| && \text{(A.15)} \\ \phi(\omega) &= -\phi(-\omega) && \text{(A.16)} \end{aligned}$$

If the input to a real-coefficient non-recursive filter is a cosine

$$\begin{aligned} x_n &= \cos(\omega n) && \text{(A.17)} \\ &= \frac{1}{2}(e^{i\omega n} + e^{-i\omega n}) && \text{(A.18)} \end{aligned}$$

the following output is obtained

$$\begin{aligned} y_n &= \frac{1}{2}(\mathcal{H}(\omega)e^{i\omega n} + \mathcal{H}(-\omega)e^{-i\omega n}) && \text{(A.19)} \\ &= \frac{1}{2}\left(|\mathcal{H}(\omega)|e^{i(\omega n+\phi(\omega))} + |\mathcal{H}(-\omega)|e^{-i(\omega n-\phi(-\omega))}\right) && \text{(A.20)} \\ &= \frac{1}{2}\left(|\mathcal{H}(\omega)|e^{i(\omega n+\phi(\omega))} + |\mathcal{H}(\omega)|e^{-i(\omega n+\phi(\omega))}\right) && \text{(A.21)} \\ &= |\mathcal{H}(\omega)|\cos(\omega n + \phi(\omega)) && \text{(A.22)} \end{aligned}$$

Thus, the response of a real-coefficient non-recursive filter to a cosine input of frequency ω is the input scaled by $|\mathcal{H}(\omega)|$ and shifted in phase by $\phi(\omega)$.

A.3 Design of Non-Recursive Digital Filters

Non-recursive filter design addresses the problem of computing the filter coefficients c_j (the filter operator) for use in convolving with the input data to achieve a desired frequency response $\mathcal{D}(\omega)$.
The common approach in non-recursive filter design is to define a design error $\epsilon(\omega)$ as the difference between the desired response and the filters actual response

$$\epsilon(\omega) = \mathcal{D}(\omega) - \mathcal{H}(\omega) \tag{A.23}$$

The design criterion is chosen as the integral squared design error

$$\delta = \int_{-\pi}^{\pi} |\epsilon(\omega)|^2 d\omega \tag{A.24}$$

The filter coefficients c_j are chosen in such a way that the design criterion is minimised

$$\begin{aligned} \frac{\partial \delta}{\partial c_j} &= 0 \\ \Rightarrow \quad c_j &= \frac{1}{2\pi} \int_{-\pi}^{\pi} \mathcal{D}(\omega) e^{i\omega j} d\omega \end{aligned} \tag{A.25}$$

This result is identical to computing the Fourier coefficients of the Fourier expansion of $\mathcal{D}(\omega)$. Thus, if $\mathcal{D}(\omega)$ is a piecewise continuous function, $\mathcal{H}(\omega)$ converges to $\mathcal{D}(\omega)$ as J approaches infinity (Kaplan, 1981).
However, for practical applications, the filter operator must be truncated, i.e. reduced to a finite number of coefficients. Consequently, the filter frequency response will, in general, differ from the desired frequency response, particularly when the desired frequency response is characterised by quick transitions and discontinuities. In such cases, the least-squares fit given by eq. (A.25) is often not the most desirable solution. Applying a window function to the filter operator may improve the result (Karl, 1989). The use of window functions is a straight-forward approach, but it has the disadvantage of little design flexibility.
Alternatively, the following iterative procedure can be applied

1. Sample the desired frequency response

$$\mathcal{D}(\omega_k) = \mathcal{D}(k\frac{2\pi}{N}) \quad ,k = -J..J \tag{A.26}$$

2. Compute the filter coefficients c_j by means of IDFT

$$c_j = \frac{1}{N} \sum_{k=-J}^{J} \mathcal{D}(\omega_k) e^{ik2\pi j/N} \tag{A.27}$$

3. Determine the actual frequency response $\mathcal{H}(\omega)$ given by eq. (A.7). If the result is unacceptable, readjust the sampled frequency response $\mathcal{D}(\omega_k)$ and return to 2.

Figs. 1 and 2 illustrate how this simple trial-and-error approach to non-recursive filter design is applied to the design of a lowpass filter operator with $N = 33$ coefficients. Sampling the desired ideal lowpass filter frequency response $\mathcal{D}(\omega)$ results in large ripples in stop band and pass band. The ripples are caused by the discontinuity in the desired magnitude response at $\omega = \frac{\pi}{2}$ which cannot be modelled with a finite length filter operator. A considerable reduction in ripple amplitude is achieved by readjusting the sampled frequency response by prescribing a magnitude response of $|\mathcal{D}(\omega_k)| = 0.5$ at $\omega_k = \frac{\pi}{2}$ (see fig A.2). However, this manipulation of the sampled frequency response has had the undesirable effect of broadening the transition zone.

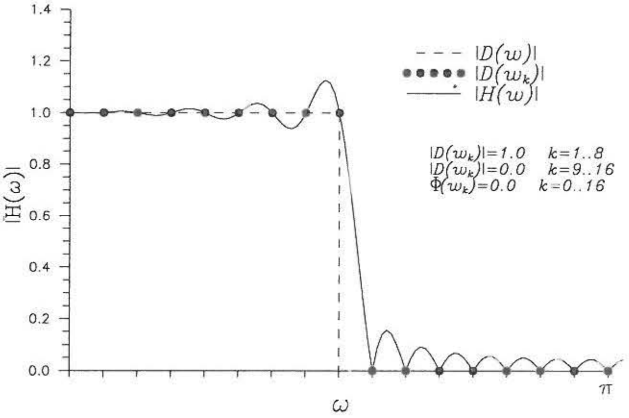

Figure A.1: Magnitude response $\mathcal{H}(\omega)$ of 33-coefficient lowpass filter.

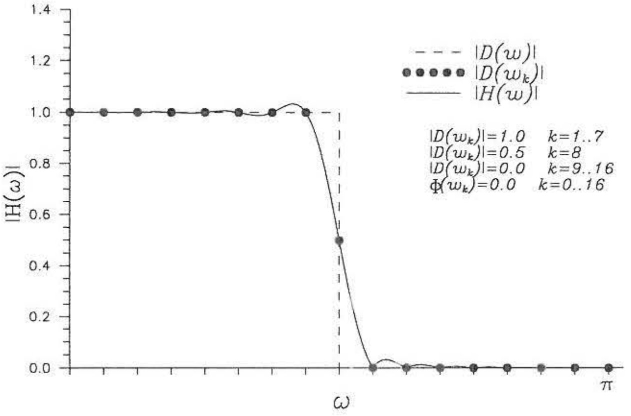

Figure A.2: Magnitude response $\mathcal{H}(\omega)$ of 33-coefficient lowpass filter. Ripple-sizes reduced and transition zone broadened by setting $|\mathcal{D}(\omega_8)| = 0.5$.

A.4 Causal Non-Recursive Digital Filters

A system is *causal* if the system output depends only on past and present values of the input. The N-coefficient non-recursive filter defined by eq. (A.3)

$$y_n = \sum_{j=-\frac{N-1}{2}}^{\frac{N-1}{2}} c_j x_{n-j} \tag{A.28}$$

is clearly non-causal because the output depends on future values of the input.
In real-time computing, future input values are not available. Consequently, only causal systems are applicable. The causal version of eq. (A.28) is given by

$$y_n = \sum_{j=0}^{N-1} c_j x_{n-j} \tag{A.29}$$

In (A.29), the output is delayed $\frac{N-1}{2}$ relative to the input. In order to compensate for the phase-shift introduced by the delay, a phase-shift of

$$\phi(\omega) = \left(\frac{N-1}{2}\right)\omega \tag{A.30}$$

must be prescribed.

Appendix B

Servocontrol System Frequency Response

In the following, the control system of the serpent-type directional wave generator applied in the laboratory tests presented in chap. 4 and 5 is described, and the results of measurements of the servocontrol system frequency response are given.

B.1 Wave Generator Control System

As described in chap. 4, the directional wave maker consists of 9 paddles hinged with vertical axes to 10 individually controlled hydraulic powered piston-type machines regulated by electric MOOG valves (see fig. B.1).

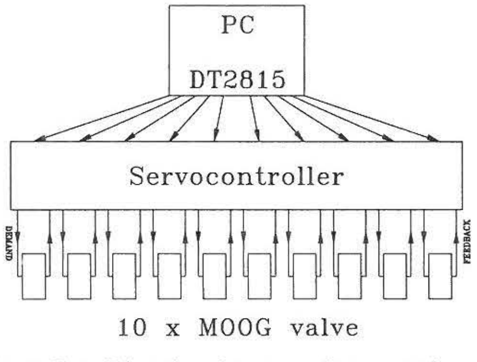

Figure B.1: Directional wave maker control system.

Prior to each test, a digital wave generator displacement signal corresponding to each individual piston was generated by means of the time domain white noise filtering method described in chap. 4 (a sample frequency of $f_s = 30\,\mathrm{Hz}$ was applied). The displacement signals were stored on the harddisk of a PC (the computational speed of the PC was not sufficiently high to enable on-line generation of the displacement signals). When wave generation is performed, the digital displacement signals are read from the harddisk and transferred to DT2815 D/A-boards installed in the PC. Here, the displacement signals are converted to analog signals and sent to the servocontroller (one channel is reserved for each hydraulic machine, i.e. two 8-channel DT2815 D/A-boards are required).

B.2 Measurement of Servocontrol System Frequency Response

In order to determine the frequency response of the wave generator servocontrol system, i.e. the transfer function between the prescribed piston displacement signal $X(t)$ sent to the servocontroller and the actual piston displacement signal $X_a(t)$, a series of regular wave tests was performed.

Assuming that the transfer function is linear, a prescribed displacement signal given by

$$X(t) = A\cos(\omega t) \tag{B.1}$$

will yield the actual displacement signal

$$X_a(t) = |\mathcal{W}(\omega)| A \cos\left(\omega t + \phi(\omega)\right) \tag{B.2}$$

where $|\mathcal{W}(\omega)|$ and $\phi(\omega)$ denote the gain and phase of the servocontrol system frequency response $\mathcal{W}(\omega)$.

The test set-up for the regular wave tests is given in fig B.2. A displacement transducer was installed on hydraulic machine no. 1. The hydraulic machine and the displacement transducer were calibrated by applying a constant voltage signal to the servocontroller and measuring the corresponding piston displacement [m] and displacement transducer signal [V].

In each test, a sinusoidal voltage signal with a given frequency f and an amplitude corresponding to a piston displacement amplitude of $A = 0.02\,\mathrm{m}$ was sent to all 10 pistons. During the test, a PC equipped with a DT570 A/D card sampled the voltage signal from the DT2815 card and the displacement transducer simultaneously at a rate of $f_s = 100\,\mathrm{Hz}$. By applying the calibration factors, these signals were converted into the prescribed piston displacement signal and the actual piston displacement signal, respectively.

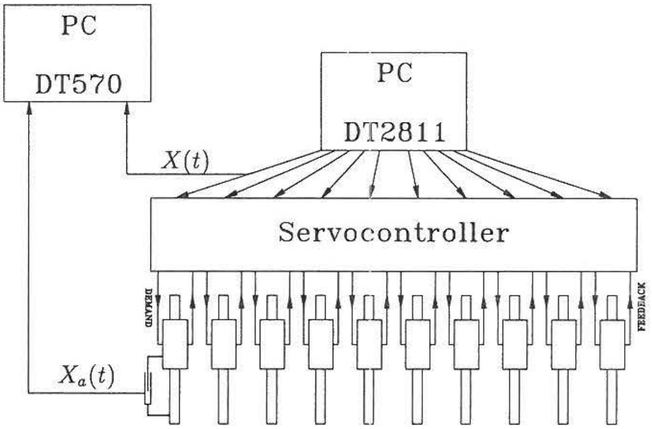

Figure B.2: Test set-up for measurement of frequency response.

Seven tests involving frequencies of $f = 0.7\,\text{Hz}$ to $1.3\,\text{Hz}$ were performed. Fig. B.3 shows a segment of the displacement time series recorded in test no. 1 ($f = 0.7\,\text{Hz}$).

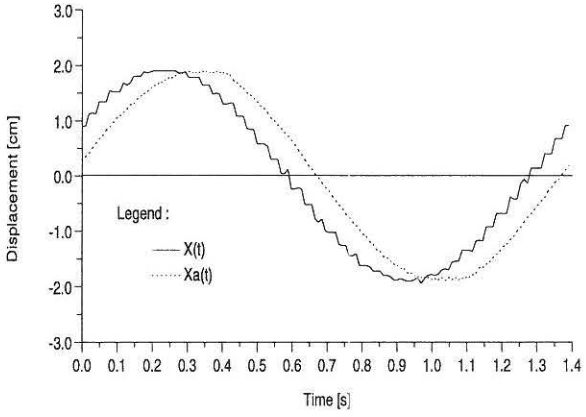

Figure B.3: Displacement time series.

For each test, the servocontrol system frequency response $\mathcal{W}(f)$ at frequency f is derived by means of Discrete Fourier transform (DFT) analysis (Newland (1975)). The DFT of simultaneously recorded time series $X(r\Delta t) = x_r$ and $X_a(r\Delta t) = y_r$ is

Test no.	f	$\lvert\mathcal{W}(f)\rvert$	$\phi(f)$	$\delta(f)$
	Hz		rad	s
1	0.7	1.002	0.395	0.0898
2	0.8	1.003	0.455	0.0905
3	0.9	1.002	0.490	0.0867
4	1.0	1.006	0.526	0.0837
5	1.1	1.013	0.574	0.0830
6	1.2	0.978	0.592	0.0785
7	1.3	0.967	0.639	0.0782

Figure B.4: Measured servocontrol frequency response.

determined as

$$X_k = \frac{1}{N}\sum_{r=-N}^{N} x_r e^{-i(2\pi k r/N)} \tag{B.3}$$

$$Y_k = \frac{1}{N}\sum_{r=-N}^{N} y_r e^{-i(2\pi k r/N)} \tag{B.4}$$

where N is chosen in such a way that $(2N+1)\Delta t$ represents one period of the displacement signals $T = 1/f$ in order to avoid spectral leakage.
Subsequently, the servocontrol system frequency response at frequency $\omega_k = 2\pi k/T$ is calculated from

$$\begin{aligned} \mathcal{W}_k &= \frac{S_{XY_k}}{S_{XX_k}} && \text{(B.5)} \\ &= \frac{X_k^* Y_k}{X_k^* X_k} && \text{(B.6)} \end{aligned}$$

where superscript $*$ denotes complex conjugate.
The value of $\mathcal{W}_k$ corresponding to $k = 1$ represents the servo control system complex frequency response at frequency f.

In fig. B.4 the measured gain and phase of the servocontrol system frequency response is tabulated. The delay between the prescribed and actual paddle displacement signal defined as

$$\delta(f) = \phi(f)/(2\pi f) \tag{B.7}$$

is also given. Fig. B.4 shows that the servocontrol frequency response is characterised by approximately unity gain and a delay of 0.08 s-0.09 s in the frequency range of 0.7 Hz-1.3 Hz.

Enclosure 1

Maximum Likelihood Estimation of Directional Spectrum Expressed in Standard Form

Maximum Likelihood Estimation of Directional Spectrum Expressed in Standard Form

Morten Christensen and Niels Bo Sørensen
Hydraulics & Coastal Engineering Laboratory
Aalborg University
Sohngaardsholmsvej 57, DK-9000 Aalborg, Denmark

January 1994
Revised June 1995